From the Department of Radiation Therapy and Radiation Oncology,
Faculty of Medicine, Saarland University,
Homburg/Saar, Germany

Elucidating the role of histone variant H2A.J following ionizing radiation

A thesis submitted to the Faculty of Medicine in fulfilment of
the requirements for the degree of
Doctor of Philosophy (Ph.D.)
Faculty of Medicine,
SAARLAND UNIVERSITY
2021

Submitted by: Anna-Luka Isermann
Born on the 27.08.1987 in Letterkenny

Tag der Promotion:	21. April. 2021
Dekan:	Univ.-Prof. Dr. med. Michael D. Menger
Berichterstatter:	Prof. Dr. rer. nat. Jens Mayer Prof. Dr. med. Claudia E. Rübe

Table of contents

1 Abbreviations

53BP1	Tumor Protein P53-Binding Protein
alt-NHEJ	alternative-NHEJ
ASF-1a	Anti-silencing factor 1 a
ATM	ataxia-telangiectasia mutated
ATR	ataxia telangiectasia and Rad3-related protein
BCA	bicinchoninic acid
BER	base excision repair
BLM	Bloom syndrome protein
bp	base pairs
BRCA2	BRCA2 DNA repair associated
BrdU	Bromodeoxyuridine / 5-bromo-2'-deoxyuridine
BSA	bovine serum albumin
CCL2	C-C Motif Chemokine Ligand 2
cDNA	complementary DNA
Cer-XLF	Cernunnos-X4-like factor
ChIP-seq	Chromatin Immunoprecipitation DNA-Sequencing
CHK1	checkpoint kinase 1
CHK2	checkpoint kinase 2
CRB2	Crumbs Cell Polarity Complex Component 2
CSF2	Colony Stimulating Factor 2
CtIP	C-terminal-binding protein interacting protein
Ct	cycle threshold
CT	computer tomography
CXCL8	chemokine (C-X-C motif) ligand 8
DH2O	distilled water
DAB	3,3'-diaminobenzidine
DAPI	4′,6-diamidino-2-phenylindole
DC	dendritic cells
DETC	dendritic epidermal T cells
DDR	DNA damage response
DMSA	7,12-dimethylbenz(a)-anthracene
DMSO	Dimethylsulfoxide
DNA	Deoxyribonucleic acid
DNA-PK	DNA-dependent protein kinase
DNA-SCARS	DNA segments with chromatin alterations reinforcing senescence
dox	doxycycline

ETO	etoposide
EtOH	ethanol
EDTA	Ethylenediaminetetraacetic acid
ELISA	enzyme-linked immunosorbent assay
EXO1	exonuclease 1
FCS	fetal calf serum
g	gravitational force
GAPDH	Glyceraldehyde 3-phosphate dehydrogenase
GROalpha	growth regulated oncogene-alpha
Gt	goat
Gm-csf	Granulocyte-macrophage colony-stimulating factor
Gy	Gray
H2A.J	Histone H2A variant J
H3K9ac	H3 acetylated at lysine 9
H3K9me3	H3 trimethylated at lysine 9
H3K36me3	H3 trimethylated at lysine 36
HIRA	histone repressor A
HCL	hydrochloric acid
HGF	hepatocyte growth factor
HGPS	Hutchinson-Gilford Progeria Syndrome
HP1	heterochromatin protein 1
HR	homologous recombination
γH2AX	Histone H2A.X phosphorylated at Serine 139
IFM	immunofluorescence microscopy
IFNγ	interferon gamma
IGFBP-7	Insulin-like growth factor-binding protein *7*
IL1β	interleukin 1 beta
IL6	interleukin 6
IL8	interleukin 8
IL12	interleukin 12
ILC	innate lymphoid cells
IVC	individually ventilated cage
IP10	Interferon gamma-induced protein 10
IR	ionizing radiation
IRIF	irradiation–induced foci
KAP 1	KAP-associated protein 1
KD	TERT/ptet-on-sh3-H2AFJ insert
Ku70	X-ray repair cross-complementing protein 6

Ku80	X-ray repair cross-complementing protein 5
LAD	lamine-associated domains
LET	linear energy transfer
LMB1	lamine B1
mAB	monoclonal antibody
MAP	mitogen-activated protein
MCP1	Monocyte chemoattractant protein 1
MDC1	Mediator of DNA damage checkpoint protein 1
Mdn	median
MEM	minimum essential medium
MIP1α	acrophage inflammatory protein 1-alpha
mGy	milligray
MgCl	magnesium chloride
MMR	mismatch repair
MRE11	meiotic recombination 11 homolog
Ms	mouse
MV	megavolt
nm	nanometers
N_2	nitrogen
NaCl	sodium chloride
NET	nuclear envelope transmembrane proteins
NF-κB	nuclear factor kappa-light-chain-enhancer of activated B cells
NBS1	Nijmegen breakage syndrome protein 1
NHEJ	non-homologous end joininig
NER	nucleotide excision repair
NT	WI-38hTERT/ptet-on-sh-NoTarget insert
OIS	oncogene-induced senescence
p16INK4a	cyclin dependent kinase inhibitor 2A
P21	cyclin-dependent kinase inhibitor 1
p38MAPK	p38 mitogen-activated protein kinases
PARP	Poly (ADP-ribose) polymerase
PBS	phosphate buffered saline
PES	polyethersulfone
PFA	paraformaldehyde
PIKK	phosphoinositide 3-kinase (PI3K)-related
PLA	proximity ligation assay
PML-NB	promyelocytic leukemia protein nuclear bodies
PTM	post-translational modification

p53	tumor protein 53
Rab	rabbit
RAD50	ATP-binding cassette–ATPase
RBE	relative biological effectiveness
RC	replication coupled
RFP	red fluorescent protein
RNA	ribonucleic acid
RNF 8	Ring Finger Protein 8
RNF168	Ring Finger Protein 168
ROS	reactive oxygen species
RPA	replication protein A
RPMI	Roswell Park Memorial Institute medium
RS	replicative senescence
RT	room temperautre
RT-qPCR	quantitative reverse transcription polymerase chain reaction
SA-β-gal	senescence-associated beta galactosidase
SAHF	senescence-associated heterochromatin foci
SASP	senescence-associated secretory phenotype
SEM	standard error of mean
SIPS	stress-induced premature senescence
ssDNA	single strand DNA
SSA	single strand annealing
SSBR	single strand break repair
TEM	transmission electron microscope
TERT	Telomerase reverse transcriptase
TGFβ1	Transforming growth factor beta
TNFα	Tumor necrosis factor alpha
Topo II	DNA Topoisomerase II
XRCC4	X-ray repair cross-complementing protein

2 Summary/ Zusammenfassung

Elucidating the role of histone variant H2A.J following ionizing radiation

Senescence is a stress-induced state in which cells cease proliferation whilst remaining metabolically active. While it is a noteworthy tumour suppressor mechanism, accumulation of senescent cells in aged tissue or tissue damaged through toxins such as *ionizing radiation* (IR), it has been implicated as a one of the nine hallmark ageing mechanisms, as well as, inducing premature ageing and promoting neoplastic growth. The limited study of novel histone variant H2A.J, has uncovered accumulation of H2A.J in *etoposide (ETO)*-induced and *oncogene-induced senescence* (OIS). Additionally, it plays a functional role in induction of the inflammatory senescence-associated secretory phenotype, a major effector of ageing and cancer. Whilst the DNA-damaging properties of radiotherapy aid in tumour growth control, healthy tissue is inevitably exposed to low doses of irradiation with side-effects including inflammation and radiation–induced senescence. This study therefore seeks to elucidate a possible role of H2A.J association with irradiation-induced senescence, DNA-damage repair and senescence-associated secretory phenotype.

H2A.J knock-down WI-38 lung fibroblasts and No-Target WI-38 lung fibroblasts containing unaltered H2A.J expression were irradiated and compared. *Immunofluorescence microscopy* (IFM) examinations were applied to determine H2A.J accumulation in response to IR, DNA-damage repair efficiency, senescence induction, proliferative arrest, *senescence-associated heterochromatin foci* (SAHF) formation and *DNA-segments with chromatin alterations reinforcing senescence* (DNA-SCARS) formation. *Transmission electron microscopy* (TEM) was applied to gain further insight into senescence-associated chromatin changes and H2A.J localisation in respect to SAHF and DNA-SCARS. Furthermore, ultrastructure of DNA-SCARS was examined at the nanoscale using TEM. The *senescence-associated secretory phenotype* (SASP) following radiation was investigated using *enzyme-linked immunosorbent assay* (ELISA), performed on conditioned medium, and *quantitative reverse transcription polymerase chain reaction* (RT-qPCR), performed on isolated RNA. Additionally, aged- and *ex vivo* irradiated human epidermal biopsies were evaluated for DNA-damage foci and H2A.J accumulation using IFM. *In vivo* immunofluorescence microscopy examinations of 20x 0.1Gy irradiated murine epidermis was also completed to gain insight into the long term accumulation of H2A.J following low-dose fractionated radiation.

In vitro studies revealed H2A.J accumulates in a dose-dependent manner with lower doses resulting in transient accumulation and higher doses inducing senescence, leading to long-term H2A.J positivity. H2A.J did not influence repair capacity following IR. Knock-down of

H2A.J did not affect senescence induction, proliferative arrest, or SAHF formation. It did, however, effect ultrastructure of DNA-SCARS, thereby potentially explaining the altered SASP revealed by ELISA and RT-qPCR. Human epidermal biopsy examinations revealed increased H2A.J in aged epidermis together with increasing presence of DNA-damage foci. *In vivo* murine epidermis showed increased H2A.J accumulation up to 6 months post-IR at a level similar to 18 month old aged mice.

This work provides a baseline insight into H2A.J accumulation following IR revealing potential insight into its influence on IR-induced SASP regulation. Additionally, indications arose for the application of H2A.J as a potential biomarker of senescent cells in culture, as well as, in human epidermal biopsies.

Die Bedeutung der Histonvariants H2A.J nach ionisierender Strahlung

Seneszenz beschreibt einen durch Stress induzierten zellulären Zustand, indem keine Proliferation stattfindet, die Zelle aber trotz allem metabolisch aktiv bleibt. Während Seneszenz damit in erster Linie einen effizienten Tumorsuppressions-Mechanismus darstellt, unterstützt die Akkumulation seneszenter Zellen in gealtertem oder bestrahltem Gewebe frühzeitige Alterung und das Tumorwachstum. Eine aktuelle Studie der Histonvariante H2A.J zeigt die Akkumulation von H2A.J im Rahmen einer Etoposid- und Onkogen-induzierten Seneszenz. Weiterhin bestätigte sich ein Zusammenhang zwischen H2A.J und der Induktion des *Seneszenz-assoziiertem sekretorischem Phänotyps* (SASP), einem Haupteffektor von Alterung und Krebs. In der Radiotherapie macht man sich die DNA-schädigenden Eigenschaften von ionisierender Strahlung zur gezielten Kontrolle des Tumorwachstums zu Nutze, wobei auch gesundes Gewebe in Tumornähe mit niedrigen Strahlendosen belastet wird. Dies kann möglicherweise Nebenwirkungen, wie Inflammation und strahlen induzierte Seneszenz, zur Folge haben. Im Rahmen dieser Dissertation sollen mögliche Zusammenhänge zwischen H2A.J und strahlen induzierter Seneszenz, der DNA-Schadensantwort sowie dem SASP untersucht werden.

Mithilfe von WI-38 Lungenfibroblasten, die zum einen eine unveränderte Expression von H2A.J durch Einbringung einer „No-Target“-Leerkassette und zum anderen einen H2A.J Knock-down aufweisen, wurden Unterschiede nach Bestrahlung eruiert. Unter Anwendung immunfluoreszenzmikroskopischer Analysen wurde die Akkumulation von H2A.J, die Effizienz der DNA-Reparatur, die Proliferation, die *Seneszenz-assoziierten heterochromatischen Foci* (SAHF) und die Entstehung von *DNA- Segments with chromatin alterations reinforcing senescence* (DNA-SCARS) untersucht. Anhand des Transmissionselektronenmikroskops (TEM) wurden zudem weitere Einblicke in die Lokalisation von H2A.J im Kontext von SAHF und DNA-SCARS gewährt. Zusätzlich wurde mittels TEM die Ultrastruktur und Entstehung von DNA-SCARS bestimmt. Der strahleninduzierte SASP wurde mithilfe eines ELISA im Zellüberstand gemessen und die Expression, der involvierten Gene, an Hand von RT-qPCR analysiert. Weiterhin wurden durch IFM-Analysen DNA-Reparaturfoci und die H2A.J Akkumulation in gealterter und *ex vivo* bestrahlter humaner Epidermis bestimmt. Abschließend wurde die Langzeit-Akkumulation von H2A.J in niedrig-dosis-exponierter muriner Epidermis untersucht.

In vitro Untersuchungen ergaben eine dosisabhängige Akkumulation von H2A.J nach Bestrahlung mit einer vorübergehenden H2A.J-Zunahme nach niedrigen Dosen und einer induzierten Seneszenz mit bleibender H2A.J-Expression nach hohen Dosen. Es zeigte sich zudem, dass die Effizienz der DNA-Schadensreparatur nach Bestrahlung nicht durch H2A.J beeinflusst wurde und dass der Knock-down von H2A.J keine Auswirkung auf die

Seneszenzinduktion, den Proliferationsarrest und die SAHF Entwicklung hat. Im Gegensatz dazu beeinflusste der H2A.J knock-down die Ultrastruktur der DNA-SCARS; was eine potentielle Erklärung für den verminderten SASP darstellen könnte, der mithilfe von ELISA und RT-qPCR nachgewiesen wurde. Untersuchungen an humaner Epidermis zeigten zudem eine Zunahme von H2A.J analog zu einem erhöhten Aufkommen an DNA-Reparaturfoci mit zunehmendem Alter und nach Bestrahlung. Die Analyse niedrig-dosis-exponierter muriner Epidermis wies selbst 6 Monate nach Ende der Bestrahlung eine zunehmende Akkumulation von H2A.J auf, die dem Level einer 18 Monate alten Maus entsprachen.

Diese Untersuchungen dienen als Grundlage um Zusammenhänge zwischen der Akkumulation von H2A.J und Bestrahlung zu erforschen und zeigen eine H2A.J-abhängige Induktion des SASP nach Bestrahlung. Schließlich zeigte sich, dass H2A.J als Biomarker für seneszenten Zellen *in vitro* und in der humanen Epidermis potentiell genutzt werden kann.

3 Introduction

3.1 Ionizing radiation and its effects

The first case of radiotherapy, or radiation therapy, can be traced back to 1896 when Emil Grubbe used X-rays to treat a patient suffering from breast cancer. Worryingly, this was only one year after Wilhelm Röntgen first discovered X-rays and the physical properties, and more importantly, the biological effects of radiation, were not yet known (Underwood, 1945). The term radiation can be described as emission of energy in the form of electromagnetic waves or moving subatomic particles through empty space. Radiation, in which the energy transported is immense enough to cause creation of positively or negatively charged particles from neutral atoms, is termed *ionizing radiation* (IR). IR is characterized into electromagnetic and particulate radiation. X-rays and γ-radiation are both forms of electromagnetic radiation in which energy is transferred in waves (or photons). Particulate radiation, on the other hand, involves transfer of energy through atomic or subatomic particles which possess both energy and mass and so transfer kinetic energy onto electrons with which they collide. Particulate radiation includes α radiation (consisting of α particles), β radiation (consisting of electrons or positrons), heavy-ion radiation and neutron radiation. Each type of IR has a specific *linear energy transfer* (LET) which refers to the amount of energy deposited along the beam trajectory within a material per unit distance. X-rays and γ-radiation are sparsely ionizing forms of IR (low LET) whereas protons and heavy charged particles are examples of densely IR (high LET).

$$LET = \frac{dE}{dx} = \frac{locally\ imparted\ energy\ (keV)}{distance\ traversing\ medium\ (\mu m)}$$

The *relative biological effectiveness* (RBE) increases with increasing LET, however, it also depends on the amount of energy absorbed per unit mass, which in turn, is linked to the exposed cell- or tissue type (Podgorsak, 2005). This is known as the dose and is measured in *Gray* (Gy) (S.M. Seltzer, 2011).

$$D\ (Gy) = \frac{E}{m}$$

When a cell is irradiated, the effect of radiation is divided into three phases; the physical phase referring to interaction between IR and atoms within tissue, the chemical phase in which energized or ionized atoms react, and the biological phase wherein enzymatic reactions begin repair of damage generated throughout the chemical phase. The main aim of radiation therapy is induction of cell death through DNA damage of tumor cells, achieved through direct and indirect means (Figure 1) (Goodhead 1994). Direct action occurs through interaction between radiation and atoms of the DNA molecule itself, inducing atomic

excitation or ionization, triggering a chain of physical and chemical reactions which eventually lead to biological damage of the DNA molecule.

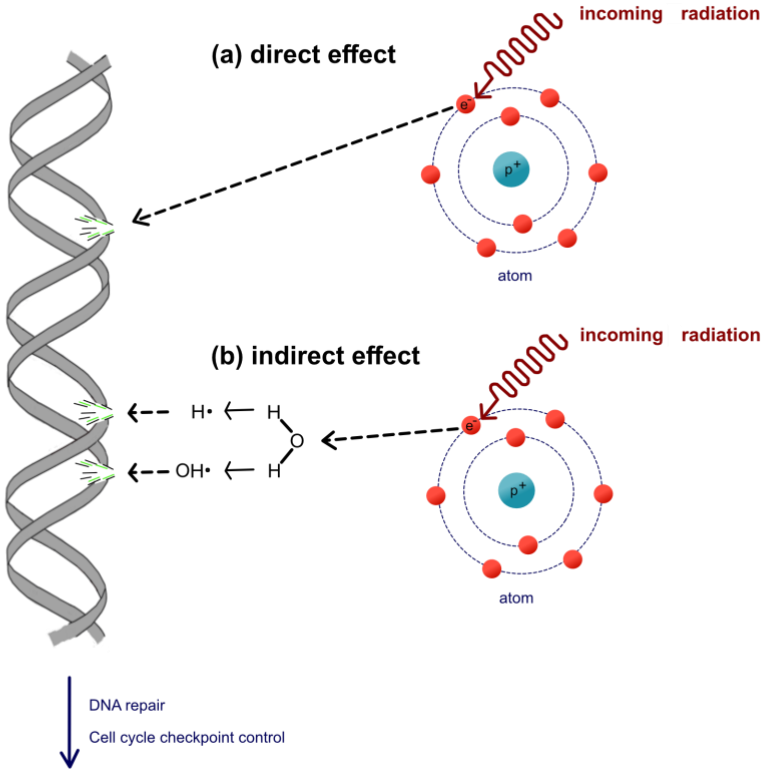

Figure 1. DNA damage by radiation through the direct and indirect effect.
Schematic representation IR-induced DNA damage mechanisms. (A) The direct effect occurs when an electron released through IR directly damages DNA. (B) The indirect effect occurs when free radicals, produced through IR interactions with other molecules, diffuse through the cell and damage the DNA molecule.

For instance, secondary electrons released through ionization, break the covalent bonds of the DNA backbone resulting in single- or double strand breaks. High LET particles mainly work through direct effect. The indirect effect of radiation occurs when free radicals, produced through interaction with other atoms and molecules within the cell, diffuse through the cell and thus damage the target. The cell consists primarily of water (80%) thus, most free radicals created are short lived, but extremely reactive water ions (H_2O^+), which in turn react with further water molecules creating a hydroxyl radical (•OH) and a hydronium ion (H_3O^+).

$$H_2O \rightarrow H_2O^+ + e^- \ (ionisation)$$
$$H_2O^+ + H_2O \rightarrow H_3O + OH\cdot$$

Additional Hydroxy radicals may also be released through the homolysis of water molecules:

$$H_2O \rightarrow H\cdot + OH\cdot \ (splitting)$$

These highly reactive free radicals may only diffuse across a short distance, however, it is sufficient to reach the critical target and cause significant biological damage. Approximately 60-70% of damage caused by low LET radiation is a consequence of the indirect effect.

3.2 DNA damage response (DDR)

IR-induced DNA damage can manifest itself in numerous ways including base modifications, loss of bases, sugar backbone alterations, DNA-DNA crosslinking, DNA-protein crosslinking, bulky lesions, *single strand breaks* (SSB), and the most detrimental, *double strand breaks* (DSB) (Shibata, Jeggo, 2019). A 1Gy X-Ray irradiation produces approximately 1000-2000 base modifications, 800-1600 sugar molecule modifications, 500-1000 SSB, 150 DNA-protein crosslinks, and 50 DSBs and bulky lesions. Maintenance of DNA integrity throughout the cell cycle is paramount to cell survival, therefore, DNA damage sensing and repair pathways have evolved collectively known as the *DNA-damage response* (DDR). The DNA damage response not only encompasses sensing of DNA damage, but pathways are also triggered following IR-induced DNA damage, and include base excision repair, nucleotide excision repair, mismatch repair and single strand break repair. Although SSBs and base loses are most frequent, they have little consequence on cell survival as they are rapidly and efficiently repaired. Conversely, repair of DSBs is exceedingly complex and error prone. It can be achieved through numerous pathways including *non-homologous end joining* (NHEJ) (which can occur at any point during the cell cycle), *homologous recombination* (HR) (limited to late S- and G2 phase), alternative-NHEJ and single strand annealing (Bennardo et al., 2008; Liu, Huang, 2014; San Filippo et al., 2008). A single unrepaired or misrepaired DSB in a specific gene region could be enough to influence cell fate through chromosome breaks at essential genes (Shiloh, Lehmann, 2004; van Gent et al., 2001).

3.2.1 DNA damage response signaling cascade

The DDR is a complex signal cascade comprising of DNA-damage sensors, transducers and effectors whose activation influences DNA-damage repair mechanisms, cell fate and cell-cycle checkpoint activation (Figure 2). DNA-damage is recognized, a DNA repair cascade is activated, and a pause in cell-cycle is mediated to facilitate repair. Cell cycle checkpoints prevent progression into the next cell cycle phase and occur between G1/S phase (G1/S checkpoint), within S phase (intra-S checkpoint), transitioning from G2 phase to mitosis (G2/M checkpoint) and within mitosis (intra-M checkpoint) (Barnum, O'Connell, 2014). Should DNA-damage be too extensive, cells may undergo cell death (apoptosis) or exit the cell cycle permanently (senescence) thereby avoiding propagation of possible mutated cells, reducing the risk of cancer and other age-related diseases. The initial DNA-damage response is triggered through localization of DNA-lesion specific DNA-damage sensor proteins such as PARP 1/2 and Ku70/80 directly to site of damage (Zhou, Elledge, 2000). Consequent signal cascade activation results in recruitment of factors to DNA damage sites whose exact order and timing is thought to influence choice of repair options and cell cycle-arrest. Four primary mediators of the DDR are *phosphoinositide 3-kinase-related kinases*

(PIKKs), *DNA-dependent protein kinase* (DNA-PK), *ataxia-telangiectasia mutated* (ATM) and *ataxia telangiectasia and Rad3-related protein* (ATR) (Figure 2) (Gottlieb, Jackson, 1993; Matsuoka et al., 2007).

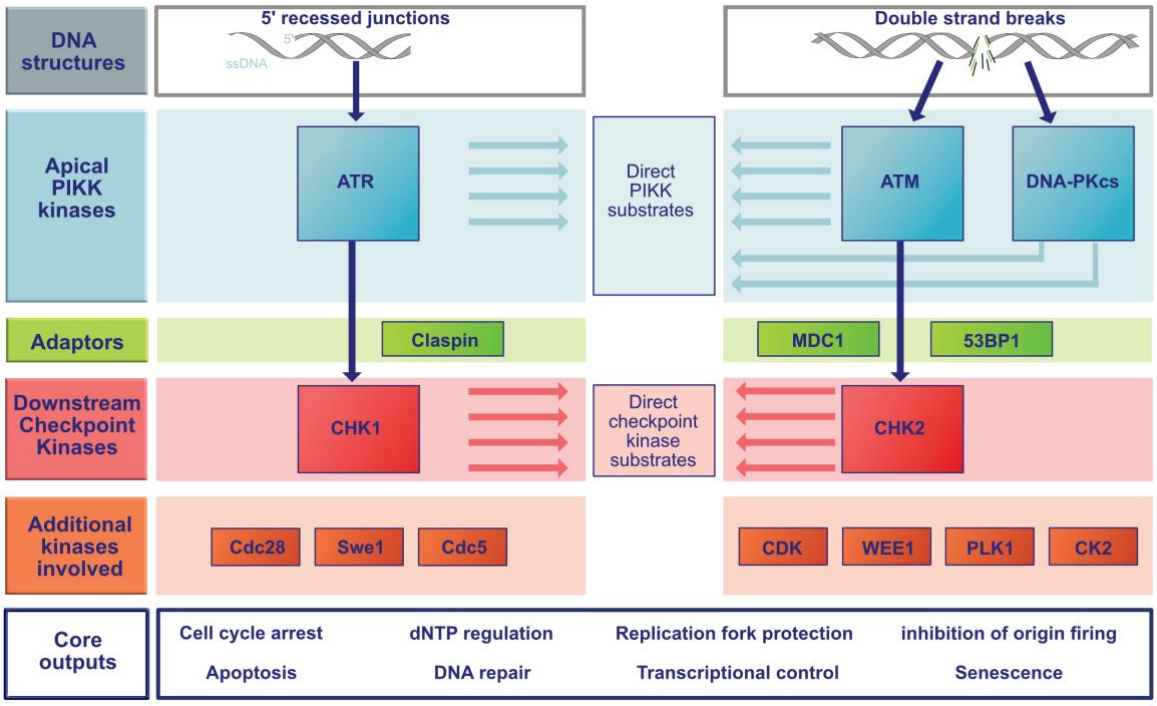

Figure 2. DNA damage signalling cascade via PIKKs in humans.
Schematic representation of DDR signalling pathway initiation with respect to varying DNA structures including SSBs and DSBs. ATR is recruited to RPA-coated single strand DNA, whereas, ATM and DNA-PKcs associate with free ends formed through DSBs. These apical kinases localize to respective DNA structures and trigger a signalling cascade directly, or through adaptor proteins that mediate phosphorylation from apical kinases to downstream checkpoint kinases. Diagram adapted from Lanz et al (Lanz et al., 2019).

Checkpoint adapter proteins are utilized to mediate ATM and ATR phosphorylation transfer to checkpoint effector kinases. ATR primarily relies on Claspin to mediate *Checkpoint kinase 1* (CHK1) activation whereas ATM uses *Mediator of DNA damage checkpoint protein 1* (MDC1) and *Tumor Protein P53-Binding Protein* (53BP1) for *Checkpoint kinase 2* (CHK2) activation (Goldberg et al., 2003; Kumagai, Dunphy, 2000; Peng, Chen, 2003; Stewart et al., 2003; Wu et al., 2008). Within minutes of DSB induction, histone H2A.X is phosphorylated at Serine 139, MDC1 binds to this phosphorylated H2A.X (γH2A.X), and MDC1 is phosphorylated by ATM thereby supporting CHK2 activation (Goldberg et al., 2003; Rogakou et al., 1999; Rogakou et al., 1998; Stewart et al., 2003; Stucki et al., 2005; Wu et al., 2008). This MDC1 phosphorylation, together with *Ring Finger Protein 8* (RNF8) and *Ring Finger Protein 168* (RNF168) ligase recruitment, results in H2A ubiquitination which is directly recognized by 53BP1 (Hustedt, Durocher, 2016). Direct interaction occurs between 53BP1 and CHK2, however, the main mechanism of CHK2 regulation by 53BP1 is thought to be more complex as CHK2 and 53BP1 interaction decreases rapidly post-IR and does not stabilize (Wang et al., 2002). ATM-mediated phosphorylation is also linked to suppression of

DNA-end resectioning within DNA-damage repair, highlighting the complexity and interplay of proteins within the DNA damage response as a whole (Bothmer et al., 2011; Ferrari et al., 2015). Incidentally, recruitment of early repair mediators γH2A.X and 53BP1 can be visualized as distinct foci using microscopy techniques and are often used as reliable markers for DSB identification (Paull et al., 2000; Wang et al., 2002).

3.2.2 Homologous recombination (HR)

Homologous recombination is an elegant and error free DSB repair solution, in which the sister chromatid is used as a template to restore the damaged chromatin (Figure 3) (Betermier et al., 2014; Sonoda et al., 2006). Therefore, it primarily occurs in S and G2 phase when the sister chromatid becomes available. The MRN complex consisting of *meiotic recombination 11 homolog 1* (MRE11), *ATP-binding cassette–ATPase* (RAD50), and phosphopeptide-binding *Nijmegen breakage syndrome protein 1* (NBS1), is one of the first responders at the DSB site, where it is involved in cell-cycle checkpoint signaling and repair protein recruitment (Maser et al., 1997; Nelms et al., 1998). Free 5' ssDNA ends at DSBs are resected to expose the 3' ssDNA ends through *C-terminal-binding protein interacting protein* (CtIP), *exonuclease 1* (EXO1), *Bloom syndrome protein* (BLM), DNA2 nuclease/helicase, and numerous other chromatin remodeling factors (Mimitou, Symington, 2009; Symington et al., 2014). Exposed 3' ssDNA ends are rapidly bound by *replication protein A* (RPA) to hinder degradation and remove secondary structure of ends (Haruta et al., 2006; San Filippo et al., 2008; Sung, 1997). Mediator proteins such as *breast cancer type 2 susceptibility protein* (BRCA2) then mitigate replacement of ssDNA-binding proteins with Rad51 family of DNA recombinases, resulting in the formation of filamentous presynaptic complexes required for homologous strand search (Bianco et al., 1998; Chen et al., 2015; Haruta et al., 2006; New et al., 1998; San Filippo et al., 2006; Shinohara, Ogawa, 1998; Symington, 2002; Yang et al., 2005b). Once the homologous donor strand has been located, presynaptic complexes catalyze strand invasion resulting in formation of an intermediated D-loop, and pairing of ssDNA with homologous donor strand (Solinger, Heyer, 2001). The 3' ssDNA end acts as a primer for DNA polymerase, which begins repair of damaged ends with use of template donor strand and ligation of newly synthesized ends creates Holliday junctions (Haber et al., 2004; Holliday, 2007). Subsequent resolution of Holliday junctions through DNA strand cleavage produces either crossover or non-crossover products (Shah Punatar et al., 2017).

3.2.3 Non-homologous end-joining (NHEJ)

When a DSB occurs and NHEJ is initiated, the last 3-4 base pairs (bp) of the free DNA ends become encircled with, and bound to, the ku70/80 *(X-ray repair cross-complementing protein 6/ X-ray repair cross-complimenting protein 5)* heterodimer ring forming a ku/DNA complex. (Figure 3) (Walker et al., 2001). One side of the ring protects one side of the DNA-double helix by forming a cradle around it, while the other side is more open, presumably to allow access for further repair proteins (Jackson, 2002). As with other DNA repair processes, NHEJ requires a nuclease, polymerase and ligase for completion.

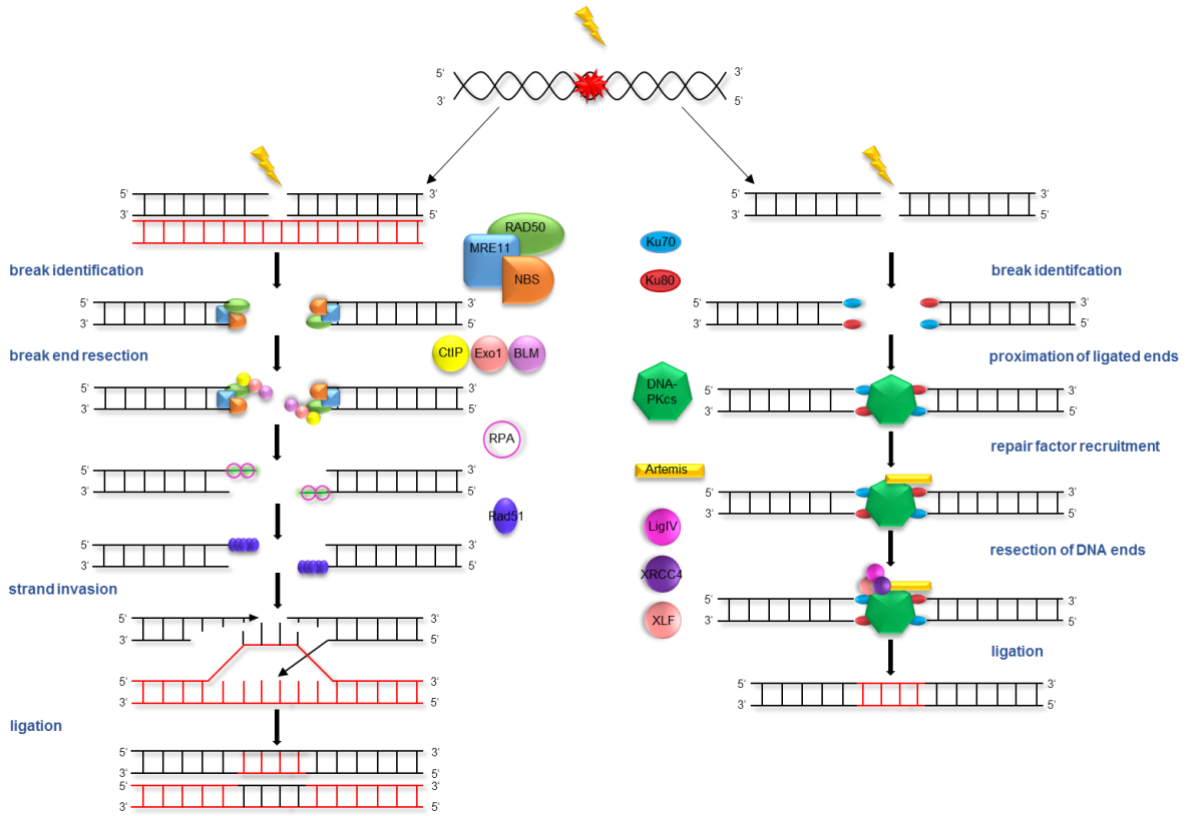

Figure 3. Schematic representation of homologous recombination (left) and non-homologous end-joining (right) DNA DSB repair pathways.

Due to the complex and flexible nature of NHEJ, the ku/DNA complex can recruit these in any order (Lieber, 2008; Ma et al., 2004). If DNA ends are undamaged and complementary, the *X-ray repair cross-complementing protein 4* (XRCC4), which upon recruitment forms a complex with *Cernunnos-X4-like factor* (Cer-XLF), holds DNA ends in close proximity while XRCC4-associated DNA ligase IV reattaches the two ends (Reynolds et al., 2012). However, in most cases free ends require further processing, which is why the ku heterodimer recruits DNA-PK and through its binding activates its *catalytic subunit* (DNA-PKcs), forming the DNA-PK holoenzyme (Smith, Jackson, 1999). It is postulated that this complex holds the free ends in close proximity to aid re-ligation and prevent degradation, as well as, participation in other recombinant events. So far, this complex has only been found in vertebrates and is thought

to aid in overcoming repressive chromatin effects associated with higher eukaryotes (DeFazio et al., 2002; Jackson, 2002; Weterings et al., 2003). Subsequently, the endonuclease Artemis is recruitment and phosphorylated, formatting the DNA-PKcs/Artemis complex and enabling endonucleaic cutting of an array of damaged DNA overhangs (Ma et al., 2005; Yannone et al., 2008). Acting in concert with XRCC4 and Cer-XLF, DNA-Ligase IV can then flexibly re-ligate the various forms of free DNA ends (Gu et al., 2007a; Gu et al., 2007b). The effectiveness of DNA-damage repair is not only influenced by the nature of the damage and the repair process applied, but is also by the chromatin context in which it occurs (Dinant et al., 2008; Hauer, Gasser, 2017).

3.3 Chromatin architecture

Chromatin, simply put, is the combination of DNA and specific packaging proteins whose unique interactions allow meters of genetic material to be compacted into a µm sized cell nucleus. The average human genome is over 3 billion bp in length and the elementary repeating unit of chromatin, known as a nucleosome, consists of 147 bp of DNA wrapped around an octamer of core histone proteins 1.65 times in a left-handed super helix. This octamer core is comprised of two of H2A, H2B, H3 and H4 histone molecules (Kornberg, 1974; Luger et al., 1997). Each nucleosome is coupled to the next by linker DNA of varying lengths, and this level of chromatin packaging is known as the 10-nm beads-on-a-string array (Woodcock et al., 1976). Chromatin is further condensed by linker histone H1, and additional chromatin chaperones pulling together individual nucleosomes creating the 30nm fiber, which in turn, folds into loops averaging 300nm in length (Tremethick, 2007). Subsequent packing and folding of 300nm loops ensues, resulting in 250nm-wide fibers. Tight curling of these fibers eventually result in the highly compact mitotic chromosome. Chromatin is a dynamic structure constantly rearranging, decompacting and recompacting to facilitate the diverse states a cell finds itself in, and the processes it undergoes, including replication, transcription and DNA repair. This chromatin remodeling is achieved through incorporation of additional histones, linker histones, switching of canonical histones with non-canonical core histone variants and post-translational modifications of histone tails (Henikoff, Smith, 2015; Marzluff, Duronio, 2002).

3.3.1 Histones and their post-translational modifications

Histones are highly conserved in eukaryotic cells and, although each of the four core histones show low sequence homology, they each contain the structural motif known as the histone fold (Arents, Moudrianakis, 1995). The histone fold, comprised of three α-helices joined by two loops, facilitates formation of the handshake motif. This refers to the heterodimeric

interactions formed among core histones within the nucleosome (one H3-H4 tetramer and two H2A-H2B dimers) aiding nucleosome stability (Arents and Moudrianakis 1995). Additionally, each histone possesses an N-terminal tail protruding from the nucleosome that influences nucleosome stability, as well as, effecting degree of chromatin fiber condensation and chromatin dynamics (Ausio, Dong et al. 1989, de la Barre, Angelov et al. 2001, Ferreira, Somers et al. 2007, Kan, Lu et al. 2007, Sperling and Grunstein 2009). Histone tails are rich in basic amino acids and subject to a vast array of post- translational modifications (PTMs) including acetylation, methylation, phosphorylation, terminal tail. They extend from the center of the nucleosome and are involved in nucleosomal translocation by chromatin remodelers and other protein interactions effecting chromatin conformation (Vogler, Huber et al. 2010). Histone PTMs are an element of the "histone code", referring to the process in which chromatin conformation is brought about through enzymatically evoked chemical changes of histones, thus contributing to genomic transcription regulation (Strahl and Allis 2000).

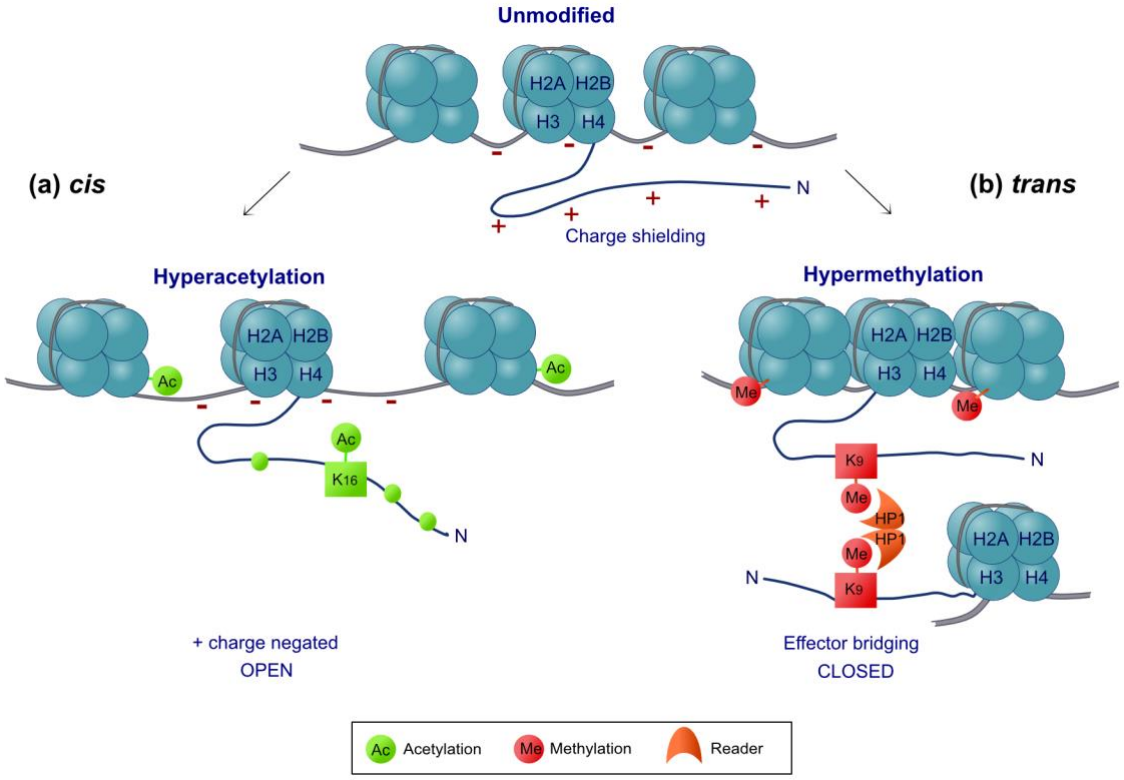

Figure 4. Basic mechanisms utilising covalent histone modifications.
Schematic depiction of cis and trans mechanisms using covalent histone modifications. N terminal histone tails within unmodified nucleosomes may contain high numbers of positive charges due to Lysine and Arginine residues resulting in 'charge shielding'. Close association between N terminal tails and negatively charged DNA may thus be permitted resulting in compaction of chromatin. (A) *Cis* mechanisms function by changing electrostatic interactions, and thus altering intra- and inter nucleosomal contacts. The example shows acetylation of H4 Lysine residues, in particular K16. Acetylation neutralizes positive charges of Lysine residues leading to decondensed 'OPEN' chromatin structure facilitating transcriptional activation. (B)*Trans* mechanisms function indirectly, acting in conjunction with non-histone effector proteins ('readers') who identify and bind specific histone modifications causing downstream functional consequences. The example depicts heterochromatin protein 1 (HP1) binding to the repressive histone mark methylated K9 on histone H3 N terminal tail. HP1 binding facilitates heterochromatin formation leading to the 'CLOSED' chromatin formation associated with gene silencing. Diagram adapted from Wang et al (Wang et al., 2007).

A primary example being the heterochromatin-associated H3 trimethylated at lysine 9 (H3K9me3), which constitutively forms domains of tightly packed repressive chromatin preventing binding of transcription factors. Conversely, H3 acetylated at lysine 9 (H3K9ac) is strongly linked to active gene promoters (Karmodiya, Krebs et al. 2012, Ninova, Fejes Toth et al. 2019). These covalent modifications are generalized into two categories; 'cis' and 'trans' based on their mode of function (Figure 4) (Kouzarides 2007). In cis mechanisms, alterations of steric or charge interactions result in altered intra- and inter nucleosomal contacts. Trans mechanisms on the other hand employ non-histone 'readers' which bind to specific histone modifications and thus influence functionality (Wang, Allis et al. 2007).

3.3.2 Histone variants

A further influential factor in chromatin architecture is the presence of histone variants. The majority of histones are synthesized during S-phase (canonical), in which preexisting histones are dispersed and newly synthesized histones are quickly deposited behind the replication fork in the remaining gaps (Krude 1999). Unlike canonical histones, non-canonical histone variants can replace S-phase histones in a replication-independent manner resulting in differentiated chromatin states (Henikoff and Smith 2015). Oftentimes, histone variants distinguish themselves from their core counterparts by minor variations in amino acid sequence, however, these are sufficient to cause a substantial shift in chromatin architecture. Possible alteration or elimination of PTM-patterns accompanying switching of canonical to non-canonical histones, for example, shows drastic effects on chromatin architecture and highlights that histone switching could conceivably reprogram epigenetic states normally associated with histones and their modifications (Henikoff, Smith, 2015). Aside from structural differences, core histones also differentiate in their tendency to variegate, which is thought to be due to their different localizations within the nucleosome being susceptible to varying evolutionary forces. In humans, H2A and H3 have shown the highest propensity to diverge whereas H2B and H4 show dramatically lower paralog numbers with only one known isotype of H4 (Hake, Allis, 2006; Long et al., 2019; Macadangdang et al., 2014; Postberg et al., 2010).

3.3.3 H2A.J, a novel histone variant

The focus of this work is the histone variant H2A.J, a minimally studied variant only found in mammals. H2A.J is differentiated from all other H2A species through an Alanine-Valine substitution at position 11 and through the presence of an SQK motif at the C-terminus (Supp. 1) (Contrepois et al., 2017). In humans, the H2afj gene is located on chromosome 12 near a gene for H4. It has two known isoforms, isoform-1 resulting from splicing of 2 introns and isoform-2 which does not require splicing of introns (Ota et al., 2004; Strausberg et al., 2002).

There are numerous gene copies throughout the genome for replication-coupled histones (RC) such as H4, for which there are 14, and they are usually found in clusters comprising various RC histone genes. For this reason the proximity of H2afj is an interesting point as it, like many histone variants, is replication independent (Lopez et al., 2012; Nishida et al., 2005) and the first paper investigating H2A.J on a protein level by Contrepois et al. found that H2A.J accumulates in replicate and ETO-induced senescence (Contrepois et al., 2017). The function of H2A.J is yet unknown, however, it is known to promote inflammatory gene expression in ETO-induced senescence (Contrepois et al., 2017). The mechanism through which H2A.J function is yet to be elucidated, as biochemical and structural analysis of H2A.J-containing nucleosome showed only that the thermal stability of the H2A.J-H2B dimer is slightly higher than the canonical H2A-H2B dimer (Tanaka et al., 2020). Enhanced thermal stability is thought to be due to the increased hydrophobicity of H2A.J, as a result of the Alanine-Valine substitution at position 11 (Tanaka et al., 2020). The C-terminal SQ motif did not have a functional effect on the thermal stability, however, it is essential for the function of H2A.J in promoting inflammatory gene expression (Contrepois et al., 2017; Tanaka et al., 2020).

3.4 Senescence

Senescence describes a stress-response state in which cells undergo an irreversible proliferation arrest while maintaining metabolic viability (Munoz-Espin, Serrano, 2014). Numerous positive functions have been identified for senescence including tumor-suppression, embryonic development and wound healing (Demaria et al., 2014). Contradictorily, it has been labeled as a fundamental ageing mechanism, contributing to ageing itself, as well as, age-related diseases and cancer development (Childs et al., 2014; Chinta et al., 2015; Lee, Schmitt, 2019). Thus defining senescence as an antagonistically pleiotropic function in which its consequence depends on biological context.

3.4.1 Replicative senescence

There are numerous types of senescence characterized through their induction processes including replicative senescence, developmental senescence, oncogene-induced senescence, and DNA-damage-induced senescence (d'Adda di Fagagna, 2008; Hayflick, Moorhead, 1961; Muñoz-Espín et al., 2013; Serrano et al., 1997). Furthermore, senescence can be broadly divided into two forms: programmed (replicative and developmental) senescence and premature senescence. Replicative or cellular senescence, as it is now known, was first described in the 1960s by Hayflick & Moorhead after observing the limited replicative capacity of cultured diploid fibroblasts. This later became known as the 'Hayflick

Limit' (Hayflick, Moorhead, 1961). *Replicative senescence* (RS) is induced through telomeric erosion. With each cell division, the protective repetitive DNA sequences at the ends of chromosomes that comprise telomeres, become shorter and shorter. This is due to the unidirectionality in which DNA polymerase moves along each strand and the use of RNA-based primers which, by binding to the DNA in their primer function, inevitably block replication of that specific DNA sequence (Bodnar et al., 1998; Lendvay et al., 1996). Eventually, telomeres become critically shortened triggering prolonged DDR resulting in upregulation of cell cycle progression inhibitors causing senescence-associated growth arrest (d'Adda di Fagagna et al., 2003).

3.4.2 Developmental senescence

Developmental senescence plays an essential role in mammalian embryonic development and is induced by a separate pathway to replicative senescence in a P21-dependent manner (Banito, Lowe, 2013). P21, or *Cyclin-Dependent Kinase Inhibitor 1*, functions as a regulator of cell cycle progression at G1 (Waldman et al., 1995; Xiong et al., 1993). The significance of programmed senescence was demonstrated in mice, where down-regulation of P21 lead to reduction of programmed senescence resulting in severe developmental defects (Munoz-Espin et al., 2013). It is hypothesized that following programmed senescence at different embryonic locations, macrophages invade said tissue, clear senescent cells and thus promote tissue remodeling (Muñoz-Espín et al., 2013).

3.4.3 Oncogene-induced senescence

Oncogene-induced senescence (OIS) and DNA damage-induced senescence both fall into the category of *stress-induced premature senescence* (SIPS). Oncogene-induced senescence may be initiated following hyper-activation of oncogenes including B-raf, K-ras, NF1 and PTEN, which has been shown both *in vitro* and *in vivo* (Chen et al., 2005; Courtois-Cox et al., 2006; Dankort et al., 2007; Michaloglou et al., 2005; Sarkisian et al., 2007). OIS is regulated by a complex signaling network which varies depending on the genetic mutation/oncogene-upregulation and on the tissue in which it occurs. Although they may use varying intermediaries, one common feature which can be found in OIS however is that all signaling functions through tumor suppressors Rb and *tumor protein 53* (p53) (Courtois-Cox et al., 2008).

3.4.4 DNA damage-induced senescence

DNA damage-induced senescence may be caused by exogenic factors such as genotoxic/cytotoxic drugs, large presences of *reactive oxygen species* (ROS) and IR (Chen

et al., 1995; Lee et al., 1999; Macip et al., 2002). The senescence-associated growth arrest, in this case, is maintained by p53 whose activation is upheld by a protracted DDR associated with DNA damage-induced senescence. The transient proliferative arrest seen in acute DDR is mediated through p21, one of p53s most important targets (Rodriguez, Meuth, 2006). Extended cell cycle arrest however, ultimately leads to cyclin-dependent kinase inhibitor $p16^{INK4a}$ upregulation triggering transcriptional regulator Rb activation (Stein et al., 1999), and resulting in senescence-associated permanent cell cycle arrest (Childs et al., 2014). IR-induced senescence has shown upregulation of genes associated with DNA repair, cell-cycle control and cell proliferation, including p53 and p16, all of which play an essential role in modulating IR-induced senescence (Iliakis, 1997; Iliakis et al., 2003; Kim et al., 2014). The mechanism determining whether a cell undergoes apoptosis or enters senescence following DNA damage of a certain magnitude is unknown. It is postulated that this choice depends on factors such as cell type, nature of the DNA damage, duration of DNA-damaging agent exposure and intensity (d'Adda di Fagagna, 2008).

3.5 Characteristics of senescent cells

Apart from permanent exit of the cell cycle, senescent cells undergo substantial changes including enlarged and flattened morphology, increased lysosomal activity, chromatin rearrangements in the form of *senescence-associated heterochromatin foci* (SAHF) and *DNA segments with chromatin alterations reinforcing senescence* (DNA-SCARS), as well as, an altered inflammatory phenotype known as the *senescence-associated secretory phenotype* (SASP).

3.5.1 Senescence-associated secretory phenotype (SASP)

The SASP is a specific inflammatory secretory phenotype displayed by most senescent cells encompassing a vast array of signaling factors such as chemokines, interleukins, growth factors, as well as, secreted proteases and secreted insoluble proteins/extracellular matrix components. However, few common factors are shared between cell types. Mode of senescence induction can also influence increase fold of secretion and which SASP factors are included (Freund et al., 2010). It is thought to function as a beacon to innate immune cells which migrate into tissue and clear present senescent cells, thus leading to tissue regeneration and reestablishment of function (Krizhanovsky et al., 2008; Sagiv et al., 2013). Additionally, it functions in the reinforcement of the senescence-associated growth arrest through a feedback loop including SASP factors such as *Insulin-like growth factor-binding protein 7* (IGFBP-7), *growth regulated oncogene*-alpha (GROalpha/CXCL1), *interleukin 6* (IL-6) and *interleukin 8* (IL-8) (Acosta et al., 2008; Kuilman et al., 2008; Wajapeyee et al., 2008;

Yang et al., 2006). The SASP, however, can also have deleterious effects on surrounding cells by inducing cell-surface receptor activation and corresponding signal transduction pathways, thus promoting numerous pathologies. For one, it is considered a type of chronic inflammation. It has been implicated in contributing to the rise in inflammatory factors associated with ageing (termed 'inflammaging') and other age-associated diseases such as atherosclerosis (Franceschi, Campisi, 2014; Minamino et al., 2003). Strikingly, a propensity of SASP factors in the promotion of epithelial cell growth, both of premalignant and malignant cells, has been observed in numerous tissues and cells. These include mammary epithelial cells (Coppe et al., 2008; Krtolica et al., 2001; Parrinello et al., 2005) and prostate tumor xenografts (Yang et al., 2005a), as well as, in emergence of cancer stem-like cells in Multiple Myeloma (Cahu et al., 2012). Factors included in the SASP such as *hepatocyte growth factor* (HGF), IL-6 and IL-8 have also been verified to promote cancer cell invasiveness in culture (Birchmeier et al., 2003; Coppe et al., 2008; Ohuchida et al., 2004). Interestingly, knock-down of H2A.J in ETO-induced senescence has been shown to mitigate SASP in lung fibroblasts (Contrepois et al., 2017). The mechanisms of which however, are yet unknown. SASP induction is a highly complex mechanism. As with senescence itself, SASP manifestation depends on numerous factors including cell type and mode of senescence induction. *Nuclear factor kappa-light-chain-enhancer of activated B cells* (NF-κB) signaling is crucial to SASP induction and its activation is initiated through the DDR response in an ATM dependent manner and, synergistically, through *p38 mitogen-activated protein kinases* (p38MAPK) functioning in a DDR-independent manner (Chien et al., 2011; Crescenzi et al., 2011; Freund et al., 2011; Rodier et al., 2009; Rovillain et al., 2011; Salminen et al., 2012).

3.5.2 DNA segments with chromatin alterations reinforcing senescence (DNA-SCARS)

As with an acute DDR (up to 24-48h post DNA-damage induction), DNA damage-induced senescent cells also display cytologically detectable nuclear foci containing 53BP1 and γH2AX, however, these foci are found to be fewer in number and larger in size. Additionally, these persisting DNA damage foci have undergone successive changes distinguishing them from actively repairing DNA damage sites, not only in structure but also in function. Thus, they have been termed DNA-SCARS (Rodier et al., 2011a). Disparities include ssDNA absence, no RPA70 and RAD51 repair proteins, decreased 53BP1 solubility, prolonged presence of activated p53 and CHK2, and *promyelocytic leukemia protein nuclear bodies* (PML-NB) association. DNA-SCARS are required for senescence-associated growth arrest and their de-stabilization through γH2AX depletion resulted senescence-associated growth arrest reversal after senescence-inducing 10Gy IR exposure (Rodier et al., 2009; Rodier et al., 2011a). DNA-SCARS de-stabilization through γH2AX deficiency also resulted in

reduction of SASP associated IL-6 secretion suggesting DNA-SCARS are critical in maintenance of senescent phenotypes (Rodier et al., 2011a).

3.5.3 Senescence-associated heterochromatin foci (SAHF) and nuclear lamina

Senescent cells undergo additional large structural changes with regards to morphology, chromatin organization and nuclear lamina structure. The major reorganization which chromatin undergoes upon entry into senescence is the formation of SAHF which can be identified microscopically as *4',6-diamidino-2-phenylindole* (DAPI) -dense punctate DNA foci (Narita et al., 2003b). SAHF possess a distinct structure featuring a heterochromatin core enriched in H3K9me3, surrounded by a layer of facultative heterochromatin marker H3K27me3 enriched chromatin. SAHF are distinct from constitutive heterochromatin regions such as centromeres and telomeres (Funayama et al., 2006; Narita et al., 2003b; Zhang et al., 2007) (Chandra et al., 2012). Presence of extra heterochromatin markers such as *heterochromatin protein 1* (HP1) and macroH2A are common (Narita et al., 2003b; Zhang et al., 2005). Each SAHF consists of one condensed chromosome (Funayama et al., 2006; Zhang et al., 2007) and thus can contain several proliferation-promoting genes thought to be contained within the transcriptionally-silent heterochromatin core. This mechanism is thought to repress the expression of these genes and thereby SAHF reinforce senescence-associated growth arrest (Adams, 2007). Additionally, SAHF reinforce senescence-associated growth arrest as they contain E2F target gene promotors, whose suppression is a crucial step in growth arrest maintenance and they do not contain any active transcription which further supports their role in assisting cell cycle exit in senescence (Narita et al., 2003b). The outermost layer is rich in histone *H3 lysine 36 trimethylated* (H3K36me3) marks, identifying the transcriptionally active regions (Chandra et al., 2012) thought to harbor the SASP genes (Freund et al., 2010). Dependence of SAHF on the p53-Rb and p16INK4a-Rb pathways has been well described and now focus on the role of chromatin-associated components such as histone variants, histone chaperones and PML-NBs is increasing. Studies conducting *Chromatin Immunoprecipitation DNA-Sequencing* (ChIP-seq) analysis of chromosome wide H3K9me3 and H3K27me3 levels following OIS induction only showed moderate changes in these histone marks whereas chromatin bound HP1 was significantly increased (Chandra et al., 2012; Salama et al., 2014). HP1 binds to H3K9me3, thus data suggest a spatial rearrangement of existing heterochromatin into clusters of regions with similar modifications rather than a large scale redistribution of histone modifications (Chandra et al., 2012; Chandra, Narita, 2013). Various effectors of SAHF formation have been identified including HP1, *Histone repressor A* (HIRA), *Anti-silencing factor 1 a* (ASF1a), Rb-E2F complexes, histone H3.3 and RB phosphatase, all of which congregate at PML-NBs

prior to SAHF formation (Adams, 2007; Corpet et al., 2014; Narita et al., 2003b; Salama et al., 2014; Vernier et al., 2011; Zhang et al., 2007; Zhang et al., 2005).

Closely linked to SAHF formation is the decline of the nuclear lamina with senescence. The nuclear lamina is a complex structural network consisting mainly of filament proteins A- and B-type lamins (Gruenbaum, Foisner, 2015), running along the inside of the nuclear envelope, forming a scaffold linked to chromatin structure maintenance and genome organization. Lamins interact directly or indirectly with a variety of *nuclear envelope transmembrane proteins* (NETs) which link them to the inner nuclear membrane (Schirmer, Foisner, 2007). Well defined (sub)megabase-sized chromatin domains rich in repressive marks known as *lamine-associated domains* (LADs) have been uncovered following genome-wide mapping (Guelen et al., 2013; Pickersgill et al., 2006). Interestingly, it has not only been shown that lamine B1 expression is reduced in senescence (Dreesen et al., 2013a; Freund et al., 2012b; Shah et al., 2013; Shimi et al., 2011), but that in senescent cells, lamine B1 is reduced at LADs and preferentially at the H3K9me3-rich LAD centers (Chandra et al., 2015; Sadaie et al., 2013), thus, supporting the theory that a large-scale spatial reorganization of repressive-histone marked regions takes place to form SAHFs.

3.6 Clinical implications of senescence

Despite senescence having positive implications in tumor-suppression, wound healing and development, it is now recognized as one of nine hallmarks of ageing mechanisms (genomic instability, telomere attrition, epigenetic alterations, loss of proteostasis, deregulated nutrient-sensing, mitochondrial dysfunction, cellular senescence, stem cell exhaustion, and altered intercellular communication) (Lopez-Otin et al., 2013), thus increasingly gathering interest as an area of study in the last 20 years. It has been linked to chronic age-associated illnesses such as Alzheimer's disease, atherosclerosis, osteoarthritis, osteoporosis and Parkinson's disease (Bussian et al., 2018; Childs et al., 2016; Chinta et al., 2018; Farr et al., 2017; Jeon et al., 2017; Musi et al., 2018). Markedly, senescence accumulation has also been implicated in pre-malignant lesion formation in lung, lymphoma, pancreas, prostate and pancreas (Braig et al., 2005; Chen et al., 2005; Collado et al., 2005; Lazzerini Denchi et al., 2005; Michaloglou et al., 2005). Increase in senescent cells with age is not only due to higher levels of DNA-damage and replicative senescence frequency, but also due to impaired immunosurveillance and immunoclearance of senescent cells (Ovadya et al., 2018). Additionally, widely used treatments such as radiotherapy and prolonged chemotherapy have been shown to induce premature senescence, promote tumor recurrence and metastasis (Demaria et al., 2017; Tabasso et al., 2019; Zacarias-Fluck et al., 2015). Radiotherapy-induced senesence has been recognized as a critical mechanism in cerebral glioblastoma relapse by inducing

formation of multinucleated cells and reactivating these (Kaur et al., 2015). Additionally, radiotherapy-induced senescence has been implicated in radiation-induced fibrosis, pulmonary fibrosis, skin fibrosis and ulceration (He et al., 2019; Wang et al., 2019). Application of senolytics, small molecules that target senescent cells and induce apoptosis, have been proposed as possible therapies alongside traditional cancer therapies, some of which have already proven effective in mice showing treatment-induced senescence (Chang et al., 2016; Demaria et al., 2017) .

3.7 Ageing and senescence in the epidermis

The skin is an ideal model to study senescence and ageing, as it presents senescence due to normal physiological ageing of the organism, as well as, premature senescence induced by intrinsic/extrinsic factors such as UV radiation, pollution and ROS (Farage et al., 2008, 2013; Kammeyer, Luiten, 2015; Landau, 2007; Waldera Lupa et al., 2015). Its accessibility also plays a key role in application for ageing studies. The skin is the body's first line of defense acting as a physical barrier to external damaging factors and as a protective layer to underlying tissues.

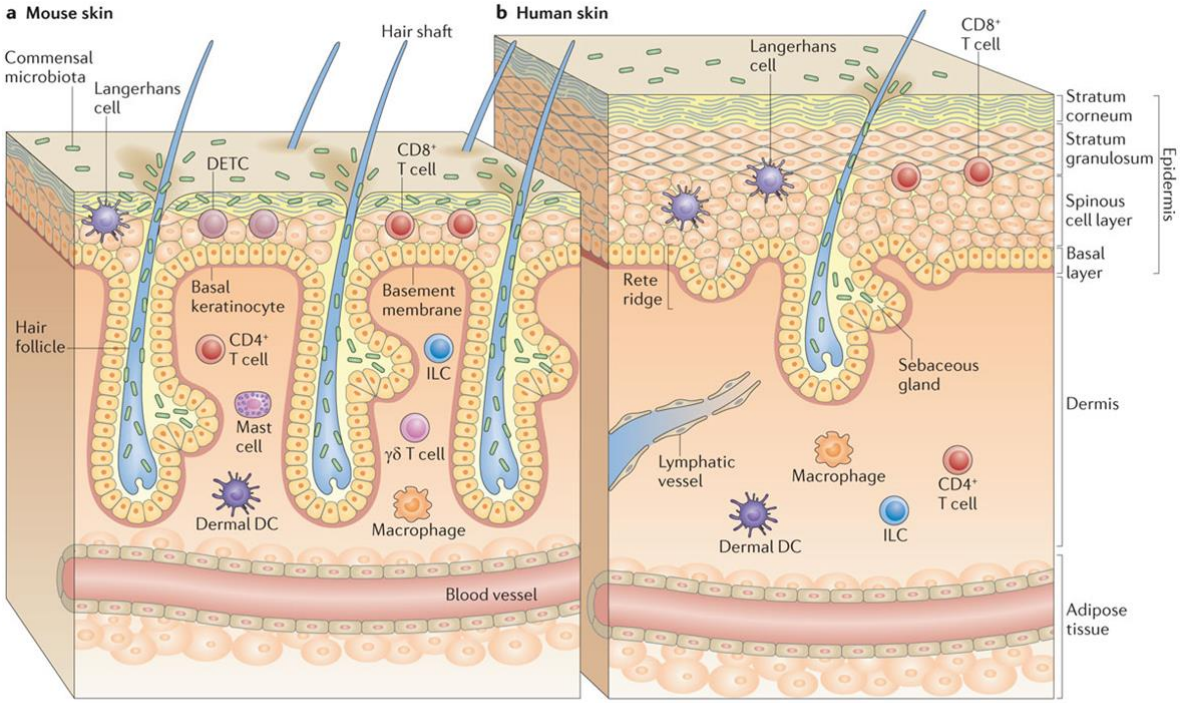

Figure 5. Structure of murine and human skin.
(A) Schematic representation of murine skin showing decreased thickness (~25µm) and increased hair follicle abundance in comparison to human skin. Murine skin also contains Vγ5+ dendritic epidermal T cells (DETC) and γδ T cells absent from human epidermis. (B) Schematic representation of human skin showing much greater thickness of skin in general (~100µm) but also of the epidermis which compared to the 2-3 cell layers of murine skin comprises of 5-10 to layers dependent on organismal age (Zomer, Trentin, 2018). Both human and murine skin also contain immune cell types including Langerhans, other dermal dendritic cells (Dermal DCs), CD8+ T cells, CD4+ T cells, macrophages, mast cells and innate lymphoid cells (ILCs). Diagram taken from Pasparakis et al., 2014 (Pasparakis et al., 2014).

Both human and murine skin are composed of the epidermis, the outer most layer, and the dermis which contain the same cell layers, however, human skin greatly differs in thickness and cell abundance (Figure 5) (Pasparakis et al., 2014). Skin biopsy examinations of this study focused mainly on the epidermis which primarily consists of keratinocytes in various stages of differentiation, melanocytes, Langerhans cells, and Merkel cells (Abraham, Mathew, 2019; Banchereau, Steinman, 1998; Cichorek et al., 2013; Wickert, Visscher, 2006) Keratinocytes begin in the *stratum basale* and differentiate up through the *stratum spinosum,* the *stratum granulosum* and finally transform into the corneocytes that comprise the *stratum corneum* (Wickert, Visscher, 2006). Melanocytes occur at intervals within the *stratum basale* secreting melanin to a network of cells in their vicinity (Cichorek et al., 2013), Langerhans cells are antigen-presenting epidermal dendritic cells found throughout the epidermis (Banchereau, Steinman, 1998), and Merkel cells also localize to the *stratum basale* functioning in neuro-endocrine and mechanoreceptor responses (Abraham, Mathew, 2019). Senescent cells accumulate in the skin in an age-dependent manner and the consequential SASP is implicated as a crucial effector in skin ageing and skin cancer (Dimri et al., 1995; Ghosh, Capell, 2016; Munoz-Espin, Serrano, 2014; Waldera Lupa et al., 2015). Intriguingly, H2A.J positive cells has been shown to accumulate in ageing human epidermis, aged murine epidermis, and murine hair follicles, which house the main stem cell population of the skin (Contrepois et al., 2017; Lavker et al., 2003). Pre-neoplastic lesions induced by the carcinogen *7,12-dimethylbenz(a)-anthracene* (DMSA) also showed increased H2A.J and $P16^{INK4a}$ levels in murine epidermisPapilloma cells were negative for both H2A.J and P16INK4a, however, the papilloma-adjacent skin showed H2A.J and $P16^{INK4a}$ positive cells (Contrepois et al., 2017).

4 Aim of work

Radiotherapy is an irreplaceable tool in cancer treatment, however its DNA-damaging properties may be accompanied by an array of short- and long-term side effects such as inflammation and fibrosis. The aim of this work is to investigate a possible connection between the novel histone variant, H2A.J, ionizing radiation and radiation-induced senescence. To date it has only been shown that H2A.J accumulates in the murine epidermis following low dose fractionation of 50x 0.1Gy, 72h post irradiation. Here we utilise a mainly *in vitro* approach working with H2A.J knock-down WI-38 lung fibroblast to gain further insights into the accumulation kinetics, longevity, DNA-damage response influence, gene expression and chromatin structure consequences of H2A.J incorporation following ionizing radiation.

5 Materials and methods

5.1 Materials and devices

The following section covers all materials and devices utilized in the completion of this project.

5.1.1 Chemicals and reagents

Table 1: Chemicals and reagents

Chemical/reagent	Supplier/Manufacturer
2-propanol	Thermo Fisher, Waltham , MA, USA
Absolute Ethanol	Sigma-Aldrich, St. Louis, MO, USA
Acetic Acid	Sigma-Aldrich, St. Louis, MO, USA
Ammonium persulphate	Thermo Fisher, Waltham , MA, USA
Aqua sterile water	B.Braun, Melsungen, Germany
Aurion Blocking Solution	Aurion, Wageningen, Netherlands
Boric acid	Sigma-Aldrich, St. Louis, MO, USA
BSA	GE Healthcare, Rimbach, German
BSA-c ™ 10%	Aurion, Wageningen, Netherlands
Chloroform	Fluka, Fuchs, Switzerland
Citric acid	Merck, Kenilworth, NJ, USA
Dako Faramount aqueous mounting medium	Agilent, Waldbronn, Germany
Dako REAL target retrieval solution (S2031)	Agilent, Waldbronn, Germany
Dako REAL target retrieval solution (S1699)	Agilent, Waldbronn, Germany
Dimethylsulfoxide	Carl Roth, Karlsruhe, Germany
DNA loading dye	Thermo Fisher, Waltham , MA, USA
Doxycycline hydrochloride	Sigma-Aldrich, St. Louis, MO, USA
Duolink® In Situ Detection Reagents Green (DUO92014)	Sigma-Aldrich, St. Louis, MO, USA
Duolink® In Situ PLA® Probe Anti-Rabbit PLUS (DUO92002)	Sigma-Aldrich, St. Louis, MO, USA
Duolink® In Situ PLA® Probe Anti-Mouse MINUS	Sigma-Aldrich, St. Louis, MO, USA

Chemical/reagent	Supplier/Manufacturer
Duolink® In Situ Mounting Medium with DAPI (DUO82040)	Sigma-Aldrich, St. Louis, MO, USA
Duolink® In Situ Wash Buffers, Fluorescence (DUO82049)	Sigma-Aldrich, St. Louis, MO, USA
EDTA	Carl Roth, Karlsruhe, Germany
Ethidium bromide	Merck, Kenilworth, NJ, USA
Etoposide	Sigma-Aldrich, St. Louis, MO, USA
Fetal bovine serum	Sigma-Aldrich, St. Louis, MO, USA
Paraformaldehyde 32% solution	Science Services, Munich, Germany
Glutaraldehyde 50% solution	Science Services, Munich, Germany
Glycerol	Carl Roth, Karlsruhe, Germany
Glycine	Carl Roth, Karlsruhe, Germany
Immersion oil for microscopy	Merck, Kenilworth, NJ, USA
Isopropanol 70%	Hedinger, Stuttgart, Germany
Isotonic sodium chloride solution for injecting	B.Braun, Melsungen, Germany
L-Glutamine	Sigma-Aldrich, St. Louis, MO, USA
LR-White accelerator	Agar Scientific, Essex, UK
LR- White resin	Plano, Wetzlar, Germany
N,N-Dimethylformamide	Sigma-Aldrich, St. Louis, MO, USA
Magnesium chloride hexahydrate pure	Applichem, Darmstadt, Germany
Methanol	Merck, Kenilworth, NJ, USA
Methylene Blue	Sigma-Aldrich, St. Louis, MO, USA
Minimum Essential Medium non-essential amino acids	Sigma-Aldrich, St. Louis, MO, USA
Minimum Essential Medium, no glutamine, no phenol red	Thermo Fisher, Waltham , MA, USA
Multi-analyte ELISArray™ Human Mix-n-Match kit	Qiagen, Hilden, Germany
Paraformaldehyde	Sigma-Aldrich, St. Louis, MO, USA
Paraplast® paraffin	Carl Roth, Karlsruhe, Germany
Penicillin/Streptomycin	Merck, Kenilworth, NJ, USA

Chemical/reagent	Supplier/Manufacturer
pH 4.0 buffer solution	Hanna Instruments, Vöhringen, Germany
pH 7.0 buffer solution	Hanna Instruments, Vöhringen, Germany
pH 10.0 buffer solution	Hanna Instruments, Vöhringen, Germany
Phosphate Buffered Saline, pH7.2-7.4	University chemist
Pioloform BM18	Plano, Wetzlar, Germany
Potassium ferricyanide	Sigma-Aldrich, St. Louis, MO, USA
Potassium ferrocyanide	Sigma-Aldrich, St. Louis, MO, USA
QuantiTect® reverse transcription kit	Qiagen, Hilden, Germany
QuantiTect® SYBR® Green PCR kit	Qiagen, Hilden, Germany
Rapid Gold BCA protein assay kit	Thermo Fisher, Waltham , MA, USA
Rompun® 2%	Bayer, Leverkusen, Germany
Roti® Immunoblock 10x	Carl Roth, Karlsruhe, Germany
Roti® PVDF membrane, poresize: 0.45µm	Carl Roth, Karlsruhe, Germany
RT-PCR grade water	Invitrogen, Carlsbad, CA, USA
SIGMAFAST 3,3'-Diaminobenzidine tablets	Sigma-Aldrich, St. Louis, MO, USA
Sodium borate	Sigma-Aldrich, St. Louis, MO, USA
Sodium chloride	Carl Roth, Karlsruhe, Germany
Sodium Pyruvate	Sigma-Aldrich, St. Louis, MO, USA
Sudan Black B	Sigma-Aldrich, St. Louis, MO, USA
Triton™ X-100	Carl Roth, Karlsruhe, Germany
Trizol™ reagent	Invitrogen, Carlsbad,, CA, USA
Trypsin/EDTA solution 10%	Merck, Kenilworth, NJ, USA
Tween®20	Carl Roth, Karlsruhe, Germany
Uranylacetate	Merck, Kenilworth, NJ, USA
Urostamin (ketaminhydrochloride 100mg/ml)	Serumwerk, Bernburg, Germany
Vectastain peroxidase standard PK-4000	Vector Laboratories, Peterborough, UK
Vectashield® Hard-set mounting medium with DAPI	Vector Laboratories, Peterborough, UK
X-Gal Biochemica	Applichem, Darmstadt, Germany
Xylol	Hedinger, Stuttgart, Germany

5.1.2 Solutions and buffers

Table 2: Solutions for cell culture

Cell culture	
Doxycycline (DOX) solution	1mg/ml DOX in ethanol Sterile filter. Store at -20°C
Etoposide (ETO) solution	20mM ETO in DMSO Store at 4°C
MEM medium for WI-38 culture	Minimum Essential Medium, no glutamine, no phenol red 10% FBS 1mM sodium pyruvate 2mM L-glutamine 0.1mM NEAAs 1% Penicillin/Streptomycin When applicable: 20µM ETO **and/or** 1µg/ml DOX
Trypsin	Diluted 10 fold in dH_2O. Store at 4°C

Table 3: Solutions and bufffers for immunofluorescence

Immunofluorescence microscopy	
Paraformaldehyde (PFA) fixation solution	4% PFA dissolved in PBS at 60^{o}C pH 6.4 Store in suitable aliquots at -20^{o}C
Sodium azide preservation solution	0.4% BSA 0.02 sodium azide in 500ml PBS Store at 4^{o}C
Triton permeabilisation solution	0.5% Triton-X-100 in 50ml PBS Store at 4^{o}C
Tween wash solution	0.1% Tween-20 in 500ml PBS Store at 4^{o}C
Sudan Black solution	0.01% Sudan Black B in 70% Ethanol Filter before use. Make fresh each time.
DNA acid denaturation solution	2 M HCl in dH_2O Store at RT
BrdU Tween/BSA/PBS wash solution	0.1% Tween, 1% BSA in 500ml PBS. Store at 4^{o}C

Table 4: Solutions and buffers for transmission electron microscopy

Transmission electron microscopy	
Fixation solution	2% PFA 0.05% glutaraldehyde in PBS Make fresh each time.
Incubation buffer	0.1% BSA-c in PBS pH7.4 Store at -20°C in suitable aliquots.
Pioloform coating solution	1.2% Pioloform dissolved in pure chloroform under constant stirring Store at room temperature.
Post-fixation solution	2% glutaraldehyde in PBS. Make fresh each time.
Richardson's Blue solution	Stock 1: 1% Azure II in dH_2O Stock: 2 Methylene Blue in sodium borate. Mix 1:1 and pass through 22μm filter. Store at room temperature.
Uranylacetate	2% uranylacetate in ultra-pure H_2O Store in suitable aliquots at -20°C.

Table 5: Solutions and buffers for immunohistochemistry

Immunohistochemistry	
Antigen retrieval buffer	Dilute antigen retrieval buffer 1:10 in dH_2O Can be used up to 3x if cooled and stored at 4°C after each use.
Blocking buffer	Dilute Roti® Immunoblock 1:10 in dH_2O Store at room temperature for several months.
BSA wash solution	1% BSA in 500ml PBS Store at 4°C for 1 month.
BSA blocking solution	4% BSA in 5ml PBS Store at 4°C for 2 weeks.
Citrate buffer	40mM citric acid 150mM NaCl 2mM $MgCl*6H_2O$ in dH_2O pH to 6.0 Store at 4°C for 6 months.
Permeabilisation solution	0.2% Triton-X-100 in PBS Make fresh each time.
Potassium ferricyanide	100mM potassium ferricyanide in PBS Store in dark at 4°C.
Potassium ferrocyanide	100mM potassium ferrocyanide in PBS Store in dark at 4°C.
Senescence-associated β-galactosidase (SA-β-gal) fixation solution	2% PFA 0.2% glutaraldehyde in PBS Make fresh each time.

Immunohistochemistry	
SA-β-gal stock solution	1mg/ml X-Gal powder in Dimethylformamide Store at -20°C for up to 6 months.
SA-β-gal staining solution	To make 5ml: 4.6ml citrate buffer 100µl X-Gal stock solution 250µl 100mM potassium ferricyanide 250µl 100mM potassium ferrocyanide Light sensitive. Make fresh each time.

Table 6: Solutions for murine perfusion

Perfusion	
Anesthetic	120µg ketamine/g bodyweight 16µg Rompun/g bodyweight
Flush solution	1% Heparin in PBS
Fixation solution	See "Paraformaldehyde fixation solution" above.

Table 7: Human skin biopsy culture

Human epidermal samples- ex-vivo irradiated	
RPMI medium	RPMI 1640 10% FCS 2% Penicillin/Streptomycin

5.1.3 Antibodies

Table 8: Antibodies and dilutions for various technical applications

Antibody	Host	Product no.	Supplier/ manufacturer	IFM	IHC	TEM
Primary antibodies						
Anti-53BP1	Ms	Mab3804	Merck Millipore,	1:500	1:500	1:5000
Anti-53BP1	Rab	IHC-0001	Bethyl, Montgomery, TX, USA	1:5000	-	-
Anti-BrdU	Rat	OBT-0030	Bio-Rad Laboratories, Munich, Germany	1:200	-	-
Anti-H2A.J	Rab	N/A	Produced by Carl Mann	1:1000	1:200	1:200
Anti-H3K9me3	Rab (pAb)	ab8898	Abcam, Cambridge, UK	1:500	-	1:200
Anti-H3K27me3	Ms (mAb)	ab6002	Abcam, Cambridge, UK	1:200	-	1:400
Anti-ki67	Rat	14-5698-82	Thermo Fisher, Waltham，MA, USA	1:600	-	-
Anti-lamine B1	Ms (mAb)	66095-1-Ig	Proteintech, Manchester, UK	1:1000	-	1:300
Anti-p21	Rb	Ab212247	Abcam, Cambridge, UK	1:700	-	-

Antibody	Host	Product no.	Supplier/ manufacturer	IFM	IHC	TEM
Anti-PML	Ms	SC-966	Santa Cruz, Dallas,TX,USA	1:500	-	1:400
Secondary antibodies						
Alexa Fluor 488nm anti-rabbit	Gt	A11034	Invitrogen, Carlsbad, CA, USA	1:1000	1:1000	-
Alexa Fluor 488nm anti-mouse	Gt	A11001	Invitrogen, Carlsbad, CA, USA	1:1000	1:1000	-
Alexa Fluor 568nm anti-rabbit	Gt	A11036	Invitrogen, Carlsbad, CA, USA	1:1000	1:1000	-
Alexa Fluor 568nm anti-mouse	Gt	A11031	Invitrogen, Carlsbad, CA, USA	1:1000	1:1000	-
Alexa Fluor 568nm anti-mouse (IgM)	Gt	A21043	Invitrogen, Carlsbad, CA, USA	1:1000	1:1000	-
6nm Gold-labelled anti-rabbit	Gt	806.011	Aurion, Wageningen, Netherlands	-	-	1:30
10nm Gold-labelled anti-rabbit	Gt	810.011	Aurion, Wageningen, Netherlands	-	-	1:30
6nm Gold-labelled anti-mouse	Gt	806.022	Aurion, Wageningen, Netherlands	-	-	1:30
10nm Gold-labelled anti-mouse	Gt	810.022	Aurion, Wageningen, Netherlands	-	-	1:30

Antibody	Host	Product no.	Supplier/ manufacturer	IFM	IHC	TEM
Goat-anti rat IgG2a FITC coupled	Gt	A110-109F	Bethyl, Montgomery, TX, USA	1:400	-	-
Immunoglobulins/ biotinylated anti-rabbit	Gt	E0432	Agilent, Waldbronn, Germany	-	1:400	-

5.1.4 PCR Primers

Table 9: PCR primers and corresponding annealing temperatures

Primer	Sequence (5'→3')	Annealing temp. (°C)
CCL2	F CAGCCAGATGCAATCAATGCC R TGGAATCCTGAACCCACTTCT	52
CSF2	F TCCTGAACCTGAGTAGAGACAC R TGCTGCTTGTAGTGGCTGG	52
IL6	F ACTCACCTCTTCAGAACGAATTG R CCATCTTTGGAAGGTTCAGGTTG	52
CXCL8	F TTTTGCCAAGGAGTGCTAAAGA R AACCCTCTGCACCCAGTTTTC	52
GAPDH	F ATGGGGAAGGTGAAGGTCG R GGGGTCATTGATGGCAACAATA	52

5.1.5 Consumables

Table 10: Consumables

Consumable	Supplier/manufacturer
BD Microlance™ 3 (26G, 0.5“, 0.45x13mm)	BD Biosciences, Heidelberg, Germany
Cell culture multiwall plates (6 wells)	Greiner Bio-one, Kremsmünster, Austria
Cell Saver pipette tips (200µl)	Biozym, Hessisch-Oldendorf, Germany
Cellstar® Cell culture flasks (75cm^2)	Greiner Bio-one, Kremsmünster, Austria
Centrifuge tubes, non-pyrogenic (15ml)	Sarstedt, Nümbrecht, Germany
Centrifuge tubes, non-pyrogenic (50ml)	Greiner Bio-one, Kremsmünster, Austria
Coverslips #1 (⌀12mm)	Thermo Fisher Scientific, Waltham , MA, USA
Coverslips 24x60mm, strength 1	Meidte, Burgdorf, Germany
Filter discs, grade 292 (ø 90mm,87g/m^2)	Sartorius, Göttingen, Germany
Gelantine capsules (size 4)	Plano, Wetzlar, Germany
Histobond® microscope slides (76x26x1mm)	Marienfeld, Lauda-Königshofen, Germany
Histosette I tissue embedding cassette	Neo Lab, Heidelberg, Germany
Injekt ® single use injections (1ml, 10ml)	B.Braun, Melsungen, Germany
LightCycler® capillaries (20µl)	GeneOn, Ludwigshafen am Rhein, Germany
Light duty one-ply tissue wipes (11.4x20.0cm)	VWR, Darmstadt, Germany
MicroAmp® optical 96-well reaction plate	Applied biosystems, Foster City, CA, USA
MicroAmp™ optical adhesive film kit	Applied biosystems, Foster City, CA, USA
Microscope slides Superfrost® 76x25mm	Carl Roth, Karlsruhe, Germany
Microtome blade A35	Feather Safety Razor, Osaka, Japan
Microtome blade N35	Feather Safety Razor, Osaka, Japan
Nickel grids (2x1mm slit)	Plano, Wetzlar, Germany
Parafilm®	Bemis, Neenah, WI, USA

Consumable	Supplier/manufacturer
Petri dishes (145/20mm)	Greiner Bio-one, Kremsmünster, Austria
PES sterile syringe filters (⌀35mm, 0.45µm)	Thermo Fisher Scientific, Waltham , MA, USA
Pipette tips (10µl, 200µl,1000µl)	Sarstedt, Nümbrecht, Germany
Razor blades	Plano, Wetzlar, Germany
Safelock® centrifuge tubes (1.5ml, 0.5ml)	Eppendorf, Hamburg, Germany
SafeSeal Professional filter pipette tips (10µl, 200µl, 1000µl)	Biozym, Hessisch-Oldendorf, Germany
Safety-multifly®-set (25Gx0.75“ 0.5x19mm)	Sarstedt, Nümbrecht, Germany
Serological pipettes (5ml, 10ml, 25ml)	Sarstedt, Nümbrecht, Germany
Standard pipette tips (10µl, 200µl, 1000µl)	Sarstedt, Nümbrecht, Germany
Sterile surgical blades #11	B.Braun, Melsungen, Germany
Superfrost® microscope slides (76x25mm)	Carl Roth, Karlsruhe, Germany
Weighing pans	Carl Roth, Karlsruhe, Germany

5.1.6 Devices and instruments

Table 11: Devices and instruments

Device/instrument	Supplier/manufacturer
Arpege 170 N_2 Tank	VWR, Darmstadt, Germany
Artiste linear accelerator	Siemens Meidcal Solutions, CA , USA
Balance BL3100	Sartorius, Göttingen, Germany
Centrifuge 5810R	Eppendorf, Hamburg, Germany
DiATOME diamond knife (3.5mm length, 45° angle)	DiATOME AG, Biel, Switzerland
Dissection tools (scissors, scalpel, foreceps)	C. Bruno Bayha GmbH, Tuttlingen, Germany
Freezer (-80°C)	Thermo Fisher, Waltham , MA, USA

Device/instrument	Supplier/manufacturer
Freezer (-20°C)	Bosch, Gerlingen, Germany
Fridge (4ºC)	Bosch, Gerlingen, Germany
Grid filming apparatus	Bespoke design by University of Saarland
Heating chamber	Binder, Tuttlingen, Germany
HERAsafe™ biological safety cabinet	Thermo Fisher, Waltham , MA, USA
Ice machine	Scotsman, Illinois, USA
pH meter pH526	WTW, Weilheim, Germany
Pipetus ® akku	Hirschmann Laboratories, Eberstadt, Germany
Pipettes (P10, P200, P1000)	Eppendorf, Hamburg, Germany
Plexiglass cylinder	Bespoke design by University of Saarland
Plexiglass plate	Bespoke design by University of Saarland
Precision balance	Sartorius, Göttingen, Germany
LightCycler®	Roche, Basel, Switzerland
Manual microtome RM2235	Leica, Wetzlar, Germany
Microcentrifuge Heraeus Biofuge fresco	Heraeus, Hanau, Germany
Micropipettes (P10, P200, P1000)	Gilson Inc., Middelton, WI, USA
Microwave	Panasonic, Osaka, Japan
Multichannel pipette S-12	Brand, Wertheim, Germany
Nanodrop 2000c	Thermo Fisher, Waltham , MA, USA
Neubauer Counting Chamber	Marienfeld, Lauda-Königshofen, Germany
Nikon Eclipse TS100 light microscope	Nikon Instruments Europe BV, Amsterdam, The Netherlands
Nikon Eclipse NI-E microscope	Nikon Instruments Europe BV, Amsterdam, The Netherlands
Shaker S4	ELMI Ltd., Riga, Latvia
Shandon Exclesior ES tissue processor	Thermo Fisher, Waltham , MA, USA
Stuart® hotplate stirrer	Biocote, Coventry, UK

Device/instrument	Supplier/manufacturer
Tecnai Brown Transmission Electron microscope	FEI, Oregon, USA
Thermoshaker HLC MHR23	Ditabis, Pforzheim, Germany
Tissue-tek TEC 5 embedding station	Sakura, Alphen aan den Rijn, Netherlands
Ultramicrotome Ultracut S	Leica, Wetzlar, Germany
VI05 250i CO_2 incubator	Heraeus, Hanau, Germany
Vortexgenie 2	Scientific Industries, Bohemia, NY, USA
Waterbath	GFL, Burgwedel, Germany

Table 12: Image and data analysis software

Software	Creator/distributor
Analysis TEM image acquisition software	FEI, Oregon, USA
GraphPad	GraphPad Software, San Diego, CA, USA
Microsoft Office	Microsoft Corporation, Redmond, WA, USA
NIS Elements Basic Research	Nikon Instruments Europe BV, Amsterdam, The Netherlands
Origin 2015G 64bit	OriginLab Corporation, Northampton, MA, USA
Photoshop CS3	Adobe, San Jose, CA, USA

5.2 Methods

The following sections cover all methods used in the acquisition of data for this project.

5.2.1 Cell culture

All *in vitro* experiments were completed using the following lung fibroblast cell lines: WI-38, *WI-38hTERT/ptet-on-sh-NoTarget* (NT) and *WI-38hTERT/ptet-on-sh3-H2AFJ* (KD). These cell lines were kindly supplied by Prof. Dr. Carl Mann and produced as per established protocol by Contrepois et al (Contrepois et al., 2017). General culture methods described below were equal for all cell lines and completed under sterile conditions. Cell lines were received in frozen vials containing approximately 3-5 million cells in DMSO freezing medium. To take cells into culture, the contents of the vials were quickly defrosted at 37ºC and transferred to 15ml tube. To prevent possible deleterious osmotic effects associated with rapid dilution of DMSO freezing medium, the complete growth medium at 37ºC was added dropwise over several minutes. Following 4min. centrifugation at 500g, supernatant was removed and cell pellet resuspended in 10ml growth medium. Cell suspension was then transferred to T75 culture flask and cells were grown at 37ºC, 5% CO_2, 5% O_2. Once confluency was reached, cells were split 1:1 into new T75 flasks. This was achieved by removing medium, washing cells 1x in PBS and incubating in 3ml Trypsin for 2min at 37ºC. 10ml of 37ºC medium was added to neutralize Trypsin and cell suspension transferred into 15ml tube which was centrifuged at 500g for 4min. Supernatant was removed, cells resuspended in fresh medium and divided amongst flasks containing additional fresh medium.

5.2.1.1 Induction of insert expression

In the case of WI-38-NT and –KD, expression of red fluorescent protein, KD and NT cassettes, respectively was achieved by the addition of 1µg/ml of doxycycline to growth medium 1 week prior to irradiation, ETO exposure or control acquisition. Doxycycline treatment was continued following IR until cells were harvested.

5.2.1.2 Cell monolayers

Once cells had reached 90% confluency, adherent cells were detached by first removing excess medium with 2x PBS washes followed by a 2min. incubation with 1xTrypsin at 37ºC. Cell suspension was then diluted with 10ml growth medium and centrifuged at 500g for 4min. Supernatant was removed and cells re-suspended in fresh growth medium. 6-well plates were prepared by placing two circular glass coverslips into each well. Using Cell-saver tips, 150µl of cell suspension was gently dispensed onto each coverslip taking care to maintain

the surface tension. Cells were left to settle and adhere for 30min, after which 3ml of growth medium was added to each well and cells incubated as above. Experiments were carried out once 90% confluency was reached.

5.2.2 Monolayer irradiation

Irradiation with varying doses (low-LET, 6-MV photons, 2Gy/min) was performed at the Department of Radiation Oncology, Saarland University (Homburg/Saar, Germany) using Artiste™ (Siemens, Munich, Germany) linear accelerator. The radiation plan was calculated using Pinnacle planning software in which the position of the coverslips, the height of the 6-well plates and the placement of a 1cm thick Plexiglas plate on top of the 6- well plate, was taken into consideration to ensure optimum doses delivery to the cell monolayer. For RT-qPCR and Western blot cells were directly irradiated in T75 flasks on top of two 1cm Plexiglas plates (Figure 6). Cells were placed back into incubator and fixed/harvested once the desired time point after radiation had been reached as per protocol specific method below.

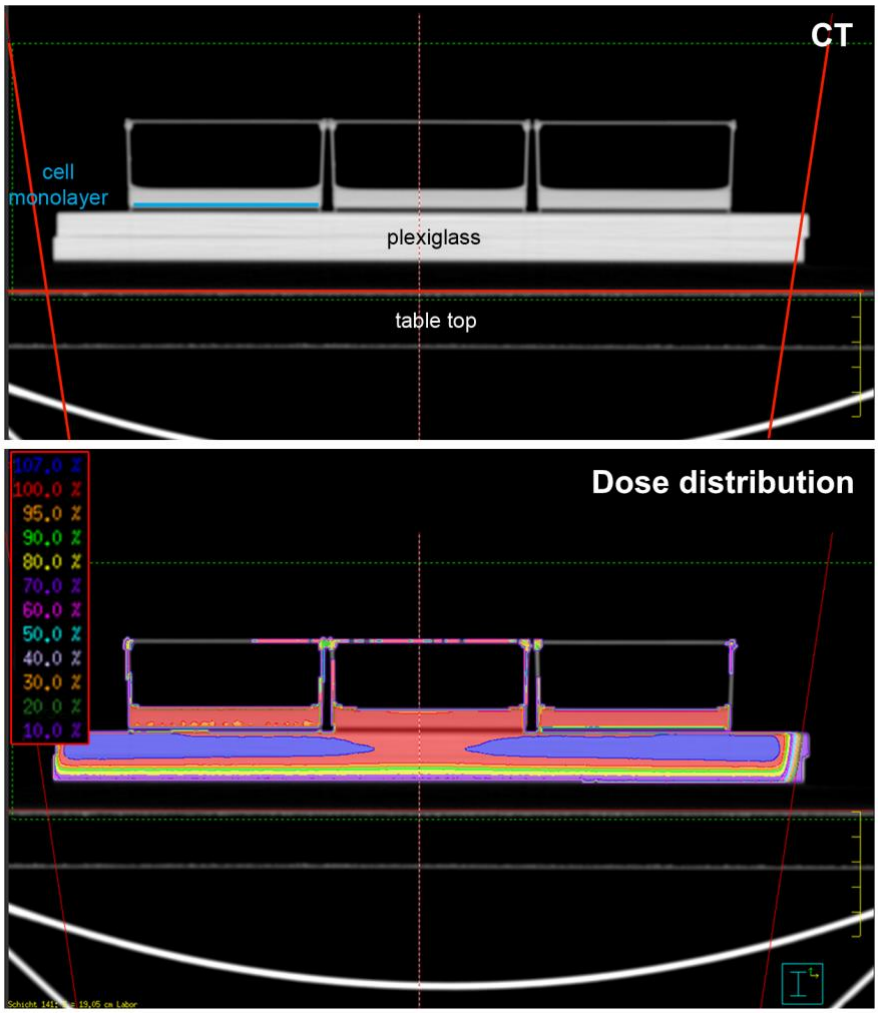

Figure 6. Dose distribution calculated using Pinnacle software.
Example of Pinnacle interface where CT images were used to calculate dose distribution for cell irradiation in T75 flasks.

5.2.3 Etoposide exposure

Etoposide is an anti-cancer drug that targets DNA Topoisomerase II (Topo II), a DNA replication enzyme, which aids the unwinding and recoiling of the DNA double-helix through temporary, deliberate DSBs. (Montecucco et al., 2015). ETO forms a complex with TopoII and DNA and thus causes deleterious DNA DSBs by preventing the re-ligation of DNA strands as intended (Pommier et al., 2010). ETO solution was added to growth medium in a final concentration of 20µM. When samples were exposed for the desired time (24h, 1w, 2w) medium was removed and samples fixated as per protocol specific method below (5.2.4.1).

5.2.4 Immunofluorescence microscopy (IFM)

Visualization, localization and quantification of proteins of interest was achieved through indirect immunofluorescent labelling of fixated cells viewed under a fluorescence microscope which was fitted with a high-intensity mercury arc lamp for illumination and wavelength filters allowing for specific excitation of fluorophores coupled to secondary antibodies.

5.2.4.1 Sample fixation

When the specific time point after IR or of continuous ETO exposure was reached, the medium was removed from 6-well plates and the circular coverslips bearing cell monolayers were gently rinsed twice with PBS. Remaining PBS was removed and replaced by PFA fixation solution for 5 min. Samples were rinsed with PBS and stored in sodium azide solution at 4°C for a maximum of 4 weeks.

5.2.4.2 IFM Staining

Samples stored in sodium azide required an additional wash step of three 10min washes with PBS to remove excess storage solution. Fresh samples could proceed directly to the permeabilisation step which encompassed a 5min incubation period with 0.5% Triton-X-100 under slight rocking to ensure even distribution and permeabilisation. This was followed by a 10min wash with wash solution containing 0.1% Tween. At this stage samples were blocked with blocking solution for 1h at RT prior to being incubated with primary antibody overnight at 4°C. Excess antibody was then removed through 3x 10min washes and the secondary antibody added on top of coverslips for 1h at RT. This was subsequently followed by three additional 10min washes with wash solution. In case of a double stain, the protocol above for primary and secondary incubation was repeated however the primary antibody was incubated either 37°C or RT for only 1h. The temperature at which antibody was

incubated was previously optimized and adjusted accordingly for each antibody used. The final step was to rinse the samples with PBS for 5min and mount in hard set mounting medium containing DAPI to stain the DNA allowing the identification of cell nuclei.

5.2.4.3 Data acquisition through light microscopy

For the dose response curve (non-IR control, 0.1Gy, 1Gy, 2Gy, 10Gy; 24 h post-IR) of H2A.J, cells were counted until a minimum of 50 H2A.J positive cells were obtained. For the 2Gy kinetic, 20Gy kinetic (non-IR control, 0.5h, 5h, 24h, and 48h post-IR) and long term accumulation (1w and 2w post-IR) of H2A.J and 53BP1 was quantified by counting a minimum of 200 cells per condition and noting H2A.J positivity, as well as, 53BP1 foci/cell and H2A.J/53BP1 double-positivity. Three technical replicates were completed for each condition and cell line.

5.2.5 Senescence-associated beta galactosidase (SA-β-gal)

It has been shown that senescent cells show a distinct β-galactosidase activity which can be measured at pH6 and thus distinguishes it from acidic β-galactosidase activity found in all cells at pH4. This senescence-associated β-galactosidase (SA-β-gal) activity is due to an increase in the presence of the lysosomal enzyme itself and has become a widely accepted marker for senescent cells.

5.2.5.1 Sample fixation and staining

Cells were prepared in monolayers as described above and staining commenced following either IR or ETO exposure, as well as, in non-irradiated/non-exposed controls. Medium was removed from the samples and all remaining traces removed by gently washing twice with PBS. Cells were then fixed for 5min using SA-β-gal fixation solution. Once cells were fixed and washed 2x 10min with PBS, SA-β-gal staining solution was added and incubated overnight, taking care to avoid exposure to light. Staining solution was removed, samples washed twice for 10min with PBS, and incubated with methanol for 30sec. Cover slips were then placed at an angle against the well walls and left to dry. Permeabilisation of cells was achieved through a 5min incubation with permeabilisation solution. Following two 10min washes with BSA wash solution, the samples were blocked with BSA blocking solution for 1h at RT. Samples were then transferred to a humidity chamber and incubated with anti-H2A.J antibody in BSA blocking solution overnight at 4^{o}C. The following day, the samples were washed twice for 10min with BSA wash solution and subsequently incubated with an immunoglobulins/biotinylated secondary antibody suspended in BSA blocking solution for 1h

at RT. After a further two 10min washes with PBS only, the samples were incubated with ABC complex (Prepared as per manufacturer's instructions) for 30min at RT in the humidity chamber. Any remaining ABC complex was thoroughly rinsed off using a further three 10min PBS washes, after which the DAB agents (Prepared as per manufacturer's instructions) were added on top of the samples for 30min at RT. The samples then underwent two quick 5min washes with PBS after which excess liquid was removed using tissue paper and finally mounted on glass slides using aqueous mounting medium.

5.2.5.2 Data acquisition through light microscopy

Using a light microscope, 200 cells were quantified for each condition where H2A.J- and SA-β-gal positivity was noted for each marker. Three technical replicates were completed for each condition and cell line.

5.2.6 BrdU labelling

To test the stability of senescence-associated growth arrest, as well as, the stability of the DNA-SCARS, cells were labelled with *Bromodeoxyuridine* (5-bromo-2'-deoxyuridine/BrdU), a thymidine analog incorporated into DNA during DNA synthesis. Proliferating non-irradiated cells served as control group to senescent cells (20Gy; 2w). Cells were pulsed with 10µmol/L BrdU in culture medium for 24h prior to fixation. Removal of medium was followed by two quick 5sec washes and three 2min washes with PBS. Fixation and permeabilisation followed as per section 5.2.4.1, followed by 3x 5min PBS washes and one dH_2O rinse. DNA denaturation was completed through a 1h incubation in 2M HCl at RT succeeded by 3x 5min PBS washes and 2h RT incubation with primary anti-BrdU antibody in 0.1% Tween,1 % BSA in PBS. After 3x 5min washes of Tween/BSA/PBS, samples were incubated with fluorescence-coupled anti-rat secondary antibody in Tween/BSA/PBS for 2h at RT. 3x 5min washes with PBS preceded coverslip mounting with hard-set mounting medium containing DAPI.

5.2.7 Proximity ligation assay

Duolink® Proximity ligation assay (PLA) system was used detect co-localizations of H2A.J and 53BP1. This system detects co-localizations between molecules that lie a maximum distance of 40nm apart. Once primary antibodies of desired targets have bound, samples are incubated with specific secondary antibodies coupled with oligonucleotides (PLA probes). If proteins are close enough together hybridizing connector oligos join the PLA

probes and a closed circle DNA template is formed with ligase. The PLA probe acts as a primer for DNA polymerase and the circle DNA as a template for rolling-circle amplification. Concatemeric sequences are generated which remain tethered to the PLA probes resulting in an amplified signal which allows for localization due to its tethering. Complementary detection oligos coupled to fluorochromes then hybridize to complementary sequences within the amplicon resulting in discrete spots detectable through IFM. Samples were prepared and fixed as for standard IFM. PLA foci for 50 cells were quantified. Three technical replicates were completed for each condition and cell line.

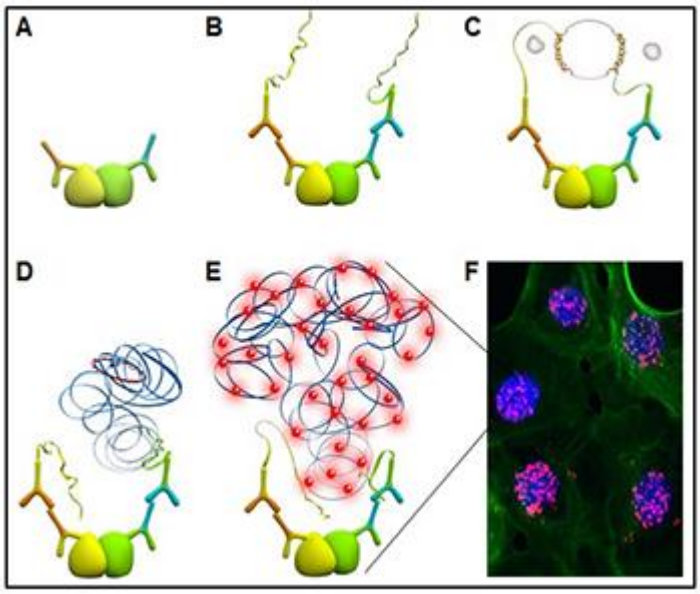

Figure 7. Schematic representation of proximity ligation assay mode of action.
Taken from www.sigmaaldrich.com.

5.2.8 Transmission Electron Microscopy

Please note all credit for sectioning, staining and TEM data acquisition of monolayer cells belongs to Dr. rer. med. Yvonne Lorat who kindly granted permission for use of raw data and images.

5.2.8.1 Monolayer fixation and embedding

Cells were prepared as described as above per section 5.2.1 and 5.2.2. Cells were gently washed once with PBS and fixed by means of a 2h incubation period with TEM fixation solution. Three 10min washes with PBS were succeeded by dehydration of the samples, achieved through 5min immersions in increasing concentrations of alcohol (30%, 50%, 70%, 95%, 100%, and 100%) at RT. A fresh 6-well plate was then lined with Parafilm® to avoid adhesion of glass to the well floor and coverslips were transferred across and incubated in 1:2 EtOH: LR white solution for 30min at RT. This was followed by two consecutive 1h

incubations in pure LR white at RT with subsequent overnight immersion in LR white at 4°C. LR white was again refreshed the next day and a further 1h immersion completed. Meanwhile, a 50ml tube of LR white was placed at 50°C without the lid to allow for the evaporation of any gases/bubbles from the resin. Next, the gelatin capsules to hold the samples were prepared by placing a small drop of LR white accelerator onto a glass slide and placing the opening of the capsule face down into the accelerator for 1h which allowed the accelerator to move up the inside of the capsule through capillary action. Once completed, the capsule was filled with the previously de-gassed LR white at 50°C, simultaneously mixing with the accelerator in the process. Coverslips were set onto the rim of the capsules with the cell monolayer touching the resin. With the coverslip held in place, the entire construct was inverted and placed onto a layer of Parafilm®. These were then incubated at 50°C for 24h to allow the LR white resin to set. Samples were left to cool once removed from incubator. At this stage the cell monolayer was infiltrated with resin and had bonded with the resin in the capsules. The coverslips were removed from the capsules by placing constructs in -80°C for 10min and when removed, the capsules were quickly snapped off, thereby leaving the cell monolayer patched onto the bottom of the resin in the capsule.

5.2.8.2 Filming of nickel grids

The first step in this process was to create a pioloform film which would later be used to coat the nickel grids. A bespoke cylinder was placed on top of a conical flask and filled with chloroform which was left to sit for 30sec. The chloroform was then drained and decanted into its original container. Next, the cylinder was filled with pioloform and the sides of the cylinder tapped to remove any air bubbles which may disrupt the formation of the film. A glass slide, which was previously been cleaned to remove any dirt and lipids, was then placed into the pioloform for 1min. The pioloform was then allowed to slowly drain off, the slide was removed and set in a coverslide holder to dry. A glass bowl was filled with distilled water to the rim and any dust or lint removed from the water's surface with a glass wand. This was completed under a plastic hood to avoid any further particles contaminating the surface. The coated slides were then dipped into the water, the edges of the pioloform film scored with a razor blade and the slide slowly lowered into the water at a slight angle allowing the film to detach from the slide and glide onto the water surface. Using a set of tweezers, nickel grids were placed onto the film with the matt side down. The grid-covered film was removed by placing the backing paper of a section of Parafilm® on top and then lifting both out and simultaneously inverting both so that the grid and film lay on top of the backing paper. These were placed in a petri dish, covered and allowed to dry. When needed individual coated grids could then be lifted off using ultra fine forceps.

5.2.8.3 Ultrathin sample sectioning

The gelatin capsule was firstly secure in the sample holder of the ultra-microtome. Using the light microscope and a razorblade, 1mm of the gelatin capsule was removed from the outside of the embedded sample to allow better access to the monolayer of cells located at the very end of the resin tube. The sample was then placed in the horizontal arm of the microtome at a minimal angle to the diamond knife. This was to ensure that only a small section of the monolayer was removed when cutting and not the entire face of the sample. Sections with a thickness of approximately 85nm were sliced off the sample and floated on water as they left the diamond blade. Sections of optimum thickness were then fished from the water's surface with pioloform coated grids ensuring they were placed on the center of the pioloform film while doing so. The grid was touched to filter paper to remove any excess water and placed in a grid box. Suitability of the sections for TEM analysis could be determined by their color as 50-90nm thick sections are silver to light gold in color and are clearly distinguishable. To check whether cells were present in the sections one such section was lifted off the surface using a wire loop and placed onto a glass slide. This was placed onto a hot plate at 50^{o}C and once excess water had evaporated, was stained with Richardson's stain for 30sec. Excess stain was rinsed off with dH_2O and slide once again dried on hot plate. Any cells present showed a monochromatic stain and could be identified under a light microscope.

5.2.8.4 Immunogold protein labelling

This labelling technique is based on the same indirect labelling technique used in immunofluorescence however in this instance the secondary antibodies are coupled with gold beads of various sizes instead of fluorescing particles. The high electron density of the gold beads causes greater electron scatter which, when visualized, can be seen as very dense, dark spots. All labelling steps were performed in a humidity chamber in which 30µl of each solution was spotted onto a taut section of Parafilm®. Grids were always placed face down on top of each solution droplet where they floated for the duration of the incubation. Firstly, the samples were blocked through a 20min incubation with BSA-c™ solution followed by 2x 5min wash steps in incubation buffer. Primary antibodies were diluted in incubation buffer and sample incubation ensued overnight at 4^{o}C. Following 6x 5min washes, secondary antibody incubation commenced for a duration of 1.5h at RT with 6nm or 10nm gold particle-conjugated secondary antibodies. 6x 5min washes with incubation buffer were then succeeded by 3x 5min washes in PBS. Labelling process was concluded with post fixation achieved through a 30min incubation with 2% glutaraldehyde in PBS, followed by 3x 5min washes in dH_2O.

5.2.8.5 Contrasting ultra-thin sections

The contrast achieved in the electron microscope depends on the electron density of the samples and as biological samples are mainly composed of low electron density elements (C, O, N) they require additional staining to increase the contrast. This is usually achieved through the use of heavy metals, in this case, uranyl acetate in which uranyl ions preferentially bind to the nucleic acid phosphate groups of DNA, as well as, to proteins and lipids with sialic acid carboxyl groups (Erenpreisa, 1981). The immunogold-labelled grids were incubated for 5min on a 30µl uranyl acetate droplet and then in dH_2O for 5min. Excess liquid was removed by touching grid to filter paper and returning to grid box to dry completely before visualization in transmission electron microscope.

5.2.8.6 TEM analysis of immunogold-labelled proteins

A Tecnai Biotwin™ transmission electron microscope (FEI, Eindhoven, Netherlands) was employed for visual analysis. For quantification, single beads and bead clusters were counted in 25 random nuclear sections. Additionally, chromatin localization (hetero-/euchromatin) was also noted. Hetero- and euchromatin was defined through varying gray scale presented by each chromatin state.

5.2.9 ELISA

To detect the SASP of cells, a multi-analyte ELISA was performed on conditioned medium. A custom Multi-Analyte ELISArray™ Kit was commissioned to detect IL1β, IL6, IL8, IL12, IFNγ, TNFα, Gm-csf, MIP-1α, MCP1, TGFβ1, IP10 and GRoα respectively. Conditioned medium was prepared as per protocol described by F. Rodier (Rodier, 2013) as follows: For each condition (non-IR, 20Gy; 2 weeks) and cell line (NT, KD) to be examined 750,000 cells were seeded in a T75 culture flask and grown to 90% confluency. 20Gy irradiated samples were cultured for 2w after IR exposure and 24h before the 2 week time point was reached, growth medium was removed, cells washed 3x with warm PBS and 6ml FBS-free medium was added. This change in medium was also implemented for non-irradiated cells once they had reached 90% confluency. Following the 24h culture with serum-free medium, the conditioned medium was removed and transferred to a 15ml tube and kept on ice. Cells were trypsinated (see section 5.2.1) and counted so conditioned medium concentration could be adjusted to cells/ml and all samples would be run at equal concentration. Conditioned medium was then centrifuged at 300g for 5min to remove any cell debris, supernatant removed and filtered through a 0.45µm syringe filter. Conditioned medium was aliquoted and frozen at -80^{o}C until SASP could be measured. ELISA was run as per manufacturer's

instructions. The concentration of all samples was adjusted to that of the sample with the lowest concentration ($3.23x10^5$ cells/ml). Preliminary results showed that the concentration of MCP1 in NT 20Gy;2w post-IR sample was above the linear range of the assay and therefore was diluted 40-fold to 10,000 cells/ml resulting in an absorbance reading within the linear assay range. A minimum of two technical replicates was performed for each sample and each analyte.

5.2.10 Reverse transcription quantitative PCR (RT-qPCR)

For RT-qPCR, NT and KD were cultured as described in sections 5.2.1 and 5.2.1.1 in T75 culture flasks. Once cells had reached 90% confluency they were either irradiated (20Gy;2w) or used as non-irradiated controls.

5.2.10.1 RNA extraction

Once desired time point/condition was reached, growth medium was removed, cells were trypsinated and centrifuged at 500g for 4min. Supernatant was removed and pellet resuspended in 1.5ml Trizol™ and the lysate pipetted up and down several times to homogenize. A 5min incubation was undergone to allow complete dissociation of the nucleoproteins complex after which 0.3 ml chloroform was added and incubated for 2-3min. Samples were centrifuged for 15min at 12,000g at 4°C, which resulted in separation of the mixture into three phases. The colorless aqueous uppermost phase contained the RNA and was thus removed and transferred to a fresh tube, taking extreme care to avoid transferring any of the interphase or organic layer. Next, 0.75ml of isopropanol was added to the aqueous phase and incubated for 10min followed by 10min centrifugation at 12,000g at 4°C. Supernatant was removed and the white gel-like pellet containing the total RNA precipitate was resuspended in 1.5 ml 75% ethanol. Sample was vortexed briefly and centrifuged for 5min at 7,500g at 4°C. Supernatant was discarded and pellet allowed to air dry for 5min. Subsequently, pellet was resuspended in 50µl RNase-free water and incubated at 60°C for 15min. RNA concentration and purity was assessed using NanoDrop™ spectrophotometer. An A260/A280nm ratio of ~2 was considered pure.

5.2.10.2 Complementary DNA (cDNA) synthesis

As a real-time two-step RT-qPCR method was used, the RNA was first transcribed into *complimentary DNA* (cDNA) using the QuantiTect® Reverse Transcription kit as per manufacturer's instructions. This allowed for cDNA synthesis with integral removal of genomic DNA contamination. A blank reaction was also completed simultaneously to ensure

no contamination was present in the kit itself. DNA concentration and purity was assessed using NanoDrop™ spectrophotometer. An A260/A280nm ratio of ~1.8 was considered pure.

5.2.10.3 Quantitative two-step RT-PCR

The PCR reaction mixture was set up as per manufacturer's instructions of the QuantiTect® SYBR® Green PCR kit, adding everything but the cDNA. 18µl of master mix was pipetted into a 96-well plate followed by 2µl of diluted cDNA to complete the reaction mixture. The plate was covered with optical adhesive film, vortexed briefly to ensure thorough mixing and centrifuged for 1min to provide a bubble-free solution. The plate was placed into the real-time PCR instrument and run under the program detailed in Table 14.

Table 13: PCR reaction setup

Component	Volume/reaction
QuantiTect® Master Mix	10µl
Primer A	1µl (final conc. 0.5µM)
Primer B	1µl (final conc. 0.5µM)
RNase-free water	Variable
cDNA	Variable (1µg/reaction)
Total reaction volume	20µl

Table 14: Real-Time PCR instrument run settings

Step	Target Temp (ºC)	Incubation time	Temp. transition rate (ºC/s)	Secondary target temp. (ºC)	Step size (ºC)	Step delay (cycles)	Acquisition mode
Denaturation	94	15min	20	0	0.0	0	NONE
Amplification	94 Variable* 72	15 sec 30 sec 45 sec	20 20 20	0 0 0	0.0 0.0 0.0	0 0 0	NONE NONE SINGLE
Melting curve	80 40 95	0 15 sec 0	20 20 0,3	0 0 0	0.0 0.0 0.0	0 0 0	NONE NONE STEP and HOLD
Cooling	40	10 sec	20	0	0.0	0	NONE
Analysis mode: **Quantification**							
Cycles: **40**							

* See Table 9 for annealing temp. of individual primers

5.2.10.4 Data analysis

Fold change in gene expression was calculated using the Delta-Delta Ct Method ($2^{-\Delta\Delta Ct}$) (Livak, Schmittgen, 2001) with GAPDH as the housekeeping gene and non-irradiated NT samples as control.

5.2.11 Murine epidermis

Please note all credit for fractionated irradiation, sample collection and sample embedding of murine tissue belongs to Zoé Schmal who undertook these experiments as part of her doctoral thesis. The thesis of Ms. Schmal focused solely on the hippocampus of these mice, however, to avoid unneccessary sacrifice of mice, all organs were collected for potential future studies. The skin samples which were acquired at this time point were examined in this study. Studies were approved by Medical Sciences Animal Care and Use Committee of Saarland University (approval under application number: 05/2014 and 35/2016).

5.2.11.1 Sample acquisition

C57BL/6 strain (C57BL/6NCrl) mice were obtained from Charles River Laboratories, Sulzfeld, Germany. All mice were housed in groups of 3 to 6 animals in IVC cages under standard laboratory conditions (22°C ±2, 55% ±10 humidity, 12h : 12h light/dark cycle, ad libitum feeding conditions). Fractionated irradiation began when mice reached maturity at 8 weeks old. Mice were placed in bespoke Plexiglas cylinder and covered by a 1.5cm thick tissue-equivalent plastic material which improved dose homogeneity. To execute a whole body radiation, the cylinder was then placed under the linear accelerator and the following conditions applied: radiation field size: 30cm × 30cm; collimator angle 0°; gantry angle 0°; source surface distance (SSD): 208cm (0.1Gy); beam energy: 6-MV photons; dose-rate: 2Gy/min. Tomography-based, three-dimensional dose calculations were performed using Pinnacle™ planning system and a thermoluminescent dosimeter was employed to confirm a reliable and uniform dose delivery. Mice were exposed to 0.1Gy every 24h from Monday to Friday over the course of 4 weeks. 72h after the final dose was applied, mice were anesthetized intraperitoneally, and a section of dorsal skin removed, rolled into a tight coil to increase surface area, as well as, improve ease of handling, and placed in 4% PFA overnight at RT. Subsequently, mice underwent perfusion which resulted in termination and allowed for the collection of the remaining organs for further studies. Once samples were fixed, they were transferred into tissue processing embedding cassettes and rinsed in H_2O. Cassettes were then placed in automatic tissue embedder programmed to run overnight. Briefly, as paraffin is hydrophobic, tissues were firstly dehydrated through a number of incubations in ethanol (70%, 80%, 90%, 95%, absolute, absolute for 65min each) followed by three incubations in Xylol (55min x2, 80min) in which the Xylol displaced the ethanol and also removed fat which acts as a barrier to paraffin infiltration. Samples were then infiltrated with melted paraffin through a 1h incubation at 58°C. Cassettes were now transferred to an embedding station where they were placed in fresh liquid paraffin. A metal mold was then placed onto a heat plate and a small drop of wax added. The cassette was opened, the lid removed and the sample placed into the mold ensuring correct orientation of sample to

achieve desired “plane of section”. The sample was held in place and the mold moved onto a cooling plate (-4°C) causing the wax to set and the sample to remain fixed. The cassette was placed on top of the mold, lifted off the cooling block and filled to the brim with liquid paraffin and left to solidify on cooling plate. Once completely cooled, the mold was removed and the resulting cassette with protruding sample-containing paraffin block was complete.

5.2.11.2 IFM staining

Firstly, tissue sectioning was required. Tissue cassettes were placed at -20°C for approx. 2h prior to sectioning. Cassettes were fixed in the microtome and 4µm thick sections removed from the front of each sample. As the blade sliced the sample, the sections were floated on top of the water held in the bath adjacent to the blade. Using a glass slide, one section at a time was fished out. With the glass slide held at an angle, the section was floated on top of H_2O at 56°C causing the paraffin to soften and allowing the section to be pulled flat and fixed onto the glass slide. Samples were then de-paraffinated by 3x 7min immersions in Xylol. Re-hydration of tissue was achieved by passing through an alcohol row of decreasing concentration for 3min in each (absolute, 96%, 90%, 80%, 70%) ending in dH_2O. The cross-links formed during fixation may mask the antigenic sites in a sample therefore they were broken through a 60min incubation in antigen retrieval buffer in a water bath at 95°C. The dish containing slides and antigen retrieval buffer, was removed from the water bath and left to cool for 20min. To reduce background or unspecific staining, samples were blocked with Immunoblock for 1h at RT. This was done by taking the slides out of the cooled citrate buffer, tapping off excess liquid onto lint-free paper and pipetting 100µl blocking solution onto slide. A coverslide was gently placed over the liquid ensuring no air bubbles formed and the entire sample was covered. Slides were then placed in a humidity chamber. All subsequent incubations for antibodies as well as DAPI staining were completed in this manner also. Following blocking, samples were incubated overnight at 4°C with primary antibody in Immunoblock. Coverslide was removed by quickly flicking it off and the slide was placed in a slide rack and immersed in PBS in a glass staining dish. Slides were washed on a magnetic stirrer for 3x 10min followed by 1h RT incubation with fluorescent-coupled secondary antibody in the dark. Excess secondary antibody was removed through further 3x 10min washes in the dark. If a double stain was required, primary and secondary antibody incubation, and wash steps were repeated as above ensuring a different species was used for the second primary antibody. Coverslip was then mounted on top of samples using hard-set mounting medium containing DAPI. Samples were left at 4°C overnight to allow complete setting of mounting medium.

5.2.11.3 Data acquisition

For the quantification of H2A.J positive cells in the murine epidermis, 500 cells were counted per tissue section noting the H2A.J-positivity of each. This was completed for three biological replicates as well as three technical replicates. Each irradiated sample was compared to a non-irradiated, age-matched control.

5.2.12 Human epidermis

Please note that the credit for obtaining the skin samples for the following experiments belongs to Dr.rer.med. Caroline Bäumert. The irradiation and embedding of ex-vivo irradiated series was completed in collaboration whereas the aged human skin samples were gathered and processed by Dr. Bäumert alone. Protocol procedures were approved by the local ethics committee ("Ethikkommission der Ärztekammer des Saarlandes", ethical approval application number: 226/16) and all donors provided written, informed consent.

5.2.12.1 Collection of human skin biopsies

Following signed patient consent, skin samples with a minimum surface area of 25mm^2 were removed from abdominal area of patients of varying ages during elective surgery. Exclusion criteria included systemic illnesses, rheumatism, autoimmune diseases, and Grade 5 renal failure (determined by Chronic Kidney Disease Epidemiology Collaboration equation). Samples should originate from the abdominal area due to low sun exposure associated with this location. Samples were placed in 15ml tube containing 37^{o}C RPMI medium as soon as they were removed from patient and transported back to the laboratory in an insulated box containing heat pads. To avoid incomplete fixation of samples, any subcutaneous fat was removed from samples and fixation occurred through a 24h incubation in 4% PFA solution at RT. All steps following fixation were completed as described for murine skin above.

5.2.12.2 Ex-vivo irradiation of human skin biopsies

Once skin sample was received it was sectioned into 8 pieces and divided amongst two 6-well plates containing medium. One 6-well plate was irradiated with 10Gy, the other, sham irradiated to act as a non-irradiated control. Samples were fixated 0.5h, 5h, 24h and 48h after irradiation along with a non-irradiated control for each time point.

5.2.12.3 IFM staining

IFM staining was completed as described in 5.2.11.2 for murine epidermis.

5.2.12.4 Data acquisition

When examining aged human skin, three biological replicates were examined from each age group; 20-30 years old, 31-60 years old and >60 years old. Two technical replicates were performed for each sample. As age-associated foci are not as abundant as IR-induced foci and widely scattered, quantification continued until at least 30 foci-positive cells or 1000 cells in total were captured. H2A.J positivity and H2A.J/53BP1 positivity was noted for all captured cells, as well as, foci numbers/cell. Ex-vivo irradiated samples and their non-irradiated controls were taken from one patient. Three technical replicates were performed for each non-irradiated control and time point post-IR (non-IR; 0.5h, 5h, 24h, 48h. 10Gy IR; 0.5h, 5h, 24h, 48h post-IR). As IR-induced 53BP1 foci are much more numerable and frequent than age-associated 53BP1 foci, quantification continued until at least 30 foci-positive cells and 250 cells in total were captured. H2A.J positivity and H2A.J/53BP1 positivity was noted for all captured cells as well as foci numbers/cell.

5.3 Statistical analysis

Statistical analysis was performed using GraphPad and Origin 2015G 64bit Software. Data sets were analysed for normal distribution using Shapiro-Wilk. Normally distributed data sets were subsequently analysed using unpaired two-tailed Student's t-test (equal variances under F-test), Welch's t-test (unequal variances under F-test) or ANOVA. Non-parametric data was analysed for statistical significance using two-tailed Mann-Whitney U test. Normally distributed data was displayed as Mean plus standard error whereas non-parametric data was displayed as box-plot containing Median with upper and lower Quartiles were applicable. A $p<0.05$ was considered statistically significant, $p<0.01$ as highly significant and $p<0.001$ as extremely statistically significant.

6 Results

6.1 H2A.J accumulates following 2Gy irradiation

To gain insight into H2A.J accumulation following a therapeutic dose fraction, *WI-38* (WT) and NT fibroblasts were irradiated with 2Gy, fixed at various time points following IR, in which active DNA damage repair is ongoing, and stained for IFM. Samples were labelled with H2A.J, whose accumulation could be monitored in context of DNA-damage repair through a double stain with 53BP1 (Figure 8A). Quantification of 53BP1 foci revealed, that both WT and NT fibroblasts, displayed typical DNA damage repair kinetics in which the highest foci numbers were observed shortly after irradiation (0.5h; WT: ~25 ±1.1 foci/cell, NT: ~23 ±0.7 foci/cell) and continuously declined thereafter until 48h post-IR (48h; WT: ~3 ±0.3 foci/cell, NT: ~2 ±0.04 foci/cell) (Figure 8B). In comparison, H2A.J displayed a delayed accumulation in response to DNA damage (Figure 8C). For both WT and NT fibroblasts, significantly increased numbers of H2A.J positive cells were noted for almost all time points after IR (except WT; 0.5h) compared to the non-irradiated controls (non-IR; WT:12.4 ±1.2%, NT:10.5 ±1.2%). In contrast to 53BP1 foci however, H2A.J positive cells initially increased following IR reaching a maximum 24h post-IR (24h; WT: 26.6 ±0.3%, NT: 26.9 ±1.6%) after which numbers began to decline (48h; WT: 21.6 ±1.8%, NT: 21.2 ±1.3%). Although 53BP1 demonstrated minor but statistically significant differences between cell lines 24h and 48h following IR (24h; WT ~4 ±0.2 foci/cell, NT ~3 ±0.2 foci/cell, 48h; WT ~3 ±0.3 foci/cell, NT ~2 ± 0.04 foci/cell) this disparity in DNA-damage levels did not affect the levels of H2A.J positive cells, with both WT and NT fibroblasts showing comparable accumulation patterns following a single dose of 2Gy irradiation. Additionally, both WT and NT cells were used in this experiment to compare the repair capacity and H2A.J accumulation patterns in wild type WI-38 to genetically modified WI-38-NT. Thus it was ensured that the „No-Target“ insert did not affect the cells negatively and going forward WI-38-NT cells could be used in all subsequent experiments.

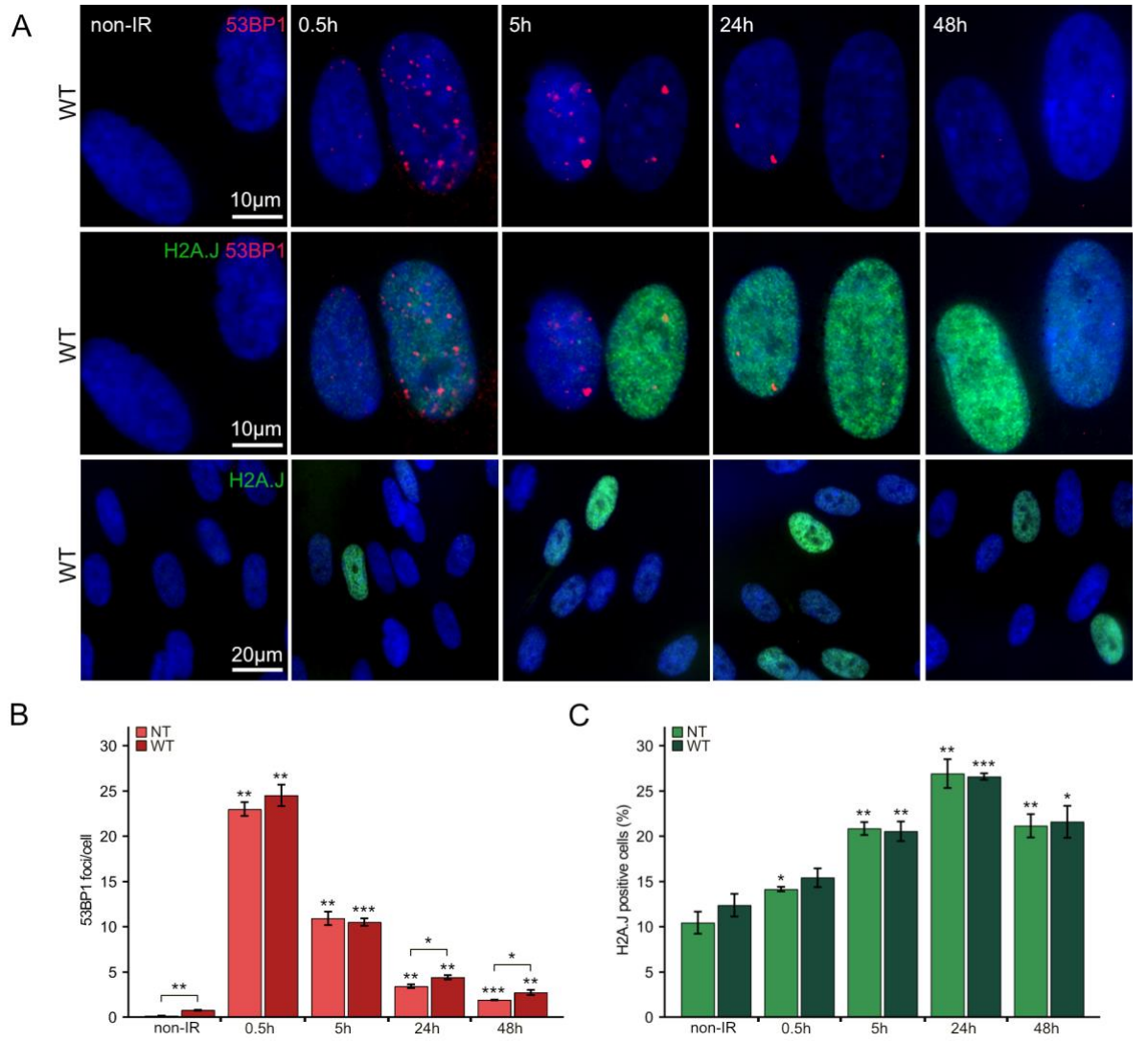

Figure 8. H2A.J accumulation following 2Gy irradiation.
(A) IFM micrographs of non-irradiated control and 2Gy irradiated WT and NT fibroblasts stained for H2A.J and 53BP1. (B) Quantification of 53BP1 foci in non-irradiated control and 2Gy irradiated WT and NT fibroblasts. (C) Quantification of H2A.J positive cells in non-irradiated control and 2Gy irradiated WT and NT fibroblasts. Data is presented as mean of 3 technical replicates ± SEM. Significant statistical difference * ($p < 0.05$), ** ($p < 0.01$), *** ($p < 0.001$).

6.2 H2A.J accumulation is dose dependent

Following the observation that H2A.J accumulated following a single exposure to 2Gy and the highest levels were found 24h post-IR, a further in depth dose response study was completed in which WT fibroblasts were irradiated with varying doses ranging from comparatively low to high (0.1Gy, 1Gy, 2Gy, 10Gy) and examined 24h post-IR (Figure 9). Notably, 24h after irradiation, H2A.J-positive cells increased significantly following each dose compared to non-irradiated control. Even after the lowest dose of 0.1Gy, a rise from 13.9 ±0.8% non-IR to 16 ±0.72% H2A.J-positive cells was detected. Additionally, the higher the dose, the greater the increase in H2A.J-positive cells (0.1Gy; 16 ±0.72%, 1Gy; 27.7 ±2.9%, 2Gy; 29.6 ±0.7%, 10Gy; 40 ±3.3%) .

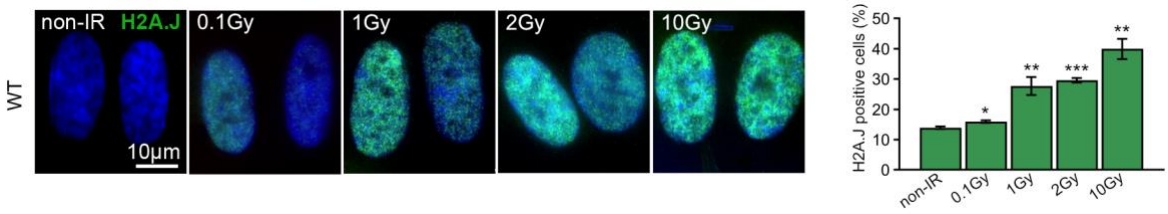

Figure 9. H2A.J accumulation following various doses
IFM images and quantification of H2A.J positive cells in WI-38 fibroblasts 24 h after IR with varying doses. Data is presented as mean of 3 technical replicates ± SEM. Significant statistical difference * ($p < 0.05$), ** ($p < 0.01$), *** ($p < 0.001$).

6.3 Higher doses result in altered H2A.J kinetics

Subsequently, a repair kinetic combined with H2A.J was completed in NT fibroblasts to investigate the effect of different doses on the kinetics of H2A.J accumulation (Figure 10). Exposure to 10Gy and 20Gy caused significantly greater amounts of DNA damage for all time points post-IR. 20Gy consistently generated the highest levels of DNA damage, with the maximum at 0.5h post-IR (36 ±0.9 foci/cell) and the minimum at 48h post-IR (9.3 ±0.9 foci/cell). 2Gy and 10Gy had similar peaks at 0.5h (23 ±0.7 foci/cell, 24 ±1.0 foci/cell respectively), however, repair was less efficient after 10Gy, where persistent foci levels at 48h post-IR reached 4 ±0.4 foci/cell compared to 2Gy with only 2 ±0.04 foci/cell. The effect of varying DNA-damage levels and persistent DNA damage foci 48h post-IR was reflected in H2A.J positive cells. 10Gy and 20Gy IR showed significantly higher values of H2A.J positive cells at all-time points following IR compared to values after 2Gy IR, which corresponds to what was observed in the previous section. However, additionally, while H2A.J positive cells declined by 48h after 2Gy (21.1 ±2.8%) compared to the peak at 24h (26.9 ±1.6%), abundance of H2A.J positive cells after 10- and 20Gy continued to rise from 24h to 48h post IR (10Gy;24h: 32.6 ±2.1%, 10Gy;48h: 34.1 ±1.8% , 20Gy;24h: 33.6 ±2.8%, 20Gy;48h: 44.1 ±4.1%).

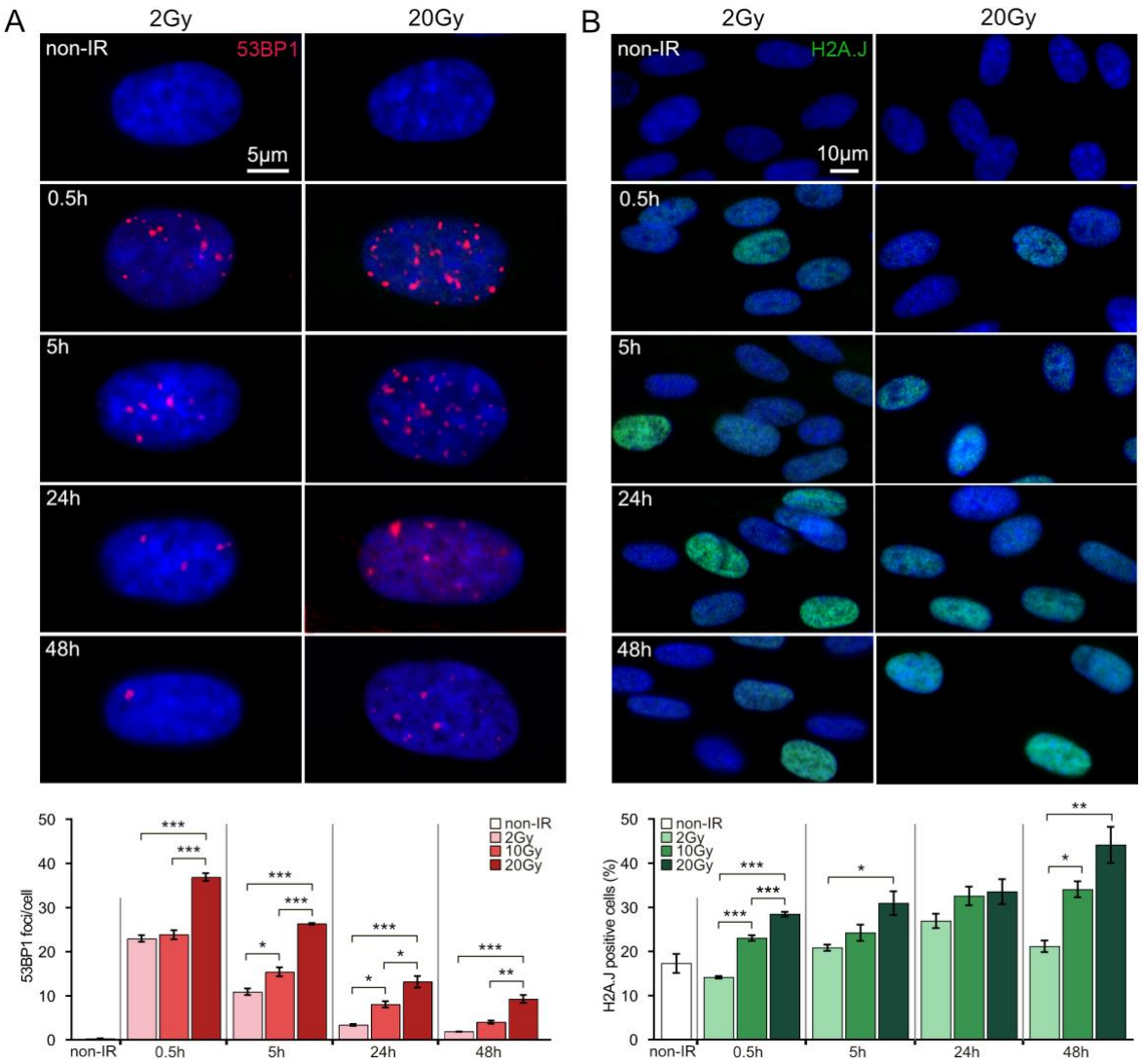

Figure 10. Effect of varying doses on H2A.J accumulation kinetics
(A) IFM micrograph and quantification of 53BP1 foci in NT fibroblasts irradiated with 2Gy, 10Gy and 20Gy compared to non-irradiated controls. (B) IFM micrograph and quantification of H2A.J positive cells in NT fibroblasts irradiated with 2Gy, 10Gy and 20Gy compared to non-irradiated controls. Data is presented as mean of 3 technical replicates ± SEM. Significant statistical difference * ($p < 0.05$), ** ($p < 0.01$), *** ($p < 0.001$).

6.4 H2A.J has no effect on DSB repair capacity

The next logical step after demonstrating the pivotal role which DNA-damage has on the induction and accumulation of H2A.J was to investigate whether H2A.J, like γH2A.X, influences DNA damage repair response. KD and NT fibroblasts were irradiated with 20Gy and their repair kinetics compared. Figure 11A and B clearly demonstrate that H2A.J knockdown was effective. The repair kinetics of both cell lines, whether they contain H2A.J or not, follow the same progression with no significant difference in values between the two at any time point except 48h post-IR. Here we see a statistically significant difference in the two cell lines in 53BP1 foci numbers 48h post-IR (NT: 9.3 ±0.9 foci/cell, KD: 6.9 ±0.2 foci/cell).

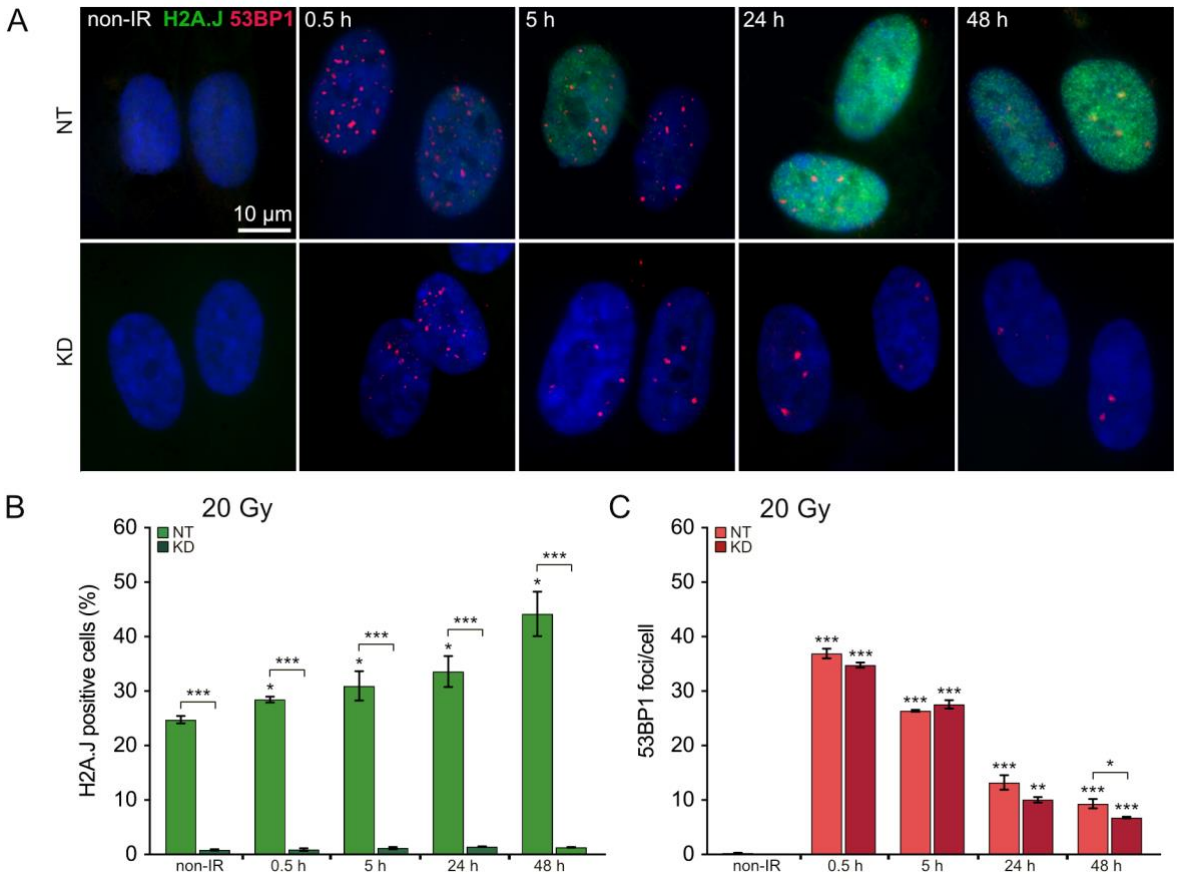

Figure 11. Investigation of H2A.J on repair capacity of fibroblasts following 20Gy irradiation.
(A) IFM micrographs of NT and KD fibroblasts following 20Gy irradiation stained for 53BP1 and H2A.J. (B) Quantification of H2A.J positive cell accumulation in NT and KD fibroblasts following 20Gy IR compared to non-irradiated control. (C) Quantification of acute 53BP1 foci in NT and KD fibroblasts following 20Gy IR compared to non-irradiated control. Data is presented as mean of 3 technical replicates ± SEM. Significant statistical difference * ($p < 0.05$), ** ($p < 0.01$), *** ($p < 0.001$).

6.5 Long-term H2A.J accumulation following irradiation

To this point only acute H2A.J accumulation had been examined, in which it was seen that following high doses of IR (10- and 20Gy), H2A.J positive cells increased up to 48h post-IR. The question now arose how this progressed at later time points. NT and KD fibroblasts were irradiated with 20Gy, a dose known to induce premature senescence, and cultured for a further 2 weeks post-IR. Figure 12 clearly shows that in NT fibroblasts, H2A.J-positive cells increase more than 10-fold from the non-IR control (7.7±3.1%) to 2w post-IR (84.2 ±3.5%), whereas, the knock-down fibroblasts display negligible accumulation of positive cells at any time point ranging from 0.8 ±0.7% in non-IR control to 6.7 ±1.7% in irradiated samples. To elucidate the link between H2A.J and DNA-damage further, the number of 53BP1-positive cells was also quantified revealing a ≈ 8-fold increase in 53BP1-positive cells in both cell lines 2w post-IR (NT: 11.7 ±5.3% to 81.8 ±1.9%, KD: 8.8 ±5.3% to 79.3 ±4.1%) (Figure 12B). The importance of DNA-damage in H2A.J accumulation was also supported in a separate experiment where NT and KD cells were exposed to the DNA-damaging chemotherapy drug ETO (ETO) for 1w and 2w (Figure 12C).

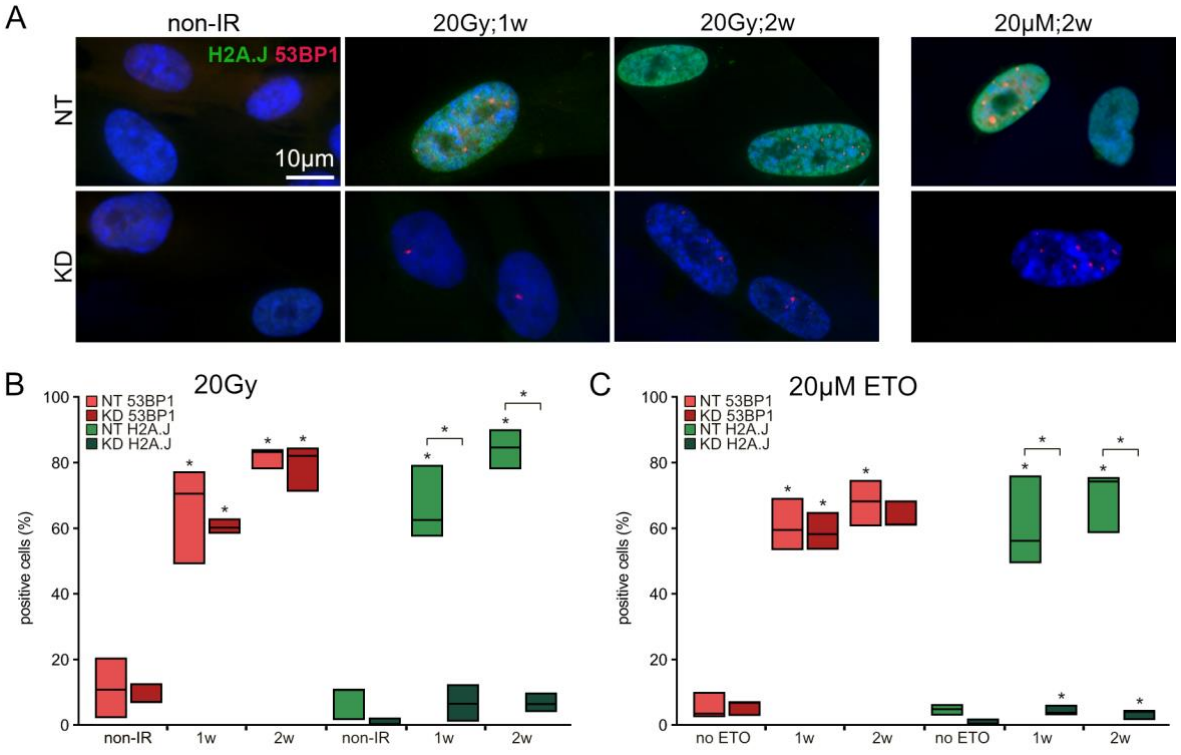

Figure 12. Long-term accumulation of H2A.J following 20Gy irradiation or continuous ETO exposure. (A) IFM micrograph of 53BP1-foci and H2A.J in NT and KD fibroblasts following 20Gy irradiation 1w and 2w after exposure, as well as NT and KD fibroblasts after continuous ETO exposure over 2w compared to non-irradiated/non-ETO exposed control. (B) Quantification of H2A.J- and 53BP1-positive cell accumulation in NT and KD fibroblasts following 20Gy IR, 1w and 2w following irradiation compared to non-irradiated controls. (C) Quantification of H2A.J- and 53BP1-positive cell accumulation in NT and KD fibroblasts following 1w and 2w continuous ETO exposure compared to non-exposed controls. Data is presented as median, maximum and minimum of 3 technical replicates. Significant statistical difference * (p <0.05).

Both NT and KD fibroblasts showed ~12 fold ETO induced increase in 53BP1-positive cells (NT: 5.3 ±2.4% to 67.8 ±4.1%, KD: 5.6 ± 1.4% to 63.5 ±2.5%) with no significant difference between cell lines (Fig. 8C). NT cells showed a significant ~15-fold increase in H2A.J-positive cells following ETO exposure with the maximum being reached after 2w ETO exposure (non-IR; 4.6 ±1%, 1w; 60.5 ±8%, 2w; 69.5 ±5.5%). As expected, H2A.J KD fibroblasts again showed negligible numbers of H2A.J positive cells (non-IR; 0.9 ±0.6%, 1w; 4.3 ±1%, 2w; 3.4% ±1).

6.6 H2A.J in radiation-induced premature senescence

SA-β-gal staining is widely accepted as a biomarker for senescent cells and indicates increased activity of lysosomal acid β-galactosidase at pH6. To determine whether H2A.J is essential to senescence induction, NT and KD cells were stained for SA-β-gal and H2A.J following a senescence-inducing dose of 20Gy and a maximum of 2w in culture post-IR. Analysis showed (Figure 13B and C) both NT- and H2A.J knock-down KD cells stained SA-β-gal positive with a ~3 to 4-fold rise just 24h post-IR. The greatest increase in SA-β-gal positive cells was seen 1w- (NT: 90.7 ±3.1%; KD: 94.7 ±2.6%) and 2w (NT: 92.6 ±3.3%; KD: 96.3 ±1.6%) post-IR. No significant difference was observed between NT and KD cell lines for SA-β-gal. Notably, in NT fibroblasts, almost all cells which stained positive for H2A.J were positive for SA-β-gal (H2A.J/ SA-β-gal; 24h: 37.5 ±2.9% /32.5 ±%, 1w: 90.7 ±5.7% /90.8 ±3.1%, 2w: 94.2 ±1.7% /92.6 ±3.3%). NT and KD cells exposed to ETO again showed very similar progressions for both H2A.J and SA-β-gal (Figure 13A and C). To support SA-β-gal data and further determine the senescent state of our irradiated cell population, additional senescence markers in the form of p21 and ki67 were evaluated in non-IR NT and KD fibroblasts and those exposed to 20Gy;2w post-IR (Figure 13D and E). Cyclin/cyclin-dependent kinase (CDK) complexes that mediate cell cycle progression can be inhibited by p21 in senescent cells and thus it can be used as an additional senescence marker. Quantification of p21 positive cells in both NT and KD fibroblasts revealed non-IR probes contained negligible amounts of p21 positive cells (NT: 1.1 ±0.6%, KD: 0.45 ±0.2%), however, these values rose dramatically two weeks post 20Gy IR (NT: 75.2 ±6.4%, KD: 75.3 ±5.5%) (Figure 13D). Both NT and KD fibroblasts showed no significant differences in p21 positive cell values. Another senescence characteristic is permanent proliferative arrest which can be assessed by staining for a proliferation marker such as ki67 (Figure 13E). Non-IR semi-confluent WT and NT fibroblasts showed high ki67 values ranging from 61.7±8.1% in NT fibroblasts and 66 ±4.7% in KD fibroblasts. Two weeks after 20Gy irradiation however, these values had dropped dramatically to 1.6 ±0.6% (NT) and 1.3 ±0.6% (KD) respectively.

As with previous senescence markers, both NT and KD fibroblasts displayed no significant divergence in proliferation rates and both showed a dramatic decrease following 20Gy;2w.

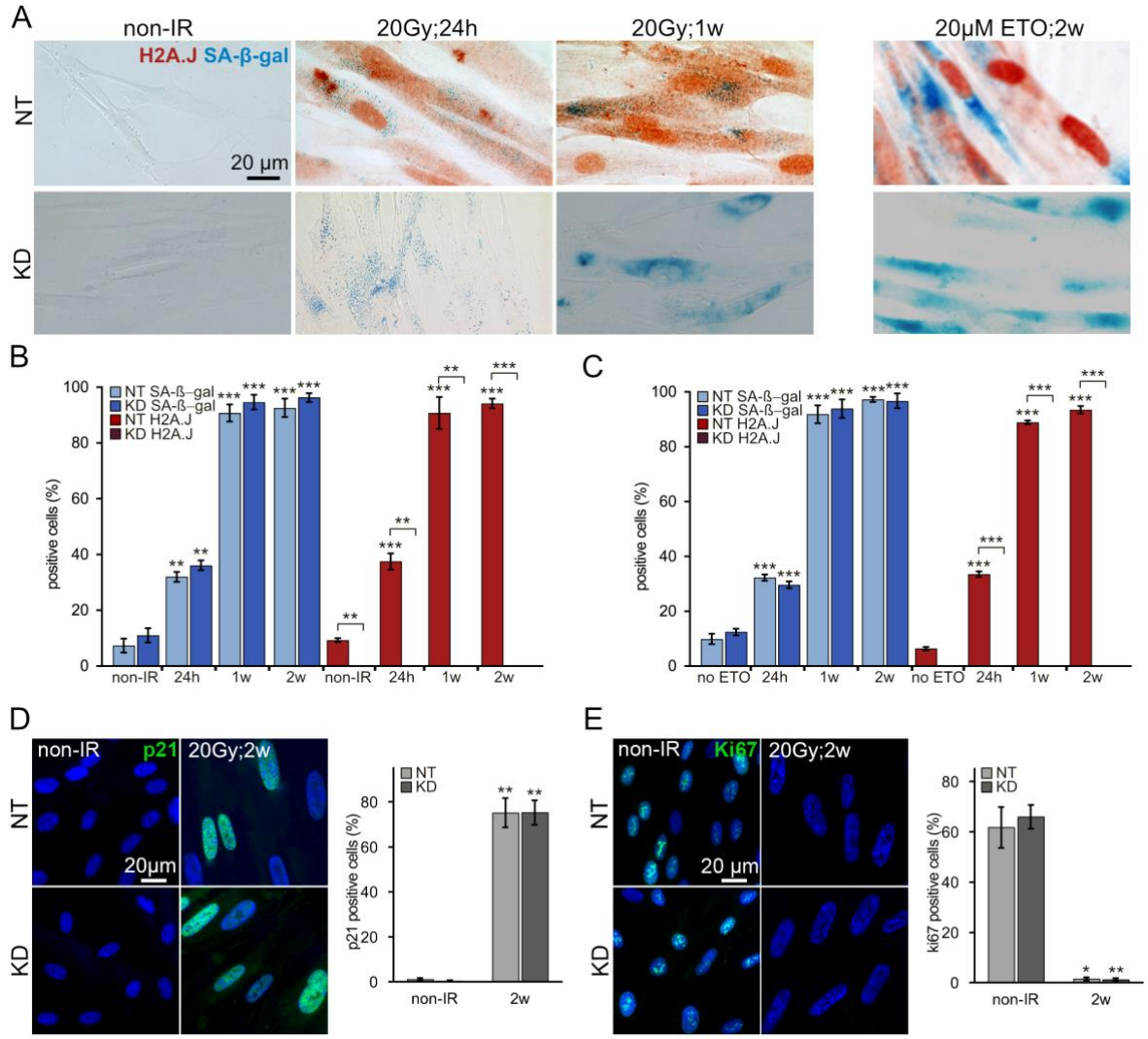

Figure 13. Long-term accumulation of SA-β-gal/H2A.J following 20Gy irradiation or continuous ETO exposure.
(A) Representative images of IHC staining for SA-β-gal/H2A.J in NT and KD fibroblasts following 20Gy irradiation or continuous 20µM ETO exposure compared to non-treated controls. (B) Quantification of SA-β-gal- and H2A.J-positive cell accumulation in NT and KD cells following 20Gy IR, 24h, 1w and 2w post-IR compared to non-irradiated controls. (C) Quantification of SA-β-gal- and H2A.J-positive cell accumulation in NT and KD fibroblasts following 24h, 1w and 2w continuous ETO exposure compared to non-exposed controls. Data is presented as mean of 3 technical replicates ± SEM. Significant statistical difference * ($p < 0.05$), ** ($p<0.01$), *** ($p<0.001$).

6.7 Effect of H2A.J on nuclear lamina decline in IR-induced senescence

WI-38 fibroblasts in radiation-induced senescence have been shown to display morphological changes which greatly differentiate from their proliferating counterpart, including the breakdown of the nuclear lamina. Amongst others, lamine B1 declines in the nuclear lamina when cells are in senescence, having a knock on effect on the chromatin organization. Figure 14 demonstrates the decline of the nuclear lamina in murine and human epidermis with age, as well as, in WI-38 fibroblasts which have entered replicative senescence. Of note is the observation that H2A.J positive cells correlate with a declined lamine B1 signal.

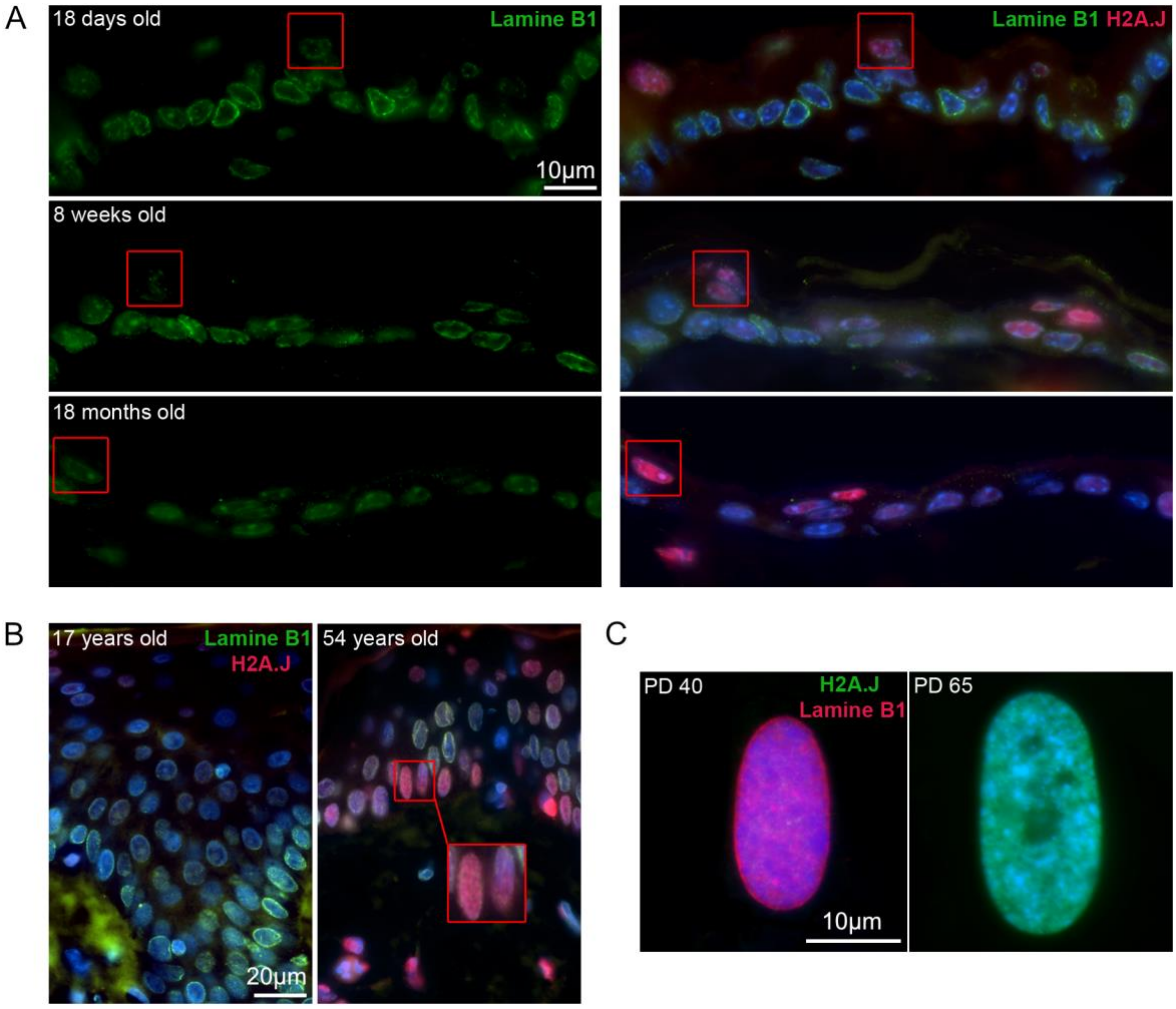

Figure 14. Lamine B1 decline in various tissues and cell lines with age.
(A) IFM images of lamine B1 (green) and H2A.J (red) in the epidermis of young (18 days old), adult (8 weeks old) and old (18 months old) mice. Boxed regions highlight examples of particularly strong lamine B1 decline corresponding with H2A.J positivity. (B) IFM images of lamine B1 (green) and H2A.J (red) in young (17 year old) and aged (54 year old) human epidermis. Boxed regions highlight examples of particularly strong lamine B1 decline corresponding with H2A.J positivity. (C) IFM images of lamine B1 (red) and H2A.J (green) WI-38 fibroblasts following varying population doublings. PD65 cells have reached replicative senescence and show a strong lamine B1 decline together with a stark H2A.J accumulation.

Following this observation, NT and KD fibroblasts were studied to discover whether H2A.J knock-down had an effect on the nuclear lamina and its senescence-associated decline. Lamine B1 fluorescent intensity was measured per cell and normalized to individual DAPI fluorescent intensities (Figure 15). As expected, non-IR NT and KD fibroblasts showed the highest levels of lamine B1. Mann-Whitney-U test indicated that normalized intensity of NT cells (Mdn=0.80) was significantly higher than in KD fibroblasts (Mdn=0.68), U=108452, p=<0.0001. Both cell lines displayed a significant decrease 2w post-IR (20Gy). Lamine B1 fluorescence in NT fibroblasts decreased from a median of 0.80 to 0.42 (U=12812, p=<0.0001). In KD fibroblasts a decrease from median 0.68 to 0.33 was observed (U=12277, p=<0.0001). As with the non-IR controls, 20Gy irradiated NT lamine B1 values (Mdn=0.42) were higher than KD values (Mdn=0.33) U=86569, p=<0.0001, 2w post-IR.

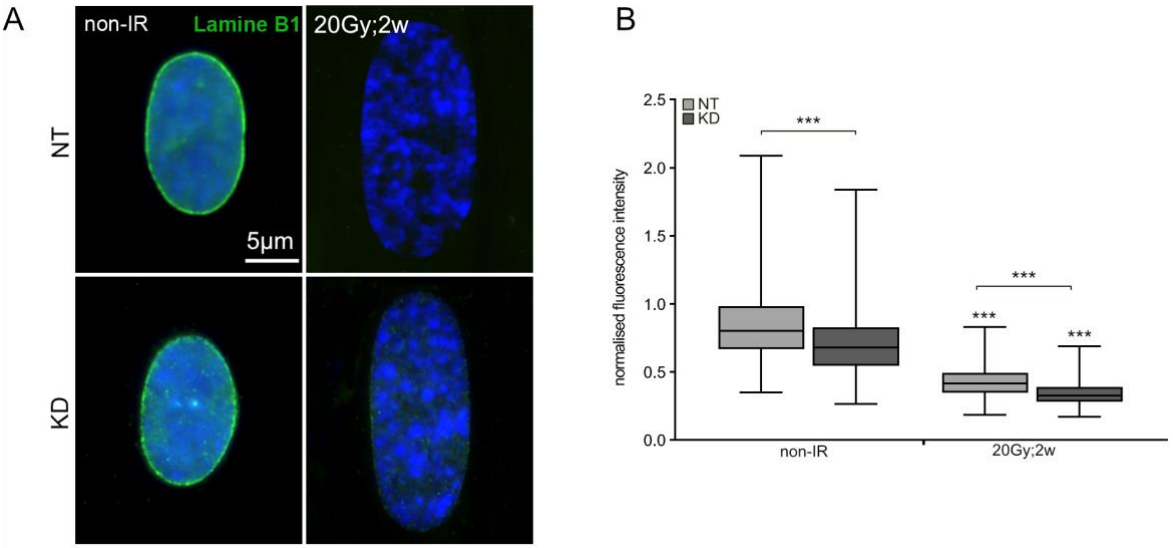

Figure 15. Lamine B1 decline in NT and KD fibroblasts following 20Gy irradiation
(A) IFM micrograph of lamine B1 in NT and KD fibroblasts following 20Gy;2w and compared to non-IR controls. (B) Box plot representing quantification of normalised fluorescence intensity of lamine B1 in NT and KD fibroblasts 20Gy;2w compared to non-IR controls. Data are shown as box plot with median, upper/lower quartiles and minimum/maximum values, n= 200 cells measured in each of 3 technical replicates.

6.8 H2A.J and senescence-associated heterochromatin foci formation

Senescence-associated heterochromatin foci can be quantified using DAPI staining alone. Non-senescent cells show a homogenous DAPI signal representing the less compact chromatin associated with this state. In a senescent cell, altered chromatin can be visualized in the form of DAPI-dense SAHF. Additionally, the SAHF core is known to be H3K9me3 rich and their peripheries high in H3K27me3, both of which are associated with heterochromatin.

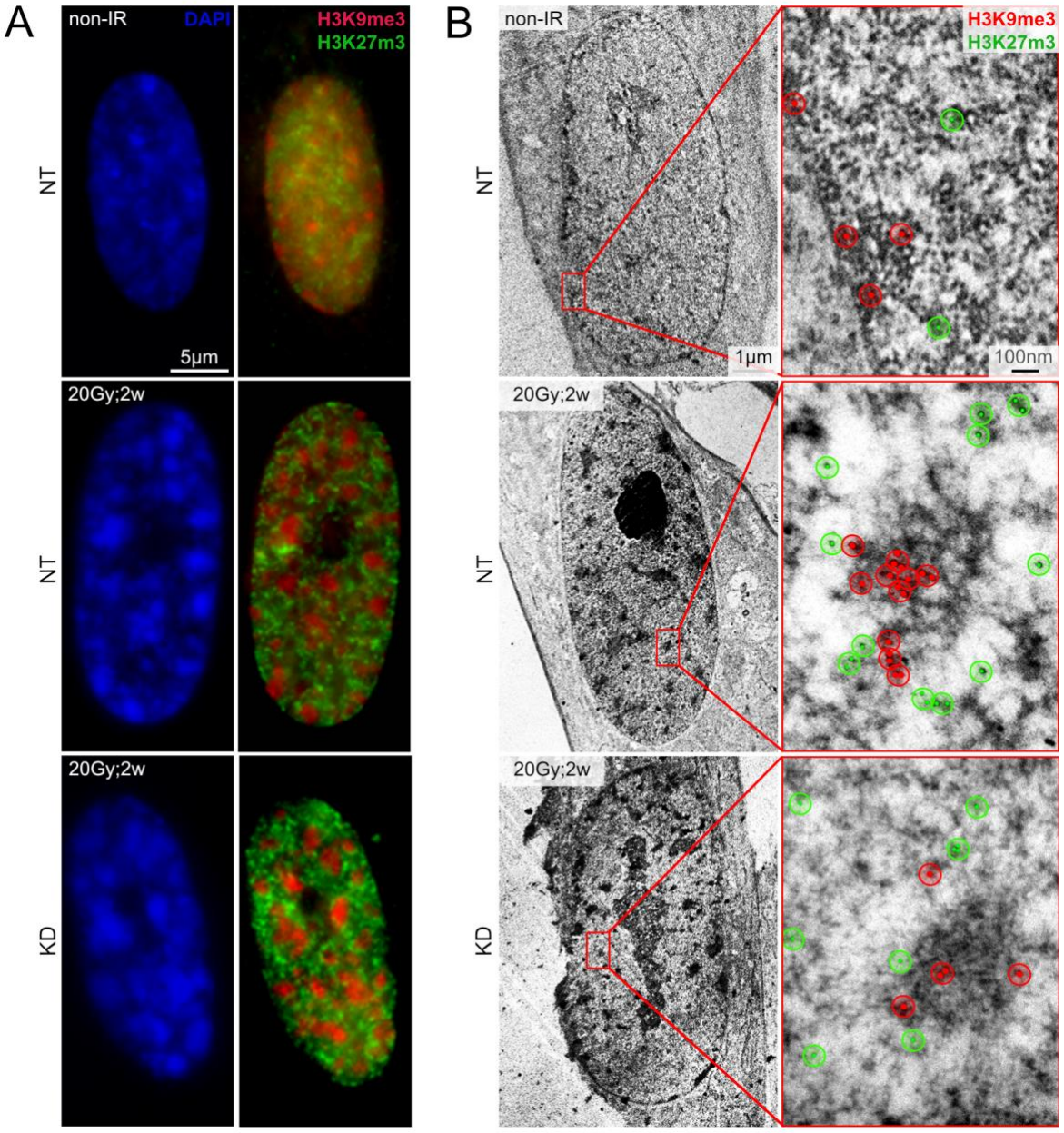

Figure 16. Senescence associated heterochromatin foci in presence and absence of H2A.J
(A) Representative IFM images showing DAPI-stained DNA and H3K9me3/k27me3 rearrangement in non-senescent versus radiation-induced senescent NT and sh3 fibroblasts. (B) Representative TEM images showing uranylacetate contrasted chromatin labelled with H3K9me3/K27me3 in non-senescent versus radiation-induced senescent NT and sh3 fibroblasts. Enlarged insets show gold-beads distinguishable by their size (6- and 10nm) overlaid with colors to aid visualization (H3K9me3; red, H3K27me3; green). TEM staining, images and analysis provided by Dr.rer.med.Y.Lorat.

Figure 16A demonstrates the change in both DNA-staining DAPI and heterochromatin-associated H3K9me3 and H3K27me3 from a non-IR control to an IR-induced senescent cell (20Gy;2w). It is evident that WI-38 fibroblasts formed SAHF irrespective of the presence of H2A.J. Figure 16B displays representative images of TEM analysis whose high-resolution enables visualization of chromatin itself. The chromatin rearrangements seen in the nucleus overview correlate with those seen in IFM. Sections were stained for H3K9me3 and H3k27me3 and labelled with gold beads enabling visualization of DAPI dense SAHF cores seen in IFM surrounded by H3K27me3. IFM and TEM analysis revealed no difference in the structure of the SAHF, however, an additional experiment was required to determine the frequency of SAHF positive cells, as not all cells, form SAHF in senescence. SAHF positive cells were quantified in NT and KD fibroblasts at 20Gy;2w and in non-irradiated controls (Figure 17A).

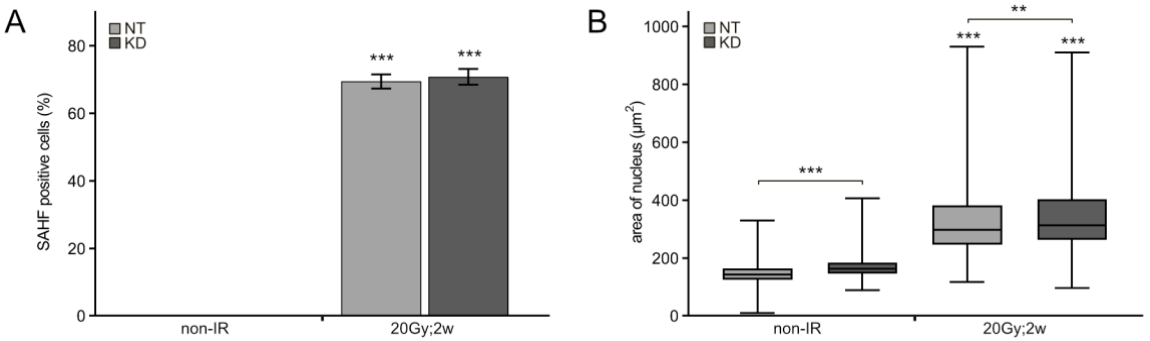

Figure 17. Effect of H2A.J on nuclear morphology of NT and KD fibroblasts in IR-induced senescence. (A) Quantification of SAHF-positive NT and KD fibroblasts 2w post-IR (20Gy) radiation compared to non-IR controls. Data is shown as mean of 3 technical replicates ±SEM. (B) Measurement of nuclear area (µm^2) of NT and KD fibroblasts 2w after 20Gy irradiation compared to non-IR controls. Data are shown as box plot with median, upper/lower quartiles and minimum/maximum values, n=3 technical replicates. Significant statistical difference * (p <0.05), ** (p<0.01), *** (p<0.001).

In non-IR NT and KD fibroblasts no SAHF-positive cells could be detected. A significant increase in SAHF-positive cells could be seen in both cell lines from non-IR fibroblasts (NT: 0%, KD: 0%) to 20Gy;2w post-IR (NT: 69.5 ±3.7%, KD: 70.8%). When comparing both cell lines under identical conditions however the data was not significantly different. Nuclei of senescent fibroblasts not only undergo a major overhaul in chromatin structure, they also become enlarged and flattened. Investigation of this phenomenon in senescent NT and KD fibroblasts was assessed by measuring the area of nuclei in non-irradiated and 20Gy irradiated fibroblasts 2w post-IR (Figure 17B). In NT fibroblasts the median nuclear area lay at 149.2µm^2 which significantly increased to 297.6µm^2 in irradiated samples (20Gy;2w) U=7012, p=<0.0001. The median area of non-irradiated KD nuclei lay at 163.9µm^2 increasing to 312.9µm^2 (U=9649, p=<0.0001) 2w post-IR (20Gy). Further statistical analysis between NT and KD fibroblasts revealed that KD cells in non- irradiated samples had a significantly larger nuclear area (Mdn=163.9µm^2) compared to their NT counterpart (Mdn=149.2µm^2)

U=112911, p=<0.0001. Evaluation by Mann-Whitney-U of the irradiated samples (20Gy;2w) revealed the same was also true where KD nuclear area (Mdn=312.9µm^2) was significantly larger than radiated NT fibroblasts (Mdn=297.6µm^2; U=160148, p=0.0009).

6.9 Senescence-associated secretory phenotype (SASP)

As senescence is a heterogenic state and varies depending on induction method, the effect of high radiation dose on SASP was investigated in the presence and absence of H2A.J.

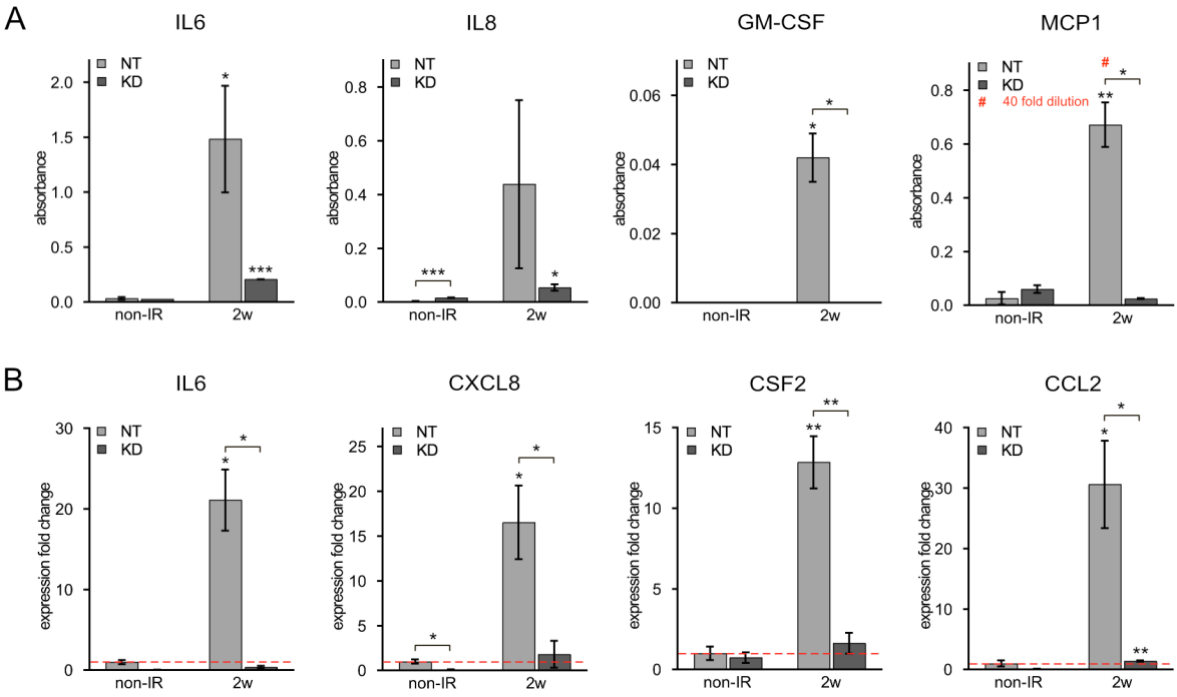

Figure 18. SASP analysis in following 20Gy irradiation
(A) ELISA analysis of SASP factors in conditioned medium of non-IR and 20Gy;2w IR NT and KD fibroblasts showing variation in SASP levels of senescence cells versus non-IR control cells and the effect of H2A.J absence on SASP profile. (B) RT-qPCR analysis of SASP gene expression in non-IR and 20Gy;2w IR NT and KD cells and the effect of H2A.J absence on SASP gene expression. Data is presented as mean of 3 technical replicates ± SEM. Significant statistical difference * (p <0.05), ** (p<0.01), *** (p<0.001). # indicates 40-fold dilution of conditioned medium required to ensure results lay within linear range of assay.

ELISA was used to quantify relative increase of IL6, IL8, Gm-csf and MCP1 in IR-induced senescent NT and KD fibroblasts compared to non-irradiated controls (Figure 18A). IL1β, IL12, IFNγ, TNFα, MIP-1α, TGFβ1, IP10 and GROα were also tested but levels were not detectable by ELISA. NT cells showed an increase in absorbance for all four factors in irradiated fibroblasts (20Gy;2w) compared to non-IR controls. Absorbance for IL6 rose ~21-fold, IL8 rose ~149-fold and Gm-csf rose from 0 to 0.04 ±0.007 (p=0.02) respectively. MCP1 levels in IR fibroblasts where so high that samples had to be diluted 40-fold to ensure absorbance lay within linear range of assay. Despite dilution, MCP1 levels still showed a significant increase compared to non-IR NT fibroblasts (non-IR; 0.05 ±0.02, 20Gy;2w; 0.67

±0.08, p=0.0019). KD cells showed no such dramatic increases and SASP factors were severely reduced in irradiated KD fibroblasts compared to NT fibroblasts (IL6: ~2-fold decrease, IL8: ~8-fold decrease, Gm-csf: ~42-fold decrease, MCP1: 22-fold decrease). Additionally, the equivalent SASP gene expression profiles of these fibroblasts were also analyzed. A significant expression fold change was observed in NT fibroblasts following IR compared to non-IR controls (IL6; 21.04 ±3.9 fold, p=0.03, CXCL8; 16.5 ±4.11 fold, p=0.01, CSF2; 12.8 fold ±1.6, p=0.002, CCL2; 32.3 fold ±6.7, p=0.04).

6.10 DNA-SCARS identification

Formation and stability of DNA-SCARS has been linked to SASP expression. Therefore NT and KD fibroblasts were investigated in relation to DNA-SCARS formation and abundance. Firstly, however, presence of DNA-SCARS had to be determined and validated through numerous experiments. Similar to active DNA-repair foci, DNA-SCARS also contain 53BP1 and γH2A.X, uniquely however, PML-NB are always found in close proximity to DNA-SCARS. An IFM double stain of 53BP1 and PML distinguished the 53BP1 foci which were observed at later time points (1w and 2w) post-IR from acute DNA damage repair foci seen up to 24h post-IR (Figure 19).

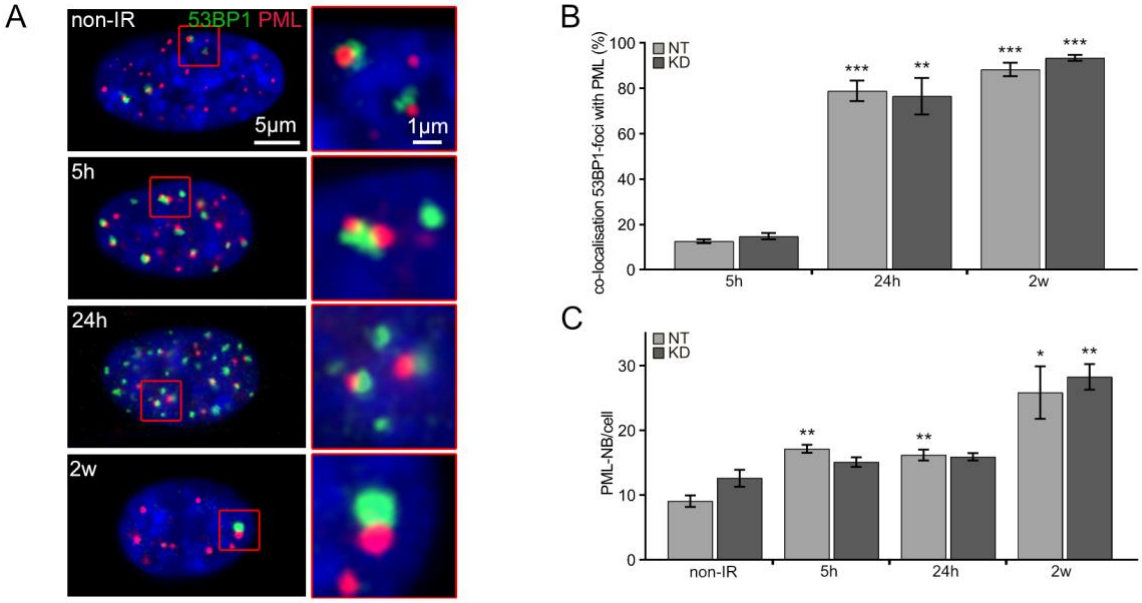

Figure 19. DNA-SCARS determination using IFM.
(A) Representative IFM images of 53BP1 and PML in non-IR and 20Gy irradiated NT fibroblasts 5h, 24h and 2w following exposure. Red boxes show magnified section highlighting presence and absence of co-localization between 53BP1 and PML under varying conditions. (B) Quantification of IR-induced 53BP1 foci which co-localized with PML in 20Gy irradiated NT and KD fibroblasts 5h, 24h and 2w following exposure. (C) Quantification of PML-NB in non-irradiated and 20Gy irradiated NT and KD fibroblasts 5h, 24h and 2w following exposure. Data is presented as mean of 3 technical replicates ± SEM. B shows statistical significance compared to 5h time point in which acute, active repair is underway and C shows statistical significance of irradiated controls at varying time points following exposure compared to non-irradiated control. Significant statistical difference * (p <0.05), ** (p<0.01), *** (p<0.001).

Although the number of 53BP1 foci is extremely high 5h post-IR (Figure 19A) only very few (NT; 12.7 ±1.4%, KD; 14.8 ±2.4%) of 53BP1 foci co-localize with PML-NBs (Figure 19 B). As acute repair takes place and foci number decline (24h post-IR), a shift occurs resulting in a significant increase in 53BP1/PML-NB co-localization (NT; 78.9 ±7.8%, KD; 76.6 ±14.1%). The greatest co-localization increase is seen when cells are senescent 2 weeks after 20Gy IR (NT; 88.3 ±5.1%, KD; 93.5 ±2.4%). A large number of PML-NB are present under non-IR conditions, however, the amount of PML-NBs are known to increase in response to stress. This rise in PML-NB was also evident in NT and KD fibroblasts following 20Gy IR (Figure 19C). Non-irradiated samples had a base level of 9.1 ±1.5 PML-NB per cell in NT fibroblasts and 12.6 ±2.2 PML-NB per cell in KD fibroblasts. A steady progression was observed post-IR in NT fibroblasts (5h; 17.1 ±1.1, 24h; 16.2 ±1.5, 2w; 25.8 ±3.4) and KD fibroblasts (5h; 15.1 ±1.3, 24h; 15.9 ±0.9, 2w; 28.3 ±3.4) respectively, with no difference in PML-NB accumulation levels between the two cell lines (Figure 19C).

TEM was used to view DNA-SCARS in the chromatin context (Figure 20B). DNA-SCARS where found to lie at the periphery of SAHF and a maximum distance of 0.75µm from the attributed SAHF. As was indicated by IFM analysis of 53BP1/PML and in sync with publications, PML is to be found adjacent to the 53BP1 foci. Inversely however, not all PML-NB amass around 53BP1 foci (Figure 20 B2 and B4). Through TEM, PML-only foci could clearly be distinguished from DNA-SCARS not only through 53BP1 absence but also by their chromatin structure. DNA-SCARS were found at the periphery of SAHF, whereas PML-only foci were located at the edge of much smaller and denser heterochromatin foci whose function is yet unknown (Figure 20 B1-4). Taken together, IFM and TEM data validate that persistent 53BP1 foci observed in NT and KD cells at 20Gy;2w are in fact DNA-SCARS.

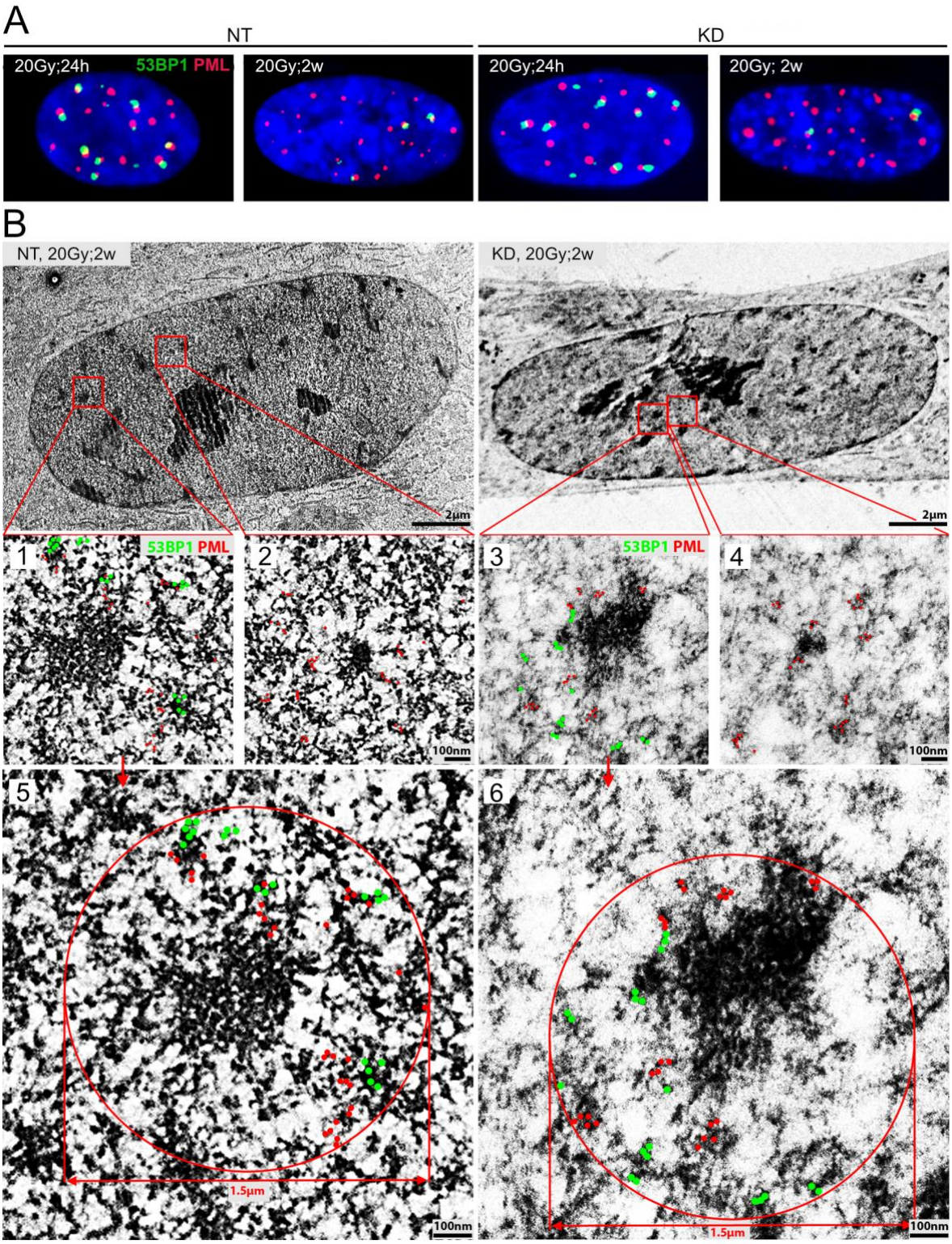

Figure 20. DNA-SCARS visualisation and localisation in chromatin context using IFM and TEM.
(A) IFM micrographs demonstrating localisation between PML and 53BP1 in NT and KD fibroblasts following 20Gy;24h and 2w after exposure. (B) TEM micrograph of gold-labelled PML and 53BP1 at varying magnifications in NT and KD fibroblasts following 20Gy;2w. Gold beads have been overlaid with colour to aid visualization (PML; red, 53BP1; green). B1, 2, 3 and 4 show variances between PML/53BP1 foci and PML-only foci in chromatin context. B5 and 6 highlight localisation of PML/53BP1 foci localisation in relation to SAHF. Red circle shows maximum distance at which these PML/53BP1 foci were found from centre of SAHF. TEM staining, images and analysis provided by Dr.rer.med. Y.Lorat.

6.11 DNA-SCARS stability

Depletion of γH2A.X has been found to effect stability of DNA-SCARS resulting in an altered SASP. To investigate whether H2A.J has an effect on DNA-SCARS stability, both non-irradiated and 20Gy irradiated NT and KD fibroblasts where pulse-labelled with BrdU for 24h prior to fixation (Figure 21). Both NT and KD fibroblasts showed high levels of BrdU positive cells due to proliferation during 24h pulse labelling (NT; 52.83 ±9.5%, KD; 52.6 ±2.1%) period. 2w post 20Gy IR however, cells were in senescence and no pan-nuclear BrdU incorporation was expected due to senescence-associated growth arrest. If, however, destabilization of DNA-SCARS was present, punctate BrdU incorporation would be expected. Knock-down of H2A.J however did not have an effect on DNA-SCARS stability as no punctate BrdU staining was observed in either NT or KD fibroblasts and only a negligible amount of BrdU positive cells were detected overall (NT; 1.08 ±0.1%, KD; 1.2 ±0.2%).

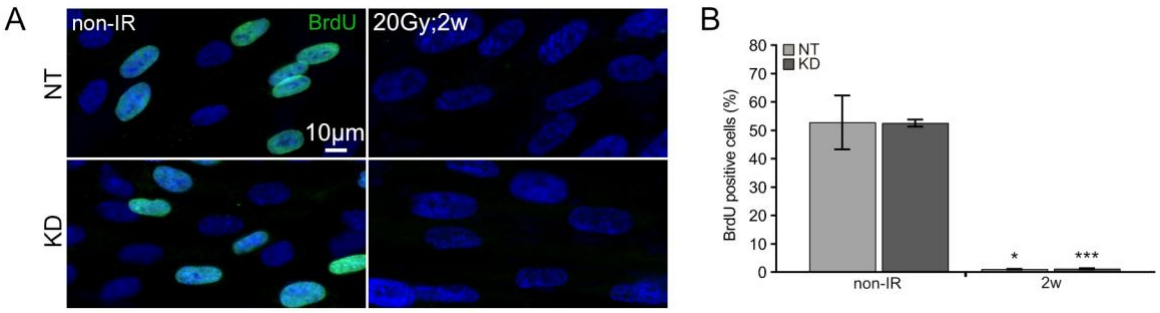

Figure 21. DNA-SCARS stability following H2A.J knock-down.
(A) Representative IFM images BrdU pulse-labelled NT and KD fibroblasts 2w post 20Gy IR compared to non-irradiated controls. (B) Quantification of BrdU positive NT and KD fibroblasts 2w following 20Gy IR compared to non-irradiated controls. Data is presented as mean of 3 technical replicates ± SEM. Significant statistical difference * ($p < 0.05$), ** ($p < 0.01$), *** ($p < 0.001$).

6.12 H2A.J preferentially localizes to DNA-SCARS

To further investigate potential H2A.J influence on DNA-SCARS, a proximity ligation assay was performed between 53BP1 and H2A.J to observe possible co-localization between these two proteins within DNA-SCARS in non-IR and 20Gy irradiated NT and KD fibroblasts (Figure 22). Foci are only present when anti-53BP1 and anti-H2A.J primary antibodies lie within 40nm of one another. Non-irradiated NT fibroblasts showed a baseline level of 5.9 ±1.6 foci/cell which rose significantly to 15.7 ±0.5 foci/cell 2w post-IR (20Gy). 20Gy radiated H2A.J knock-down cells showed minimal co-localization of 1.3 ±0.2 foci/cell. versus 20Gy irradiation-induced senescent NT and KD fibroblasts.

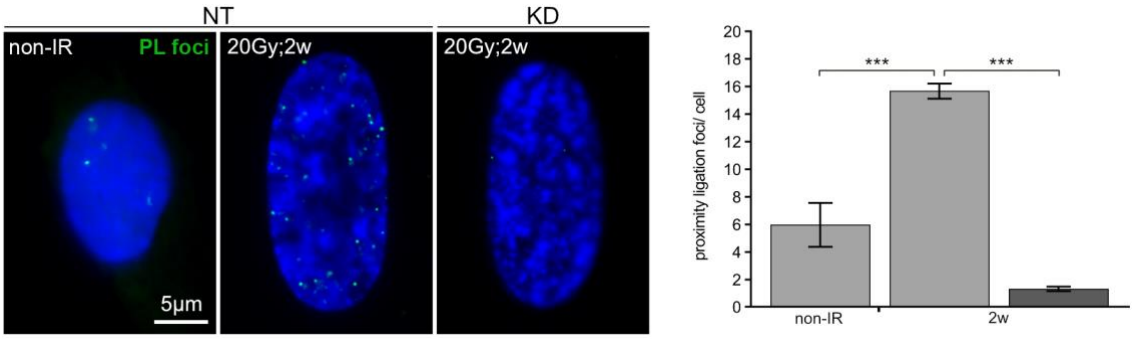

Figure 22. Proximity ligation assay between H2A.J and 53BP1
IFM micrograph and quantification of PLA foci between H2A.J and 53BP1 in non-IR NT fibroblasts compared to 20Gy;2w irradiated NT and KD fibroblasts. Data is presented as mean of 3 technical replicates ± SEM. Significant statistical difference * (p <0.05), ** (p<0.01), *** (p<0.001).

Consequently, NT and KD fibroblasts were analyzed using TEM to gain further insight into H2A.J localization to DNA-SCARS and its accumulation in the context of chromatin. Figure 23 highlights distribution patterns of gold-labelled H2A.J and 53BP1 in non-irradiated NT fibroblasts and 20Gy;2w post-IR NT and KD fibroblasts.

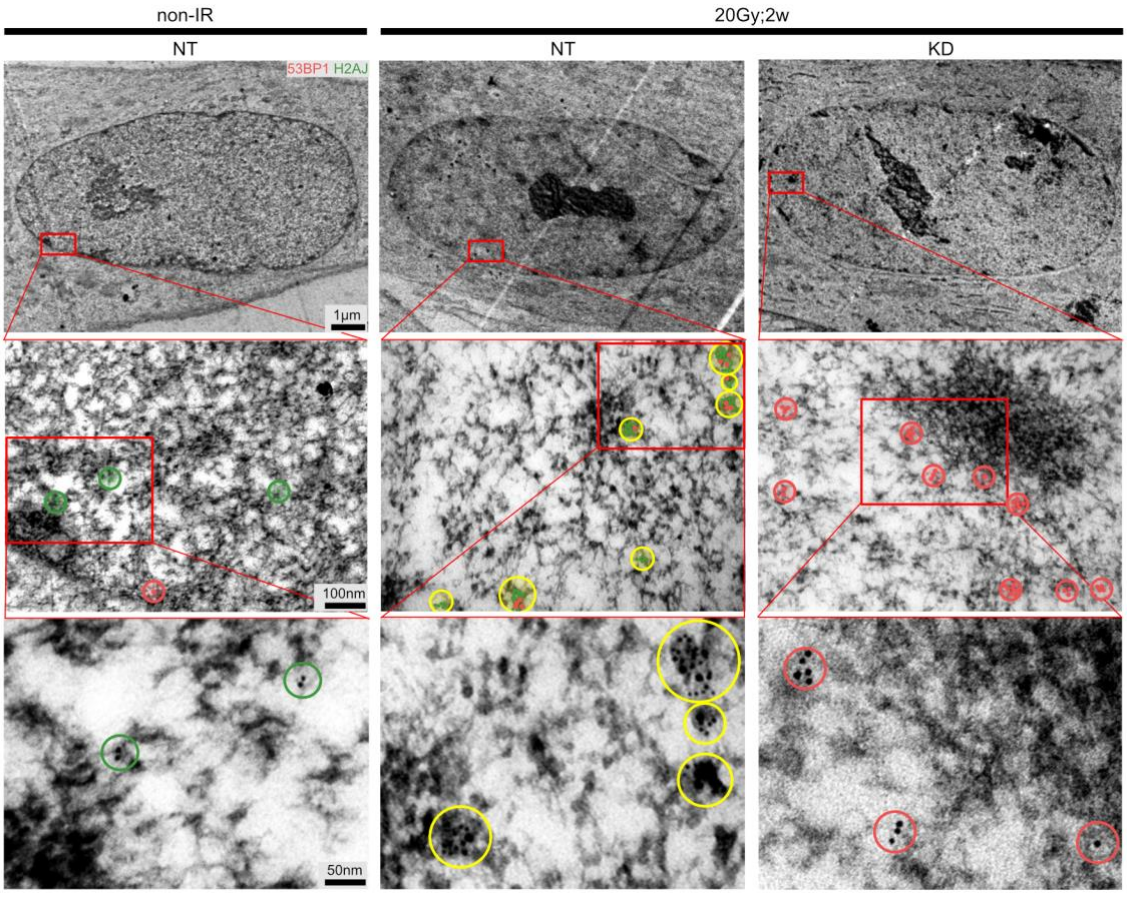

Figure 23. TEM analysis of H2A.J and 53BP1 in DNA-SCARS.
Row 2 shows magnified sections from nuclei in row 1 where gold-labelled 53BP1 and H2A.J were overlaid with colors to aid visualization (53BP1 red, H2A.J green). Row 3 shows magnified sections from row 2 displaying the original state of the gold beads. In both row 2 and 3 co-localization between H2A.J and 53BP1 is highlighted in yellow. TEM staining, images and analysis provided by Dr.rer.med. Y.Lorat.

H2A.J gold beads were quantified and their localization examined in the context of chromatin, SAHF and DNA-SCARS. Figure 24A clearly supports previous IFM data (Figure 12A and B) in which a marked increase in H2A.J can be seen 2w following 20Gy radiation. A highly significant ~20-fold increase of H2A.J beads from non-IR control to 2w post 20Gy-IR was observed in NT fibroblasts. Comparing NT to H2A.J KD cell lines revealed a significantly higher amount of H2A.J beads in non-IR NT fibroblasts (5.5 ±0.3 beads/section) than non-IR KD fibroblasts (0.5 beads/section ±0.1, $p<0.0001$). The difference of H2A.J beads in irradiated samples was even starker (NT; 117.2 ±7.7 beads/section KD; 1 ±0.1 bead/section). H2A.J beads were further classified into their localization within chromatin, as well as, their co-localization with 53BP1 (pan-nuclear, within DNA-SCARS, within DNA-SCARS and co-localizing with 53BP1) (Figure 24B). This revealed that H2A.J found in non-IR NT and KD cells, as well as 20Gy;2w post-IR KD cells, was only found within pan-nuclear regions and not within DNA-SCARS. (Figure 19B). Senescent NT cells (20Gy;2w) also showed increased pan-nuclear H2A.J accumulation however the majority of H2A.J (~58%) was located within DNA-SCARS. This is extremely noteworthy as DNA-SCARS were measured found to occupy only around 3% of nuclear section area. Additionally, ~92,9% of the H2A.J found in DNA-SCARS co-localized with 53BP1. H2A.J bead localization was further categorized and the size of the bead clusters captured with reference to their localization (Figure 24C). H2A.J beads within DNA-SCARS where most commonly found in large clusters (between 4 and 13 beads) whereas pan-nuclear H2A.J beads, regardless of cell type or irradiation status, were overwhelmingly found as single beads. Analysis of all H2A.J beads within DNA-SCARS (with- or without 53BP1 co-localization) supported this observation with ~94% of clusters containing 3 beads or more and ~65% of clusters containing 5 beads or more (Figure 24C). Cluster size prevalence in IR NT fibroblasts was found to be significantly, highly significantly or extremely significantly greater than the equivalent cluster size prevalence in IR KD fibroblasts for all cluster sizes apart from 10, 12, and 13 bead clusters.

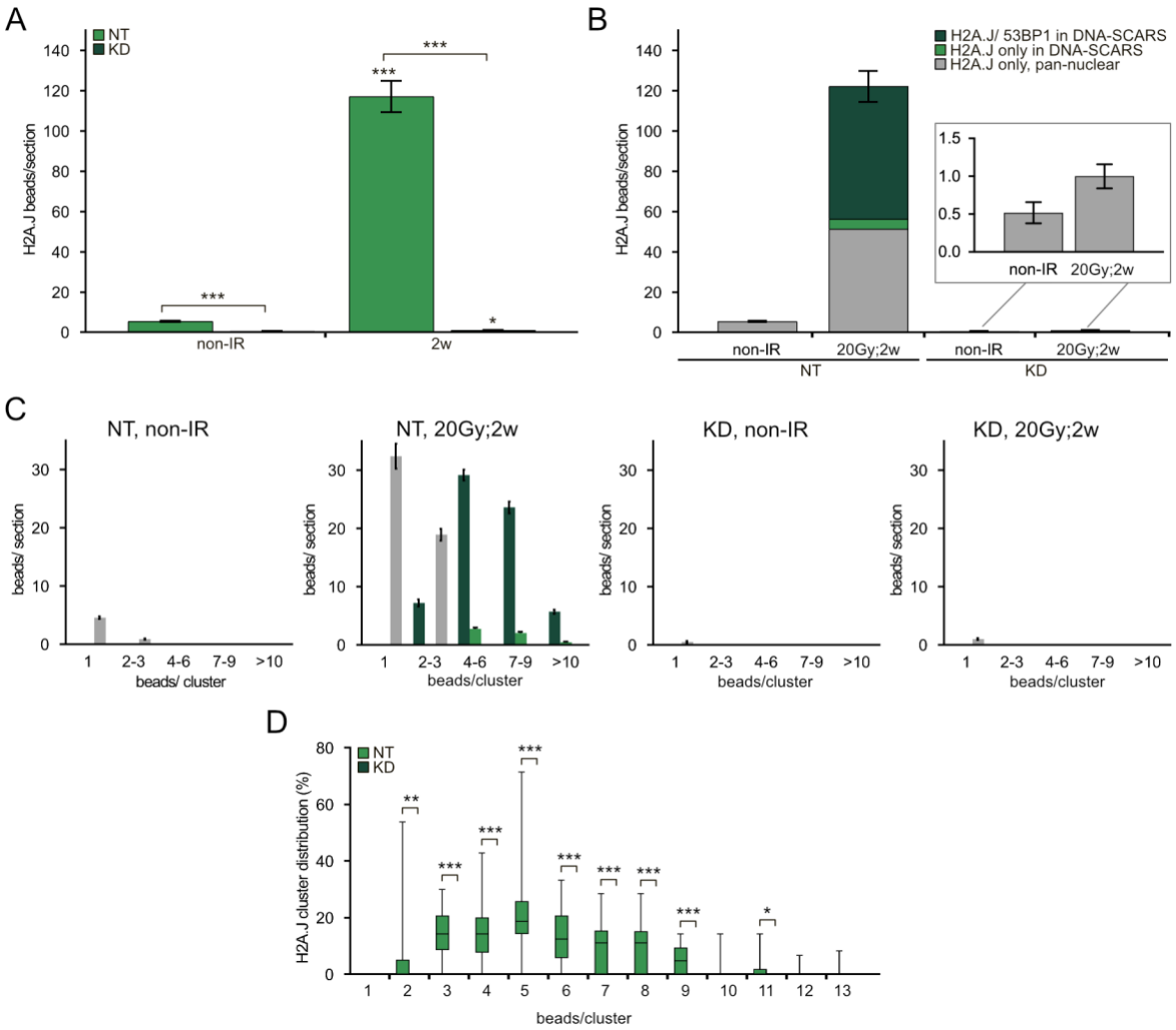

Figure 24. TEM quantification and localization analysis of H2A.J in the context of DNA-SCARS in non-IR and 20Gy;2w IR NT and KD fibroblasts.
(A) Quantification of total H2A.J beads/section (B) H2A.J beads classified into chromatin localization based on pan-nuclear H2A.J, H2A.J only located within DNA-SCARS and H2A.J co-localizing with 53BP1 within DNA-SCARS. (C) Bead cluster analysis of H2A.J in context of chromatin localization based on pan-nuclear H2A.J, H2A.J only located within DNA-SCARS and H2A.J co-localizing with 53BP1 within DNA-SCARS. (D) Prevalence of H2A.J cluster sizes with DNA-SCARS. Data in A and B presented as mean of H2A.J-labelling gold bead quantification within 25 nuclear sections ± SEM. Data in C and D shown as box plot with median, upper/lower quartiles and minimum/maximum values, n=25 nuclear sections. Significant statistical difference * ($p < 0.05$), ** ($p<0.01$), *** ($p<0.001$). TEM staining and raw data provided by Dr.rer.med. Y.Lorat.

6.13 53BP1 accumulation in chromatin context.

The structure of DNA-SCARS was further investigated in the form of 53BP1 foci quantification and area measurements to determine whether the absence of H2A.J has potential structural effects on DNA-SCARS which are not significant for DNA-SCARS stability. The quantity of 53BP1 foci was determined in non-IR NT and KD fibroblasts and compared to 20Gy IR equivalents 2w after exposure (Figure 25A and B). For both NT and KD fibroblasts a significant increase in DNA-SCARS/cell (marked by 53BP1) was seen. In NT fibroblasts, DNA-SCARS increased significantly from 0.1 ±0.005 foci/cell to 5.3 ±0.1 foci/cell ($p=0.0010$) 2w post-IR (20Gy). In KD fibroblasts DNA-SCARS increased significantly from 0.07 ±0.006 foci/cell to 6.5 ±0.5 foci/cell ($p=0.0051$). In irradiated samples, KD fibroblast

showed higher numbers of DNA-SCARS than NT fibroblasts, however, this was not shown to be a statistically significant difference. Additionally, the area of each of the 53BP1 foci was also measured revealing an increase in both NT and KD fibroblasts from 24h to 2w post-IR (Figure 25A and C). NT fibroblasts showed significant growth in median foci area of 0.250µm^2 to 0.551µm^2 (U=116367, p<0.0001). KD fibroblasts showed significant growth of median foci area of 0.247µm^2 to 0.460µm^2, (U=131027, p<0.0001). Notably, a significant difference in foci area was observed between NT and KD fibroblasts 2w after 20Gy IR (NT; mdn=0.551µm^2, KD; mdn=0.460µm^2, U=162559, p=0.0037).

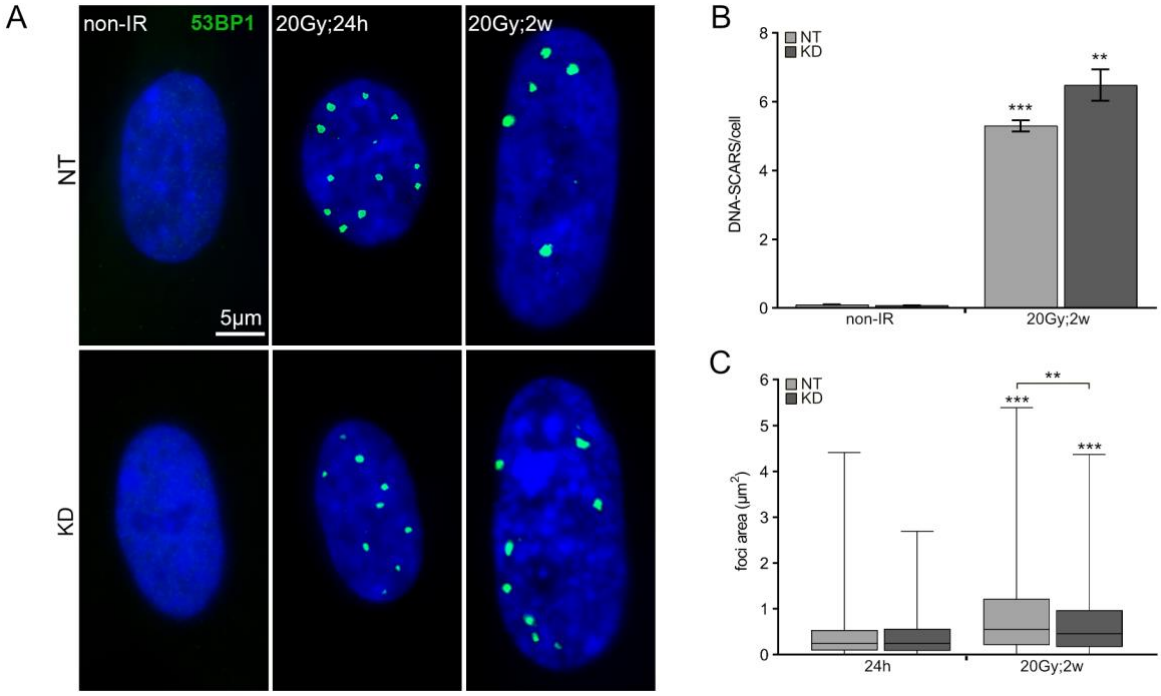

Figure 25. IFM examination of DNA-SCARS formation with respect to 53BP1 accumulation in NT and KD fibroblasts following 20Gy irradiation.
(A) IFM micrograph of 53BP1 foci within DNA-SCARS in non-irradiated controls and 20Gy irradiated NT and KD fibroblasts 24h and 2w after exposure. (B) Quantification of 53BP1 within DNA-SCARS in non-irradiated controls and 20Gy irradiated NT and KD fibroblasts 2w after exposure. Data is presented as mean 3 technical replicates ± SEM. (C) Area measurements of 53BP1 foci within DNA-SCARS in 20Gy irradiated NT and KD fibroblasts 24h and 2w after exposure. Data is presented as box plot with median, upper/lower quartiles and minimum/maximum values, n=3. Significant statistical difference * (p <0.05), ** (p<0.01), *** (p<0.001).

Subsequently, the higher resolution of the TEM was used to further investigate the difference observed in the IFM analysis and 53BP1 was examined in the same fashion as previously shown for H2A.J (Figure 23 and Figure 24) in respect to DNA-SCARS localization and accumulation in chromatin context. Figure 26A displays the overall 53BP1 beads per section in non-irradiated NT and KD fibroblasts compared to 20Gy;2w post-IR fibroblasts. NT fibroblasts show a ~10-fold rise in 53BP1 beads from non-irradiated fibroblasts (4.5 ±0.3 beads/section) to 20Gy irradiated fibroblasts 2w post-IR (44.68 ±4.4 beads/section, p<0.0001).

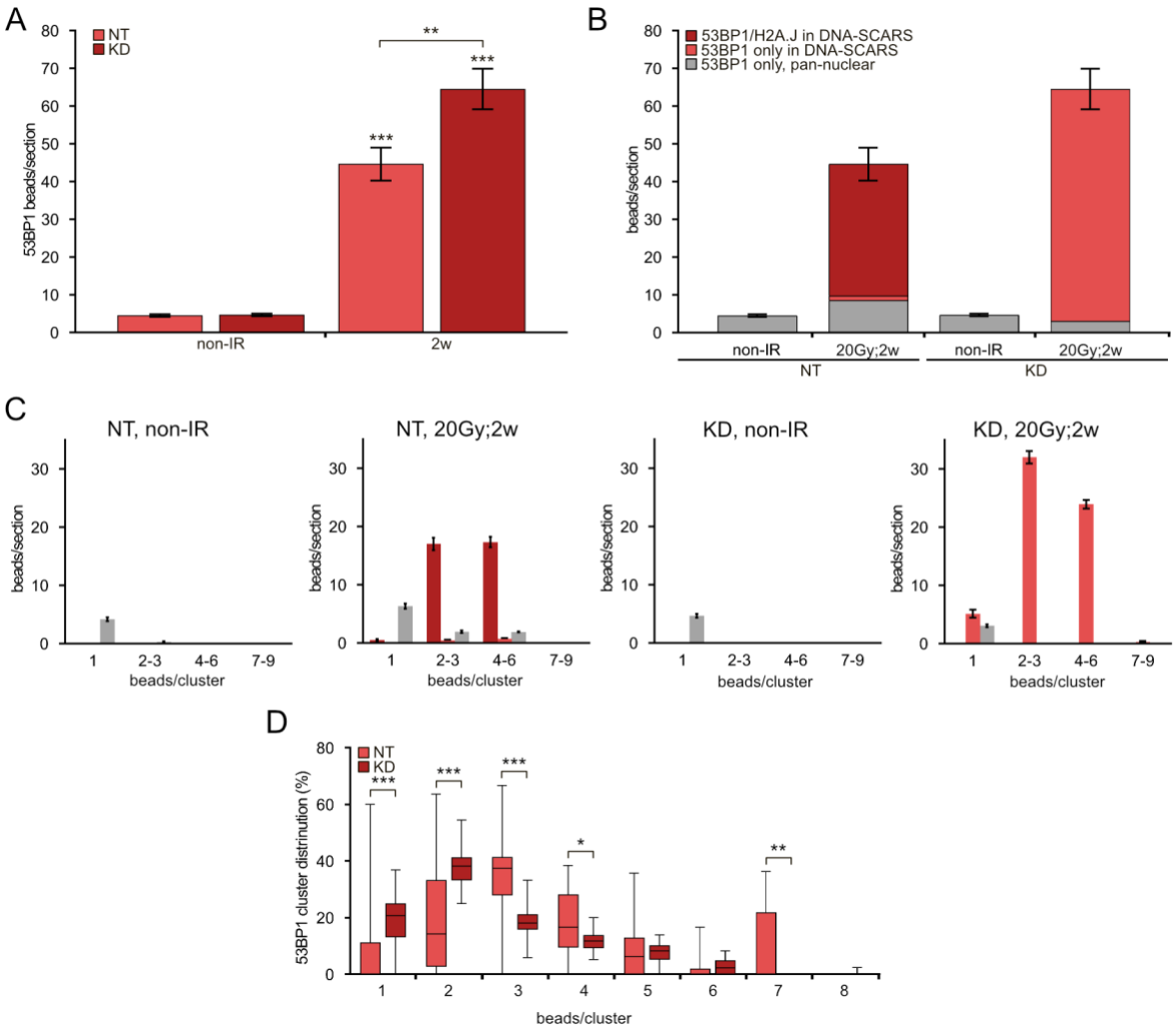

Figure 26. TEM quantification and localization analysis of 53BP1 in the context of DNA-SCARS and H2A.J in non-IR and 20Gy;2w IR NT and KD fibroblasts.
(A) Quantification of total 53BP1 beads/section (B) 53BP1 beads classified into chromatin localization based on pan-nuclear 53BP1, 53BP1 only located within DNA-SCARS and 53BP1 co-localizing with H2A.J within DNA-SCARS. (C) Bead cluster analysis of 53BP1 in context of chromatin localization based on pan-nuclear 53BP1, 53BP1 only located within DNA-SCARS and 53BP1 co-localizing with H2A.J within DNA-SCARS. D) Prevalence of 53BP1 cluster sizes within DNA-SCARS. Data in A and B presented as mean of 53BP1-labelling gold bead quantification within 25 nuclear sections ± SEM. Data in C and D shown as box plot with median, upper/lower quartiles and minimum/maximum values, n=25 nuclear sections. Significant statistical difference * (p <0.05), ** (p<0.01), *** (p<0.001). TEM staining and raw data provided by Dr.rer.med. Y.Lorat.

KD fibroblast show an even greater fold increase of ~13-fold in non-irradiated compared to 20Gy irradiated fibroblasts 2w post-IR (64.6 ±5.4 beads/section, p<0.0001). The 53BP1 level in non-irradiated samples shows no significant difference between NT and KD cell lines, however, the 53BP1 level in irradiated KD fibroblasts is significantly higher than that in irradiated NT cells (NT; 44.68 ±4.4 beads/section, KD; 64.6 ±5.4 beads/section, p=0.0063). With regards to 53BP1 distribution (Figure 26B), as with H2A.J, 100% of 53BP1 in non-irradiated samples is pan-nuclear. Similarly, the majority of 53BP1 found in irradiated senescent fibroblasts accumulates in DNA-SCARS (NT; ~80% KD; ~95%). The cluster accumulation pattern of 53BP1 beads (Figure 26C) again mirrors that of H2A.J, with pan-nuclear 53BP1 being prevalently single beads and DNA-SCARS-associated beads being

mostly in larger cluster between 3-8 beads per cluster, however, results indicate a disparity between NT and KD cell lines after irradiation. This disparity was further accentuated when regarding cluster size prevalence of 53BP1 beads within DNA-SCARS (Figure 26D). In irradiated NT fibroblasts approximately 27% of clusters fall in the categories of 1-2 beads per cluster. In irradiated KD fibroblasts, however, this prevalence more than doubles with the majority of clusters sized between 1-2 beads per cluster (~59%). Comparing the different cluster sizes shows a significantly larger percentage of 1 bead (NT; mdn=0.0%, KD; mdn=20.7%, U=98, p<0.0001) and 2 bead (NT; mdn=14.3%, KD; mdn=38.2%, U=127.5, p=0.0002) cluster in KD versus NT cells. The inverse can be seen in larger cluster sizes, where the majority of 53BP1 beads for NT fibroblasts are present in clusters of 3 or more beads (NT: ~73%, KD; ~41%). Statistically significant prevalence of larger 53BP1 can be seen for clusters containing 3 beads (NT; mdn=37.5%, KD; mdn=18.9%, U=77, p<0.0001), 4 beads (NT; mdn=16.7%, KD; mdn=11.8%, U=196.5, p<0.023) and 7 beads (NT; mdn=0%, KD; mdn=0%, U=200, p=0.0016).

6.14 H2A.J accumulates in human epidermis during skin ageing

To this point all experiments have been done *in vitro* to gain a mechanistic insight into the workings of H2A.J on a cellular level. Given the nature of cellular senescence and its potential effects on the surrounding tissue environment, foundational *in vivo* experiments were also undertaken to help investigate potential biological relevance of H2A.J accumulation. H2A.J positive cells and 53BP1 positive cells were quantified in the human epidermis (Figure 27). No significant increase in age-associated 53BP1 foci was observed between the youngest age-group (20-30 years; 4.5 ±0.5% 53BP1 positive cells) to the middle age group (31-60 years; 4.41 ±0.5% 53BP1 positive cells) however a slight increase could be seen in 53BP1/H2A.J double-positive cells (20-30 years; 3.08 ±0.3% double positive cells, 31-60 years; 3.75 ±0.4% double positive cells) with increasing age. Significant increase in 53BP1 positive cells however were observed when comparing the two younger age groups to 61-90 year old age group where 53BP1 positive cells increased up to 13.3 ±1.2% and double-positive cells to 10.63 ±1.1%. H2A.J cells increased consistently with age with a significant increase in H2A.J positive cells being observed from 20-30 years old (12.65 ±0.7% H2A.J positive cells) to 31-60 year old (33.4% ±2.7 H2A.J positive cells) age groups (p=0.0004). Similar H2A.J positive cells increased further from 31-60 year old (33.4% ±2.7 H2A.J positive cells) to 61-90 year old age group (p=0.0013).

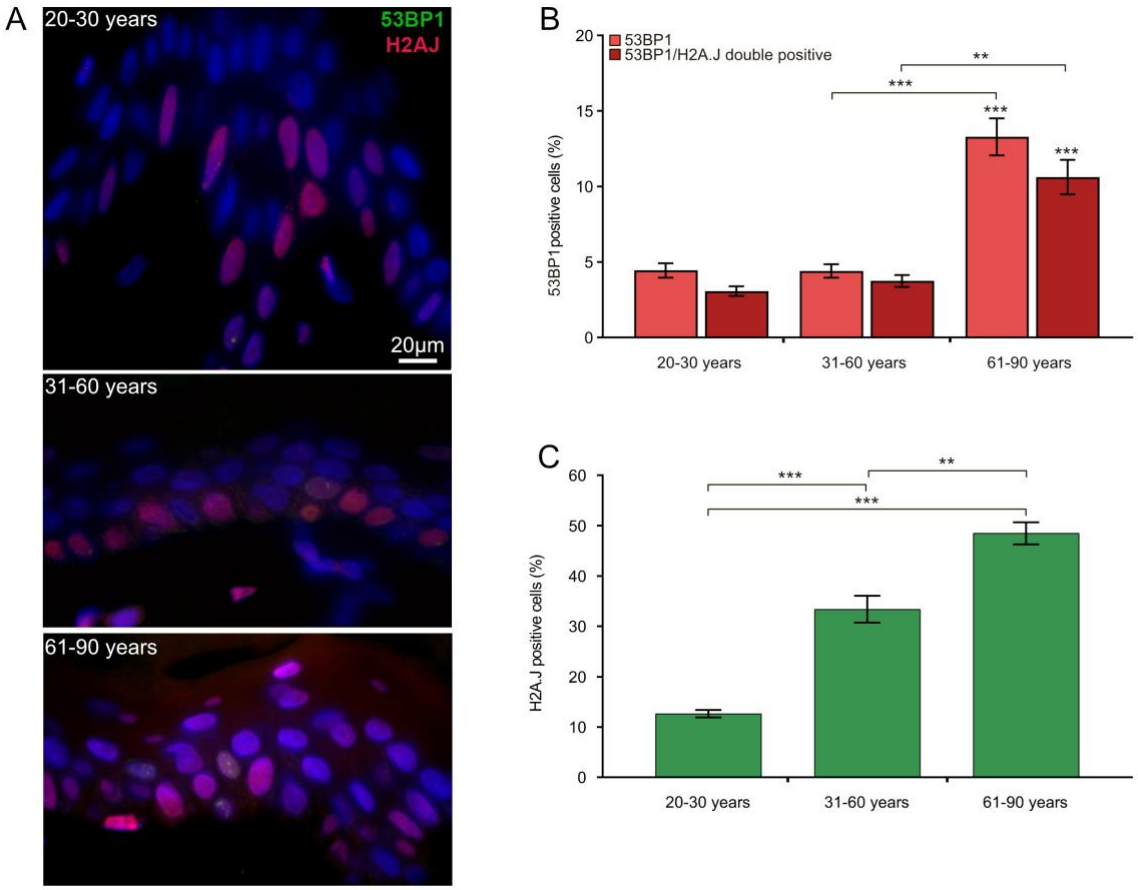

Figure 27. H2A.J accumulation in ageing human skin with increasing 53BP1
(A) IFM micrograph of human skin in varying age categories stained with 53BP1 and H2A.J. (B) Quantification of age-associated 53BP1 foci-positive cells in human epidermis. (C) Quantification of age-associated H2A.J accumulation in human epidermis. Data is presented as mean of 3 biological replicates and 2 technical replicates ± SEM. Significant statistical difference * (p <0.05), ** (p<0.01), *** (p<0.001) compared to 20-30 year age group unless otherwise indicated.

6.15 H2A.J in accumulates in human epidermis following *ex vivo* irradiation

10Gy *ex vivo* irradiation was undertaken on biopsies of human epidermis to determine whether premature H2A.J can be induced in tissue, as well as, *in vitro* cell culture (Figure 28). IR-induced DNA damage foci marked by 53BP1 were quantified at various time points following irradiation and compared to non-irradiated samples from the same patient which were fixated simultaneously. DNA damage repair proceeded as expected with the greatest amount of 53BP1 foci present at the earliest time point post-IR (0.5h; 3.1 ±0.3 foci/cell) and continuously decreasing with increasing time post-IR (5h; 2.4 ±0.1 foci/cell, 24h; 2.2 ±0.2 foci/cell, 48h; 1.03 ±0.2 foci/cell). Statistically significant reduction in 53BP1 foci was seen between 0.5h and 24h post-IR (p=0.045), as well as, between 0.5h and 48h post-IR (p=0.0043). Irradiated samples displayed higher 53BP1 foci values for all time points post-IR, with highly significant values seen at 0.5h (10Gy; 3.1 ± 0.3 foci/cell, non-IR; 0.16 ± 0.02 foci/cell, p=0.0098), 5h (10Gy; 2.4 ±0.1 foci/cell, non-IR; 0.3 ±0.1 foci/cell, p<0.0001) and 24h (10Gy; 2.2 ±0.2 foci/cell, non-IR; 0.5 ±0.1 foci/cell, p=0.0018). 48h post-IR the number

of 53BP1 foci was still higher than in non-IR samples (10Gy; 1.03 ±0.2 foci/cell, non-IR; 0.6 ±0.2 foci/cell), however, the difference was not statistically significant. IR-induced H2A.J accumulation was assessed by quantifying H2A.J positive cells at the same time points and conditions (Figure 28C). H2A.J positive cells increased for all time points post-IR in comparison to non-irradiated samples with significant differences observed at 0.5h (10Gy; 63 ± 0.7%, non-IR; 52 ±3.7%, p=0.040) and 48h (10Gy; 74 ±0.8%, non-IR; 60 ±0.8%, p=0.0004). A statistically significant increase in H2A.J positive cells was also observed between 10Gy; 0.5h and 10Gy; 48h (0.5h; 63 ± 0.7%, 48h; 74 ±0.8%, p=0.0006), with 48h showing the overall highest level of H2A.J positive cells of all conditions and time points.

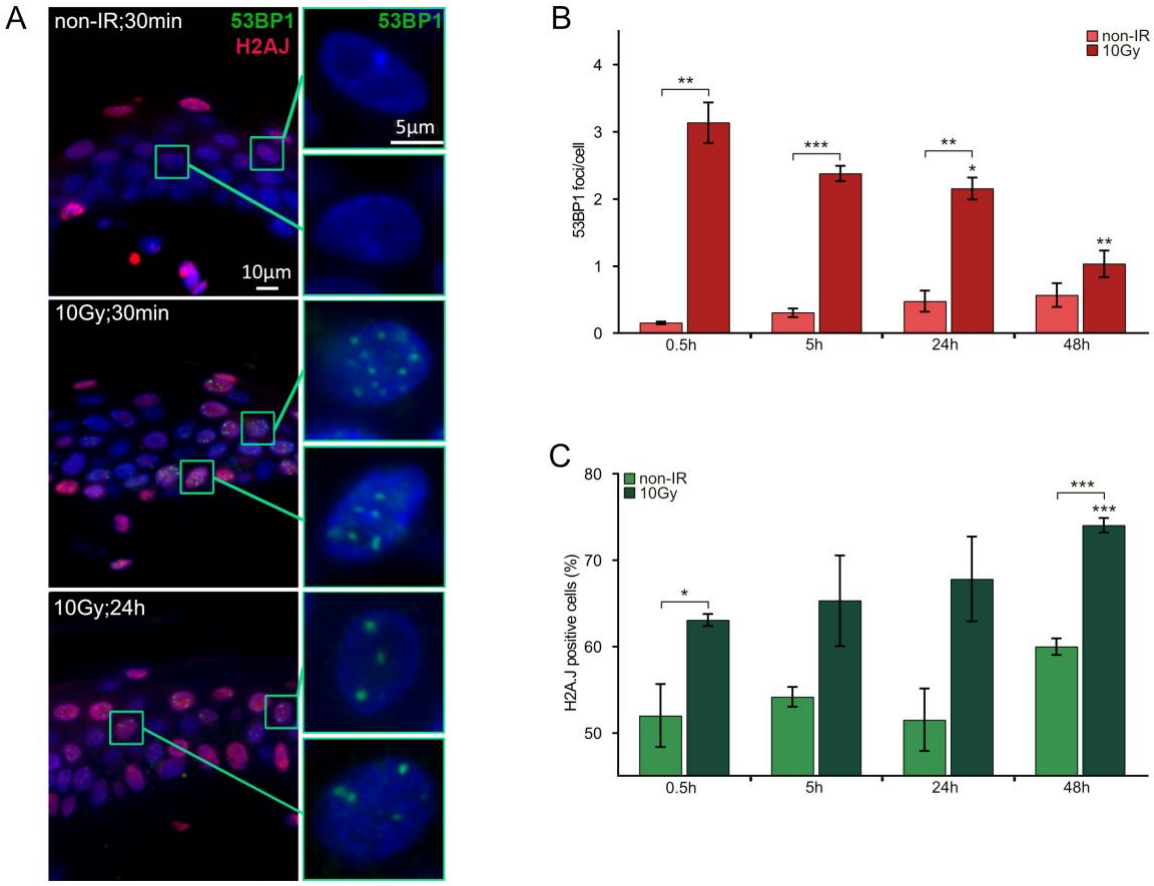

Figure 28. 53BP1 and H2A.J accumulation in 10Gy ex-vivo irradiated human epidermis
(A) IFM micrograph of 61 year old human epidermis stained for 53BP1 (green) and H2A.J (red) in non-irradiated sample and in 10Gy irradiated sample 0.5h and 24h following exposure. Green boxes mark magnified areas to highlight 53BP1 foci. (B) Quantification of 53BP1 foci in 61 year old human epidermis following 10Gy ex-vivo irradiation 0.5h, 5h, 24h, and 48h post-IR compared to a non-irradiated control sample fixated at the same time point. (C) Quantification of H2A.J positive cells in 61- year old human epidermis following 10Gy ex-vivo radiation 0.5h, 5h, 24h, and 48h post-IR compared to a non-irradiated control. Data is presented as mean of 3 technical replicates ± SEM. Significant statistical difference * ($p < 0.05$), ** ($p<0.01$), *** ($p<0.001$) compared to 0.5h time point of matching condition unless otherwise indicated.

6.16 Long term effects of low-dose fractionated radiation on H2A.J accumulation in murine interfollicular epidermis.

Following the results of singular high dose on H2A.J accumulation in human epidermis, fractionated irradiation with low doses (0.1Gy) was examined *in vivo* in murine interfollicular epidermis comparing H2A.J positive cells in 20x 0.1Gy IR mice to non-irradiated age-matched control, as well as, aged 18 month old mice (Figure 29).

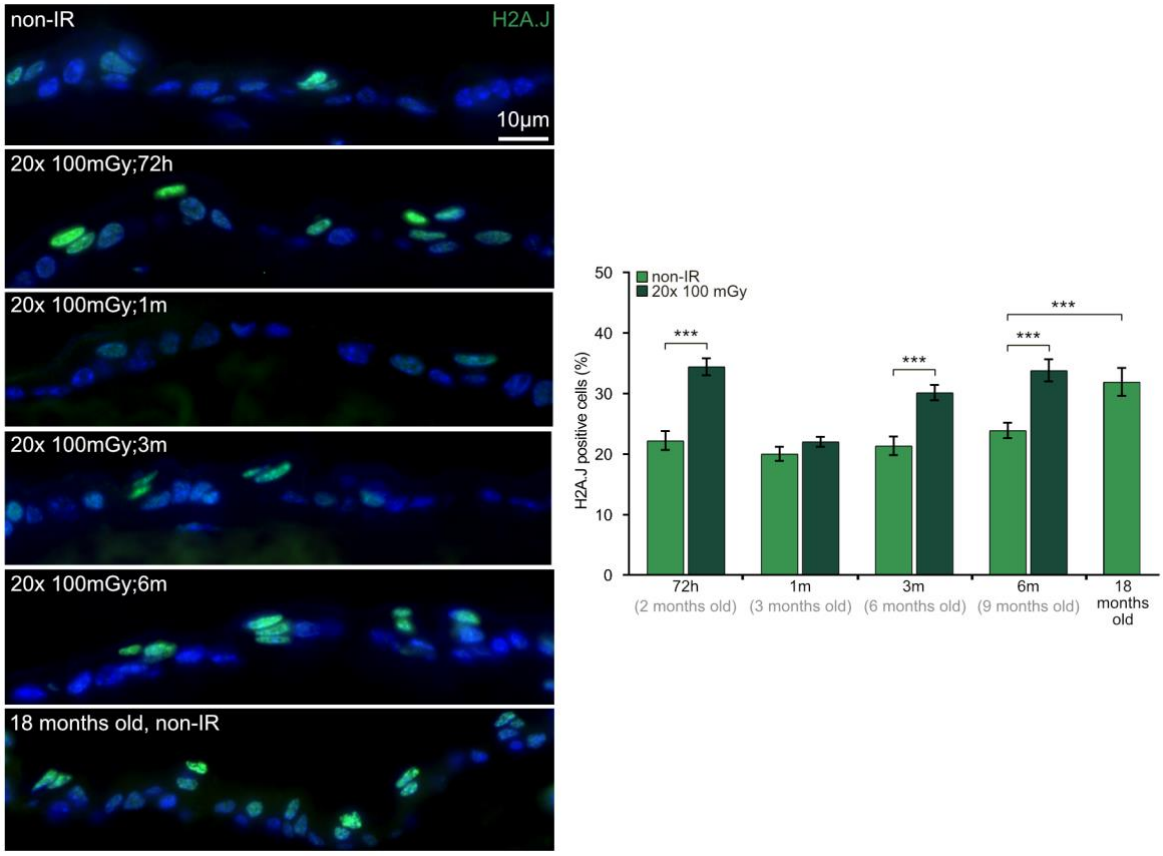

Figure 29. Short- and long term H2A.J accumulation in interfollicular murine epidermis following fractionated 0.1Gy low-dose IR.
IFM micrograph and quantification of H2A.J positive cells (green) in adult interfollicular murine epidermis 72h, 1m, 3m and 6m following completion of 20x 0.1Gy fractionated radiation compared non-irradiated age-matched controls and 18 month old aged mouse. Data shown as mean of 3 biological replicates and 4 technical replicates ±SEM. Significant statistical difference * ($p < 0.05$), ** ($p < 0.01$), *** ($p < 0.001$) compared to age-matched control.

Low-dose fractionated IR caused increased H2A.J positivity 72h (IR; 34 ±1.4%, non-IR; 22 ±1.6%, $p<0.0001$), 3 months (IR; 30 ± 1.3%, non-IR; 21% ±1.5, $p=0.0002$) and 6 months (IR; 34 ±1.8%, non-IR; 24 ± 1.3%, $p= 0.0002$) post-IR. The exceptional time point was 1 month post-IR where no statistically significant different was observed in H2A.J positive cells (IR; 22 ±1.1%, non-IR; 20 ±1.1%) and the increase in H2A.J positive cells, in general, was the lowest of all time points post-IR. As previously observed by Contrepois et al, H2A.J positive cells were also seen to rise with age. No great difference was seen between the ages of 2 months (22 ±1.6%), 3 months (20 ±1.1%) and 6 months (21 ±1.5%) of age. A slight, if non-statistically significant increase in H2A.J positive cells was observed at 9 months of age (24

±1.8%). 18 month old mice showed the greatest amount of H2A.J positive cells, which was significantly higher still than 9 month old (18 month old; 32 ±2.2%, 9 month old; 24 ±1.8%, p=0.0075). Notably, all irradiated samples except 1 month post-IR showed similarly high, if not higher (72h and 6 months post-IR), values in H2A.J positive cells compared to 18 month old aged mice.

7 Discussion

As a novel histone variant, limited publications exist examining H2A.J on a protein level. The first major breakthrough came in an observation that H2A.J accumulates in replicative- and ETO-induced senescence (Contrepois et al., 2017). ETO, a widely used chemotherapy drug, acts by binding to topo II/DNA complex at replication forks preventing DNA strand re-ligation leading to formation of DSBs (Chen et al., 2013; Pommier et al., 2010). However, unlike the radiomimetic drug bleomycin or topoisomerase II inhibitor ICRF-193, ETO has an additional, functional influence on the organization of replication proteins at replication loci during S-phase (Rossi et al., 2006). This appended reorganization results in dispersion of replication factories, formation of large RPA-positive nuclear foci and altered phosphorylation patterns of replication proteins (Montecucco et al., 2001; Rossi et al., 2002) thus highlighting that formation, structure and consequences of all DSBs are far from identical. The most detrimental and therapeutically relevant consequence of IR is the formation of DSBs, with 1Gy X-ray creating 16-40 DSBs per cell (Ward, 1988). Although DSB repair following IR has been thoroughly studied and documented, new elements are continuously coming to light. Therefore, following the observation that H2A.J accumulates *in vitro* following exposure to the DSB-inducing agent, ETO, and indications that H2A.J accumulates *in vivo* in murine epidermis/hair follicle following 50 fractions of 0.1Gy irradiation (Contrepois et al., 2017), we set to further elucidate the role of H2A.J following DSB-inducing ionizing radiation.

7.1 Acute H2A.J accumulation following irradiation

Using a onetime standard dose of 2Gy, the effect of IR on H2A.J was observed in a timeframe where acute DNA damage response occurs and is completed (section 6.1). 53BP1 was utilised as a marker for IR-induced DSBs and showed classic repair kinetics with a rapid response directly after exposure and continuous DNA-damage foci decline visible by 5h post-IR (Bekker-Jensen et al., 2005). In contrast, H2A.J accumulation steadily rose after exposure and peaked 24h post-IR with ~26% of both WT and NT fibroblasts positive for pan-nuclear H2A.J staining. Thus acute H2A.J accumulation appears to be a delayed response to IR compared to the swift initiation of DDR (Luijsterburg et al., 2010). This gradual increase could be due to H2A.J playing a potential role in the transient cell cycle arrest associated with an actively repairing-DDR. The decline of H2A.J 48h post-IR further supports this interpretation as at this time point, cells with successfully repaired DNA-damage would be re-entering the cell cycle thereby reducing the percentage of H2A.J positive cells (Jackson, Bartek, 2009). Regardless of the function of H2A.J, accretion of positive cells was proven to be dose-dependent 24h post-IR with the highest dose causing the highest level of H2A.J positive fibroblasts. Additionally, varying doses evoked altered aggregation kinetics. Markedly, following high doses (10Gy and 20Gy), H2A.J accumulation continued to rise 48h post -IR

instead of declining as with a relatively low dose (2Gy). A prolonged DDR after higher doses, reflected through greater 53BP1 foci levels 24- and 48h post-IR, may be causally linked to continuing H2A.J increase. If DDR signalling persists after IR, a shift occurs in which cell-cycle inhibitor expression rises and $p16^{INK4a}$ is upregulated with a downstream consequence of senescence-associated permanent growth arrest (Campisi, d'Adda di Fagagna, 2007; d'Adda di Fagagna, 2008; Fumagalli et al., 2012; Kim et al., 2014). As H2A.J accumulation persists and increases 48h post high dose IR, in which there is evidence of prolonged DDR signalling, it could be postulated that H2A.J may potentially play a role in, or be a consequence of, this shift from acute to persistent DDR signalling.

7.2 H2A.J does not play a crucial role in DSB repair by NHEJ

As previously discussed, accessibility of DNA damage, and thus efficiency and swiftness of DNA damage repair is, in part, dictated by surrounding chromatin structure. The hallmark covalent histone modification associated with DSB repair is phosphorylation of histone H2AX at serine 139 by ATR, ATM and DNA-PKcs (Falck et al., 2005; O'Driscoll et al., 2003; Rogakou et al., 1998). H2AX is incorporated into 5-25% of histone octamers and phosphorylation in response to IR reaches across megabases, visible as microscopic *ionizing radiation-induced foci* (IRIF) (Rogakou et al., 1999), suggesting large scale chromatin remodelling around the DSBs. Other chromatin remodelling activities have also been linked to DSB repair including cell-cycle signalling involvement of H4K20 and H3K79 methylation through 53BP1/CRB2 (*DNA repair protein crb2*) recruitment to IRIF (Botuyan et al., 2006; Du et al., 2006; Huyen et al., 2004; Kim et al., 2006; Sanders et al., 2004) and release of heterochromatin-associated *KAP-associated protein 1* (KAP1) from compacted chromatin areas surrounding DSBs (Goodarzi et al., 2008). Therefore, considering all of the above and observations of acute H2A.J accumulation post-IR, the next logical step was to examine whether H2A.J had an effect on DSB repair following IR (section 6.4). NT and H2A.J knock-down KD fibroblasts irradiated with 20Gy showed similar repair efficiencies for all time points except 48h post-IR. At this time point NT cells showed slightly higher 53BP1 foci levels than KD cells, however, it can be argued that at 48h post-20Gy IR we are no longer moving within the realm of acute DDR but traversing into persisting DDR foci. In conclusion, it could be said that H2A.J does not function in a similar fashion to γH2AX and does not play a pivotal role in acute DSB repair following high IR doses. γH2AX is important for cell-cycle checkpoint signalling following low doses but is nonessential following higher IR doses (Celeste et al., 2002; Fernandez-Capetillo et al., 2002). Taken together with observations regarding altered H2A.J kinetics following higher doses, it could be postulated that H2A.J takes over from

γH2AX with regards to cell cycle signalling in the case of high DSB levels with potential formation of persistent DSBs.

7.3 Long-term H2A.J accumulation following 20Gy IR

Pursuing H2A.J accumulation past time points of acute DDR to 1w and 2w post-IR revealed a continuous increase of H2A.J positive cells in NT fibroblasts coupled with persistent DNA damage foci-positive cells marked by 53BP1. KD cells revealed drastically diminished H2A.J positivity, however, with similar levels of 53BP1 positive cells. Post-IR H2A.J increase did not seem toxin specific as ETO exposure also induced increase in H2A.J positive cells. However, overall H2A.J and 53BP1 levels were lower compared to IR. This could potentially be due to the different mechanisms through which IR and ETO induce DNA damage (Chan, 2006; Chen et al., 2013; Montecucco et al., 2001; Pommier et al., 2010; Prise, O'Sullivan, 2009; Rossi et al., 2006; Rossi et al., 2002), however, additional targeted experiments would need to be performed to establish this.

7.4 H2A.J accumulates in IR-induced senescent fibroblasts but is not required for senescence induction or growth arrest

Persisting DDR foci, as observed above, can persist over years in culture and have been linked to stable cellular senescence, as well as IR-induced senescence (Aratani et al., 2018; Fumagalli et al., 2014; Sedelnikova et al., 2004). Additionally, higher IR doses (10-20Gy) are known to induce senescence in WI-38 fibroblasts specifically (Noren Hooten, Evans, 2017). Senescent state of NT and KD fibroblasts 2w post-20Gy IR was confirmed through SA-β-gal staining (Dimri et al., 1995), p21 accumulation (Yosef et al., 2017) and ki67 downregulation (Lawless et al., 2010). In the same population, H2A.J/SA-β-gal double-staining confirmed that H2A.J-positve cells corresponded to SA-β-gal positivity, and thus, H2A.J seems to accumulate in IR-induced senescent WI-38 fibroblasts. SA-β-gal, p21 and ki67 were also evaluated for KD cells but no discernable different was found with knock-down of H2A.J. Therefore, it stands to reason, that H2A.J accumulates in IR-induced senescent cells but is not essential for its induction. Additionally, H2A.J is not required for senescence-associated growth arrest as demonstrated by the proliferation marker ki67 as well as BrdU incorporation levels in both NT and KD fibroblasts.

7.5 Senescence-associated lamina decline

Decline of the lamina protein, lamine B1, is a well-documented senescent cell characteristic, which can also be used as a biomarker for senescence *in vitro* and *in vivo* (Dreesen et al., 2013b; Freund et al., 2012a; Wang et al., 2017). Regarding lamine B1 decline in replicative senescence associated with ageing, the connection between senescence and H2A.J was further supported. WI-38 WT fibroblasts, induced into replicative senescence through continuous culture, revealed a reduction in lamine B1 signal corresponding with increased H2A.J signal. This inverse relationship could also be demonstrated in young versus aged murine and human epidermis samples. Further *in vitro* studies with NT fibroblasts in IR-induced senescence revealed a similar negative relationship between lamine B1 decline and H2A.J positivity. However, H2A.J KD fibroblasts displayed a similar decline in lamine B1 signal intensity in non-IR versus IR-induced senescent KD fibroblasts. Nevertheless, DAPI-normalized signal intensities for lamine B1 unveiled significantly higher lamine B1 values in NT fibroblast in both non-IR controls and IR samples compared to KD cells. At this point it is to be noted, for the purpose of scientific integrity, this observation would need to be supported by further methods such as RT-qPCR and Western Blot. For discussions sake however, if this decrease in lamine B1 levels was in fact further validated, another avenue of investigation could be opened into H2A.J, the nuclear lamina, and its effect on the chromatin rearrangement associated with senescence. Hutchinson-Gilford Progeria Syndrome (HGPS) is a fatal premature ageing syndrome in children caused by a mutation in the lamin A/C gene (De Sandre-Giovannoli et al., 2003; Eriksson et al., 2003) which also exhibits decrease levels of lamine B1 (Clements et al., 2019). HGPS fibroblasts and keratinocytes display reduced H3K9me3 heterochromatin marks and do not form SAHF (Scaffidi, Misteli, 2006; Shumaker et al., 2006) even though they enter replicative senescence much earlier than WT counterparts (Cao et al., 2011). Additionally, nuclear lamina defects have been linked to inflammatory phenotype regulation to which, incidentally, H2A.J has also been associated with during ETO-induced senescence (Contrepois et al., 2017; Kristiani et al., 2020).

7.6 SAHF formation and nuclear enlargement

Despite the disparity of lamine B1 levels in NT and KD fibroblasts, H2A.J knock-down did not perturb SAHF formation in IR-induced senescence. SAHF were identified as large DAPI-dense globules within the nucleus and double-staining with H3K9me3/H3K27me3 confirmed that these corresponded to the heterochromatin cores of SAHF (Narita et al., 2003a). SAHF were also clearly identifiable utilising TEM and at this resolution no discernible difference in SAHF structure was identifiable either. Simultaneously, nuclear area was also measured

demonstrating IR-induced senescence-associated nuclear enlargement in both NT and KD fibroblasts, with KD fibroblasts demonstrating significantly larger nuclear areas. The causal and functional significance of this observation in relation to H2A.J however is difficult to assess, as the literature on senescence-associated nuclear/cellular enlargement is limited despite it being cited as one of the main characteristics of senescent cells. Early studies of WI-38 fibroblasts observed that increased size resulted in decreased replicative potential (Bemiller, Miller, 1979; Mitsui, Schneider, 1976), which was later argued as a possible mechanism fundamental to senescence (Angello et al., 1989). *In vivo*, increased cell size was also associated with senescence (Biran et al., 2017). Senescence-associated cell swelling is known to activate cell signalling through mechano transduction and the closely related nuclear swelling has also been linked to cytoskeletal networks (Gruenbaum et al., 2005). Additionally, it has been shown that induced nuclear swelling can alter gene expression (Dahl et al., 2005) and that senescence-associated nuclear swelling is mediated by *mitogen-activated protein* (MAP) kinases (Kobayashi et al., 2008). These MAP kinase signalling pathways could be a possible mechanism through which H2A.J effects nuclear morphology. However, MAP kinase signalling pathways are complex, interlinked and function across all levels of cellular mechanisms rendering it difficult to hypothesise how a lack of H2A.J could elicit an effect. Chromatin alteration through knock-down of H2A.J could influence MAP kinase target proteins, regulators and translocation factors to name but a few, all of which could have a knock-on effect on the normal regulation of senescence-associated nuclear swelling (Kobayashi et al., 2008; Zou et al., 2019).

7.7 H2A.J promotes inflammatory gene expression in IR-induced senescence.

The SASP is a complex and diverse phenotype influenced by cell type and senescence-inducing stimuli. Focus was placed on four SASP factors which showed the highest fold change in secreted protein levels in WI-38 fibroblasts in replicative senescence, OIS, high-dose X-ray induced senescence and bleomycin treatment-induced senescence (Acosta et al., 2008; Bavik et al., 2006; Coppé et al., 2008; Freund et al., 2010; Liu, Hornsby, 2007; Rodier et al., 2009). An increased abundance of RNA encoding IL6, CXCL8, CSF2 and CCL2 in IR-induced senescent NT fibroblasts compared to proliferating counterparts was demonstrated corresponding to previous publications using WT WI-38 (Coppé et al., 2008; Rodier et al., 2009). H2A.J knock-down abolished RNA abundance for these SASP factors in IR-induced senescent cells. Effect of down regulation on cytokine secretion was assessed through targeted cytokine measurements in conditioned media, and demonstrated a severe impact of H2A.J knock-down induced SASP RNA depletion on IL6, CXCL8 (IL8), GM-CSF (CSF2) and MCP1 (CCL2) secretion. Taken together, these observations align with those of

the ETO-induced senescence studies conducted by Contrepois et al. They suggest that H2A.J accumulates in DNA damage-induced senescent cells regardless of inducing toxin and H2A.J involvement occurs downstream of the DDR and not at earlier stages of initiation.

7.8 H2A.J preferentially localizes to IR-induced DNA-SCARS

An altered SASP, in particular down-regulated IL6, has been shown to not only effect paracrine signaling and autocrine senescence-phenotype maintenance, but also effects SAHF formation within OIS fibroblasts (Kuilman et al., 2008). Although the overall formation of SAHF was not visibly effected by H2A.J knockdown we speculated on a potential connection between H2A.J and another structural component of senescent cells; DNA-SCARS (Rodier et al., 2011a). DNA-SCARS do not co-localize directly with PML-NBs, as with γH2A.X and 53BP1 for example, but are found in close proximity to one another (Rodier et al., 2011b; Schultz et al., 2000). In accordance with previous publications, 53BP1 and PML-NB association increased by 24h post 20Gy IR in NT and KD fibroblasts, with H2A.J not influencing this association. By 2w post-IR, levels of 53BP1/PML-NB association lay above 80% for all 53BP1 foci, identifying these persistent 53BP1 foci as DNA-SCARS. PML-NBs can be both constitutive, as well as, transient and are known to increase in number in response to IR-induced DNA-damage (Carbone et al., 2002). NT and KD PML-NB numbers rose significantly following 20Gy IR with the highest values reached in senescent cells 2w post-IR. Therefore, H2A.J depletion did not seem to effect stress-response function of PML-NBs post-IR. These observations are also in line with previous results (ki67, SA-β-gal, p21), as PML is implicated in regulation of cell-cycle arrest and senescence induction (Carbone et al., 2002; Ferbeyre et al., 2000), neither of which were effected by H2A.J knock-down.

While the association between DNA-SCARS and PML-NB may not be influenced by H2A.J, structural significance of H2A.J in DNA-SCARS formation has yet to be investigated. Another H2A variant, histone H2A.X, is a structurally essential component for DNA-SCARS enforcing their stability, therefore a potential role for H2A.J may also be plausible. Reduced DNA-SCARS stability due to H2A.X depletion, altered IR-induced senescence-associated growth arrest, as well as, down regulating expression of SASP member, IL-6 (Rodier et al., 2011b). Similar effects on SASP were also proven following H2A.J knock-down, with exception of growth arrest. The most efficient method for investigating functionality of H2A.J in DNA-SCARS stability, was application of a 24h BrdU pulse on NT and KD fibroblasts 2w post-20Gy IR, to determine DNA synthesis level. Unlike H2A.X however, H2A.J did not seem to play a critical role in DNA-SCARS stability, as no increase in BrdU incorporation was witnessed in KD fibroblasts versus NT fibroblasts in IR-induced senescent cells.

Although γH2A.X can be clearly visualized as foci in DNA-SCARS, H2A.J association with DNA-SCARS was more difficult to examine, as IFM staining manifests as a pan-nuclear signal. This obstacle was overcome with implementation of a proximity ligation assay between H2A.J and 53BP1 marking DNA-SCARS. A baseline level of ~6 PLA foci was observed in non-IR NT fibroblasts likely due to low-level H2A.J present in non-senescent cells (Contrepois et al., 2017) coincidentally reacting with 53BP1, responsible for diffuse IFM signal in non-treated cells which later rearranges to IR-induced 53BP1 foci (Bekker-Jensen et al., 2005; Schultz et al., 2000).

The high resolution of TEM was utilized by Dr.rer.med. Yvonne Lorat to further investigate association between H2A.J and DNA-SCARS by quantifying H2A.J labelled with gold beads in relation to DNA-SCARS, and within the chromatin context. Data analysis revealed bead numbers which supported previous observations verifying low-level H2A.J presence in non-IR controls and a drastic increase 2w after 20Gy irradiation. A new insight into H2A.J distribution was gained with regards to localization. Double-staining for H2A.J and 53BP1 not only supported the results of PLA, showing that H2A.J localizes to DNA-SCARS, but also highlighted that in IR-induced senescent NT fibroblasts, the majority of H2A.J is found within DNA-SCARS and the remaining fraction is scattered throughout the nucleus. Therefore the majority of H2A.J localized to a minimal area occupied by DNA-SCARS (~3%). An additional indication that H2A.J may play a significant role in DNA-SCARS functionality or formation is reflected in the bead cluster analysis. Pan nuclear H2A.J was found to present itself mostly as single beads whereas DNA-SCARS-associated H2A.J predominantly formed larger clusters ranging between 4 and 13 beads per cluster. This abundance of H2A.J may therefore induce chromatin alterations ultimately influencing structure and functionality of DNA-SCARS such as those seen in SASP analysis. The preferential localization of H2A.J may also explain why we see continual increase of H2A.J 24h-48h post-IR following high doses. The H2A.J may be accumulating at DNA-SCARS when the shift from acute DDR foci to DNA-SCARS occurred, which is reflected in PML-NB association with 53BP1.

7.9 H2A.J impacts 53BP1 accumulation at DNA-SCARS

Amongst others, DNA-SCARS contain activated ATM, activated CHK2, MDC1 (d'Adda di Fagagna, 2008; Herbig et al., 2004; Rodier et al., 2009; Rodier et al., 2011a). H2A.X depletion effected the downstream assembly of CHK2 and MDC1 at DNA-SCARS, thereby influencing the senescence-induced growth arrest (Rodier et al., 2011a), but did not affect 53BP1, another major component of DNA-SCARS. Formation of DNA-SCARS also did not depend on ATM, ATR, Artemis, BLM, NBS1 or PML-NBs (Rodier et al., 2011a). IFM investigations revealed that senescent H2A.J KD fibroblasts presented higher numbers of

DNA-SCARS but with reduced area compared to senescent NT counterparts. Additionally, TEM analysis revealed higher number overall of 53BP1 gold beads in senescent KD fibroblasts compared to senescent NT fibroblasts. The higher resolution of TEM also supported the crude measurement data of IFM and revealed that 53BP1 accumulated in DNA-SCARS in smaller, but more numerous, bead clusters in senescent KD cells versus NT cells. Therefore it could be postulated that H2A.J may have an influence on the ultra-structure of DNA-SCARS, which in turn, influences the SASP. Perturbed 53BP1 accumulation could affect downstream DDR mediator kinase CHK2, inversely H2A.J knock-down could also influence upstream kinases such as ATM or DNA-damage sensor NBS1, all of which are known to be essential for regular SASP induction (Rodier et al., 2009; Rodier et al., 2011a).

7.10 Potential mechanistic consequences of H2A.J incorporation at DNA-SCARS

To date, only two papers have been published investigating H2A.J at protein level (Contrepois et al., 2017; Tanaka et al., 2020), thus conceiving a theory of how its incorporation effects SASP expression is challenging. Targeted ChIP experiments only added to this difficulty by revealing that H2A.J is not differentially deposited at promoters of genes regulated by H2A.J versus those who are not effected by its knock-down (Contrepois et al., 2017). Additionally, ChIP-seq experiments revealed that H2A.J was not deposited at discrete genomic locations and its distribution closely mirrored that of canonical H2A in senescent cells (Contrepois et al., 2017). Preferential accumulation of H2A.J at DNA-SCARS demonstrated in this study, gives a primary indication of potential mechanism of influence pointing to a spatiotemporal significance of H2A.J deposition and a potential interaction between other H2A.J containing nucleosomes or other nucleosomes in general. ChIP-Seq revealed additional cross-correlation peaks for di-,tri- and tetra-nucleosomes compared to H2A, revealing that H2A.J protected cross-linked chromatin from sonication (Contrepois et al., 2017). Studies into the biochemical properties of the H2A.J-containing nucleosome versus H2A-containing nucleosome also revealed an increased thermostability of the H2A.J nucleosome, however, the functional significance of this is yet unknown (Tanaka et al., 2020). Taken together, one could postulate that an abundance of H2A.J localized to one specific region creates the functional affect associated with its deposition in senescent cells.

While the C-terminal tail may not be significant in the thermostability of the H2A.J nucleosome, it is essential for SASP induction and the presence of the SQ binding motif further supports this (Contrepois et al., 2017; Tanaka et al., 2020). H2A.J-induced chromatin alterations may thus be influenced by transaction factor binding to the C-terminal. Alternatively, chromatin rearrangement could result from *cis* or *trans* actions of PTMs of the

C-terminal tail. Little is known about PTMs of H2A.J, but, unpublished data (Carl Mann) has shown phosphorylation of H2A.J at Serine 123 following extremely high doses of 50Gy. Potential C-terminal PTMs could then initiate a causal sequence on PTMs of histone tails in an intra- or internucleosomal manner (Kouzarides, 2007). Additionally, the valine/alanine substitution at position 11 unique to H2A.J could also act as a binding site for transaction factors in turn influencing gene expression.

The alternated 53BP1 accumulation at DNA-SCARS mediated through H2A.J could potentially stem from chromatin alterations which block/hinder classic 53BP1 binding. The center of 53BP1 contains a nuclear localization signal and tandem Tudor domains facilitating binding to constitutive histone modification H4K20me2 (Botuyan et al., 2006; Huyen et al., 2004). Additionally, an ubiquitin-dependent recruitment motif is present that recognizes DNA-damage-induced H2A(X) ubiquitinylation at Lysine 15 (H2A(X)K15Ub), marking 53BP1 as a histone modification reader (Fradet-Turcotte et al., 2013; Mattiroli et al., 2012). This sequence of events has been demonstrated in acute DNA damage. Larger 53BP1 foci observed in DNA-SCARS may require additional chromatin rearrangement facilitated by H2A.J to allow for greater accumulation and proximal binding of 53BP1 and other DNA-damage repair proteins to DNA-SCARS. Additionally, upon histone binding, 53BP1 is hypothesized to act as a potential cross linker between adjacent nucleosomes resulting in further knock-on conformational changes (Fradet-Turcotte et al., 2013). Distortion of chromatin alterations induced by incorrect 53BP1 binding may thus lead to disruptions in binding/activation of downstream SASP-signaling pathway as observed in H2A.J knock-down fibroblasts.

7.11 Biological relevance of H2A.J

It has been observed that H2A.J accumulates in a tissue specific, age-dependent manner in brain, liver, kidney and in the epidermis of mice and humans (Contrepois et al., 2017). Investigation of aged human epidermis showed that H2A.J accumulation increased with increasing 53BP1 in an age-dependent manner. Remarkably, although H2A.J levels in 31-60 year old was almost twice as high as those observed in 20-30 year olds, 53BP1 levels had not risen in the same fashion. A potential explanation for these results could be the age category itself and the sex of the patients from which the samples were derived. While estrogen levels drop in both men and women with age, women experience a much steeper and earlier drop in estrogen levels when they undergo menopause (Labrie et al., 1997). Estrogen, in turn, has been shown to increase telomerase activity, thus reducing telomere shortening, and prevent senescence *in vitro* in leukocytes, endothelial progenitor cells and vascular smooth muscle cells (Aviv et al., 2006; Imanishi et al., 2005; Ling et al., 2006). In

this particular study, 3 biological replicates were obtained, 2 of which were females, both of which at menopausal age, linked to a rapid drop in estrogen and premature skin ageing compared to their male counterparts. Therefore, to assess the link between H2A.J and DNA damage *in vitro* it would be prudent to divide the 31-60 year old category into smaller groups (i.e. 31 to 40-, 41 to 50-,51 to 60 years of age) and take into account the sex of the patients also. In contrast to the younger two age groups however, 53BP1 foci increased significantly from 61-90 years of age although this age group showed the same female to male ratio as 31-60 year old group. This discrepancy, however, shows H2A.J as a potential biomarker for skin ageing as, *in vivo*, it does not accumulate solely in unison with 53BP1 levels between 31-60 years old, but may potentially mark ageing cells afflicted by other ageing mechanisms such as loss of proteiostasis, mitochondrial dysfunction or altered intercellular communication (Lopez-Otin et al., 2013).

10Gy *ex vivo* irradiation of human skin has shown that DNA-damage-inducing IR results in accumulation of H2A.J in the human epidermis at levels greater than those seen in age-dependent H2A.J accumulation. Even *in vivo* studies of murine epidermis fractionally irradiated with low doses of 20x 0.1Gy to mimic non-targeted doses facing surrounding tissue during radiotherapy, showed increased H2A.J accumulation with lasting impacts up to 6 months post-IR, matching the levels seen in aged murine interfollicular epidermis. The SASP microenvironment created by increased senescent cells within tissue has long since been implicated as a critical effector within skin ageing, tumour suppression and progression (Campisi et al., 2011; Ghosh, Capell, 2016; Saleh et al., 2019). A critical question in this instance would be whether this *in vivo* accumulation is accompanied by the SASP we demonstrated in *in vitro* studies of irradiated lung fibroblasts, and, if so, can it be abated through H2A.J knock-down? Of course the SASP could be modulated through senolytics which block senescence entirely or remove senescent cells completely, however this could impair critical effects of senescence such as wound healing following tumour surgeory, chemotherapy or radiotherapy. (Demaria et al., 2014). H2A.J could thus be a potential target to reduce radiotherapy-induced senescent side effects by aborating SASP in a less disruptive manner than senolytics.

7.12 Conclusion

This study was the first of its kind into H2A.J following radiation and revealed radiation-induced H2A.J accumulation whose magnitude and persistence were both dose-dependent. The most notable consequence of H2A.J incorporation was seen in the SASP signalling, which was almost completely abolished with H2A.J knock-down. As SASP regulation is

reliant on DNA-SCARS formation, the increased H2A.J incorporation at these DNA-SCARS seemed all the more significant and the H2A.J-induced chromatin alterations effected 53BP1 accumulation at DNA-SCARS. This alteration in the ultrastructure DNA-SCARS due to H2A.J knock-down, may be the first indications as to how H2A.J is involved in the SASP expression. Elucidation of the role of histone variant H2A.J following irradiation has only just begun and this study serves as a foundation to future studies to further clarify its function and mechanisms of action.

7.13 Outlook

As H2A.J is poorly studied, there are boundless possibilities for future studies. To begin with a distinction would have to be made between acute, transient H2A.J accumulation and chronic, long-term H2A.J accumulation following IR. The impact of acute H2A.J accumulation is not yet known and the reason why some cells become H2A.J positive and others do not could be investigated. Additionally the effects of cell cycle phase on acute H2A.J accumulation could be investigated together with BrdU pulse-labelling to document whether H2A.J positive cells re-enter cell cycle progression or are halted until H2A.J is reduced.

As H2A.J is a major effector in SASP induction and, as the SASP is associated with most of the detrimental effects of senescent, this would be critical to investigate further. Future studies could focus on the pathway through which H2A.J effects SASP. Evaluations of upstream and downstream 53BP1 binding partners/effectors could pinpoint at which stage of the pathway H2A.J becomes relevant. Additionally, samples of NT, KD and H2A.J over expressing cells have been generated and will be analysed by Assay for Transposase-Accessible Chromatin using sequencing (ATAC-seq), which generates a library of open or accessible chromatin that can then be sequenced by qPCR or next generation sequencing. Mod-Spec®, applied to analyse whether H2A.J has an effect on prevalent histone modifications throughout the cell, is another high-throughput analysis currently under consideration as a future method. The same set of samples has also been sent for Mass Spectrometry analysis in co-operation with the laboratory of Simone Moertl at the Helmholtz center in Munich. All of these analysis will provide invaluable data which will aid in focusing future projects. Bystander senescence-induced by other cells following radiation has also been documented and it would be interesting to observe how the reduced SASP in H2A.J knock-down fibroblasts impacts neighboring cells.

Of unfathomable value are the H2A.J knock out mice which have been generated and gifted by Carl Mann. Here every organ offers another possibility with the question of how H2A.J accumulates in each organ. Also, what is the nature of the SASP in these mice? If it is

reduced, as with *in vitro* studies, what effect does this have on ageing and radiation-induced senescence. Would H2A.J knock out mice have altered radiosensitivty, reduced inflammation, quicker recovery or lower tumor re-growth rate? Contrarily, would these mice have higher senescent cell population due to reduced immuneclearance mitigated through an altered SASP? Focusing on the skin, it would be prudent to focus on the stem cells throughout age and after radiation, as these are also effected negatively by senescent cell accumulation and SASP. As senescence also plays a role in would healing and embryonic development, it would be prudent to characterize these mice in comparison to WT to gain insights into the role of H2A.J in development and wound healing.

The potential for H2A.J as a target for a radiotherapy-adjuvant drug target is upheld throughout this study. However, we are only just at the very beginning of understanding this histone variant and development of such a drug, if possible, lies in the distant future.

8 References

1. Abraham J, Mathew S (2019) Merkel Cells: A Collective Review of Current Concepts. Int J Appl Basic Med Res 9:9-13
2. Acosta JC, O'Loghlen A, Banito A, Guijarro MV, Augert A, Raguz S, Fumagalli M, Da Costa M, Brown C, Popov N, Takatsu Y, Melamed J, d'Adda di Fagagna F, Bernard D, Hernando E, Gil J (2008) Chemokine signaling via the CXCR2 receptor reinforces senescence. Cell 133:1006-1018
3. Adams PD (2007) Remodeling chromatin for senescence. Aging Cell 6:425-427
4. Angello JC, Pendergrass WR, Norwood TH, Prothero J (1989) Cell enlargement: one possible mechanism underlying cellular senescence. J Cell Physiol 140:288-294
5. Aratani S, Tagawa M, Nagasaka S, Sakai Y, Shimizu A, Tsuruoka S (2018) Radiation-induced premature cellular senescence involved in glomerular diseases in rats. Sci Rep 8:16812
6. Arents G, Moudrianakis EN (1995) The histone fold: a ubiquitous architectural motif utilized in DNA compaction and protein dimerization. Proc Natl Acad Sci U S A 92:11170-11174
7. Aviv A, Valdes A, Gardner JP, Swaminathan R, Kimura M, Spector TD (2006) Menopause modifies the association of leukocyte telomere length with insulin resistance and inflammation. J Clin Endocrinol Metab 91:635-640
8. Banchereau J, Steinman RM (1998) Dendritic cells and the control of immunity. Nature 392:245-252
9. Banito A, Lowe SW (2013) A new development in senescence. Cell 155:977-978
10. Barnum KJ, O'Connell MJ (2014) Cell Cycle Regulation by Checkpoints. Cell Cycle Control: Mechanisms and Protocols, 2nd Edition 1170:29-40
11. Bavik C, Coleman I, Dean JP, Knudsen B, Plymate S, Nelson PS (2006) The gene expression program of prostate fibroblast senescence modulates neoplastic epithelial cell proliferation through paracrine mechanisms. Cancer Res 66:794-802
12. Bekker-Jensen S, Lukas C, Melander F, Bartek J, Lukas J (2005) Dynamic assembly and sustained retention of 53BP1 at the sites of DNA damage are controlled by Mdc1/NFBD1. J Cell Biol 170:201-211
13. Bemiller PM, Miller JE (1979) Cytological changes senescing WI-38 cells: a statistical analysis. Mech Ageing Dev 10:1-15
14. Bennardo N, Cheng A, Huang N, Stark JM (2008) Alternative-NHEJ is a mechanistically distinct pathway of mammalian chromosome break repair. PLoS Genet 4:e1000110
15. Betermier M, Bertrand P, Lopez BS (2014) Is non-homologous end-joining really an inherently error-prone process? PLoS Genet 10:e1004086
16. Bianco PR, Tracy RB, Kowalczykowski SC (1998) DNA strand exchange proteins: a biochemical and physical comparison. Front Biosci 3:D570-603
17. Biran A, Zada L, Abou Karam P, Vadai E, Roitman L, Ovadya Y, Porat Z, Krizhanovsky V (2017) Quantitative identification of senescent cells in aging and disease. Aging Cell 16:661-671
18. Birchmeier C, Birchmeier W, Gherardi E, Vande Woude GF (2003) Met, metastasis, motility and more. Nat Rev Mol Cell Biol 4:915-925
19. Bodnar AG, Ouellette M, Frolkis M, Holt SE, Chiu CP, Morin GB, Harley CB, Shay JW, Lichtsteiner S, Wright WE (1998) Extension of life-span by introduction of telomerase into normal human cells. Science 279:349-352
20. Bothmer A, Robbiani DF, Di Virgilio M, Bunting SF, Klein IA, Feldhahn N, Barlow J, Chen HT, Bosque D, Callen E, Nussenzweig A, Nussenzweig MC (2011) Regulation of DNA end joining, resection, and immunoglobulin class switch recombination by 53BP1. Mol Cell 42:319-329
21. Botuyan MV, Lee J, Ward IM, Kim JE, Thompson JR, Chen J, Mer G (2006) Structural basis for the methylation state-specific recognition of histone H4-K20 by 53BP1 and Crb2 in DNA repair. Cell 127:1361-1373

22. Braig M, Lee S, Loddenkemper C, Rudolph C, Peters AH, Schlegelberger B, Stein H, Dörken B, Jenuwein T, Schmitt CA (2005) Oncogene-induced senescence as an initial barrier in lymphoma development. Nature 436:660-665
23. Bussian TJ, Aziz A, Meyer CF, Swenson BL, van Deursen JM, Baker DJ (2018) Clearance of senescent glial cells prevents tau-dependent pathology and cognitive decline. Nature 562:578-582
24. Cahu J, Bustany S, Sola B (2012) Senescence-associated secretory phenotype favors the emergence of cancer stem-like cells. Cell Death Dis 3:e446
25. Campisi J, d'Adda di Fagagna F (2007) Cellular senescence: when bad things happen to good cells. Nat Rev Mol Cell Biol 8:729-740
26. Campisi J, Andersen JK, Kapahi P, Melov S (2011) Cellular senescence: a link between cancer and age-related degenerative disease? Semin Cancer Biol 21:354-359
27. Cao K, Blair CD, Faddah DA, Kieckhaefer JE, Olive M, Erdos MR, Nabel EG, Collins FS (2011) Progerin and telomere dysfunction collaborate to trigger cellular senescence in normal human fibroblasts. J Clin Invest 121:2833-2844
28. Carbone R, Pearson M, Minucci S, Pelicci PG (2002) PML NBs associate with the hMre11 complex and p53 at sites of irradiation induced DNA damage. Oncogene 21:1633-1640
29. Celeste A, Petersen S, Romanienko PJ, Fernandez-Capetillo O, Chen HT, Sedelnikova OA, Reina-San-Martin B, Coppola V, Meffre E, Difilippantonio MJ, Redon C, Pilch DR, Olaru A, Eckhaus M, Camerini-Otero RD, Tessarollo L, Livak F, Manova K, Bonner WM, Nussenzweig MC, Nussenzweig A (2002) Genomic instability in mice lacking histone H2AX. Science 296:922-927
30. Chan DC (2006) Mitochondria: dynamic organelles in disease, aging, and development. Cell 125:1241-1252
31. Chandra T, Kirschner K, Thuret JY, Pope BD, Ryba T, Newman S, Ahmed K, Samarajiwa SA, Salama R, Carroll T, Stark R, Janky R, Narita M, Xue L, Chicas A, Nunez S, Janknecht R, Hayashi-Takanaka Y, Wilson MD, Marshall A, Odom DT, Babu MM, Bazett-Jones DP, Tavare S, Edwards PA, Lowe SW, Kimura H, Gilbert DM, Narita M (2012) Independence of repressive histone marks and chromatin compaction during senescent heterochromatic layer formation. Mol Cell 47:203-214
32. Chandra T, Narita M (2013) High-order chromatin structure and the epigenome in SAHFs. Nucleus 4:23-28
33. Chandra T, Ewels PA, Schoenfelder S, Furlan-Magaril M, Wingett SW, Kirschner K, Thuret JY, Andrews S, Fraser P, Reik W (2015) Global Reorganization of the Nuclear Landscape in Senescent Cells. Cell Reports 10:471-483
34. Chang J, Wang Y, Shao L, Laberge RM, Demaria M, Campisi J, Janakiraman K, Sharpless NE, Ding S, Feng W, Luo Y, Wang X, Aykin-Burns N, Krager K, Ponnappan U, Hauer-Jensen M, Meng A, Zhou D (2016) Clearance of senescent cells by ABT263 rejuvenates aged hematopoietic stem cells in mice. Nat Med 22:78-83
35. Chen J, Morrical MD, Donigan KA, Weidhaas JB, Sweasy JB, Averill AM, Tomczak JA, Morrical SW (2015) Tumor-associated mutations in a conserved structural motif alter physical and biochemical properties of human RAD51 recombinase. Nucleic Acids Res 43:1098-1111
36. Chen Q, Fischer A, Reagan JD, Yan LJ, Ames BN (1995) Oxidative DNA damage and senescence of human diploid fibroblast cells. Proc Natl Acad Sci U S A 92:4337-4341
37. Chen SH, Chan NL, Hsieh TS (2013) New mechanistic and functional insights into DNA topoisomerases. Annu Rev Biochem 82:139-170
38. Chen Z, Trotman LC, Shaffer D, Lin HK, Dotan ZA, Niki M, Koutcher JA, Scher HI, Ludwig T, Gerald W, Cordon-Cardo C, Pandolfi PP (2005) Crucial role of p53-dependent cellular senescence in suppression of Pten-deficient tumorigenesis. Nature 436:725-730
39. Chien Y, Scuoppo C, Wang X, Fang X, Balgley B, Bolden JE, Premsrirut P, Luo W, Chicas A, Lee CS, Kogan SC, Lowe SW (2011) Control of the senescence-associated secretory phenotype by NF-κB promotes senescence and enhances chemosensitivity. Genes Dev 25:2125-2136

40. Childs BG, Baker DJ, Kirkland JL, Campisi J, van Deursen JM (2014) Senescence and apoptosis: dueling or complementary cell fates? EMBO Rep 15:1139-1153
41. Childs BG, Baker DJ, Wijshake T, Conover CA, Campisi J, van Deursen JM (2016) Senescent intimal foam cells are deleterious at all stages of atherosclerosis. Science 354:472-477
42. Chinta SJ, Woods G, Rane A, Demaria M, Campisi J, Andersen JK (2015) Cellular senescence and the aging brain. Exp Gerontol 68:3-7
43. Chinta SJ, Woods G, Demaria M, Rane A, Zou Y, McQuade A, Rajagopalan S, Limbad C, Madden DT, Campisi J, Andersen JK (2018) Cellular Senescence Is Induced by the Environmental Neurotoxin Paraquat and Contributes to Neuropathology Linked to Parkinson's Disease. Cell Rep 22:930-940
44. Cichorek M, Wachulska M, Stasiewicz A, Tyminska A (2013) Skin melanocytes: biology and development. Postepy Dermatol Alergol 30:30-41
45. Clements CS, Bikkul MU, Ofosu W, Eskiw C, Tree D, Makarov E, Kill IR, Bridger JM (2019) Presence and distribution of progerin in HGPS cells is ameliorated by drugs that impact on the mevalonate and mTOR pathways. Biogerontology 20:337-358
46. Collado M, Gil J, Efeyan A, Guerra C, Schuhmacher AJ, Barradas M, Benguria A, Zaballos A, Flores JM, Barbacid M, Beach D, Serrano M (2005) Tumour biology: senescence in premalignant tumours. Nature 436:642
47. Contrepois K, Coudereau C, Benayoun BA, Schuler N, Roux PF, Bischof O, Courbeyrette R, Carvalho C, Thuret JY, Ma Z, Derbois C, Nevers MC, Volland H, Redon CE, Bonner WM, Deleuze JF, Wiel C, Bernard D, Snyder MP, Rube CE, Olaso R, Fenaille F, Mann C (2017) Histone variant H2A.J accumulates in senescent cells and promotes inflammatory gene expression. Nat Commun 8:14995
48. Coppe JP, Patil CK, Rodier F, Sun Y, Munoz DP, Goldstein J, Nelson PS, Desprez PY, Campisi J (2008) Senescence-associated secretory phenotypes reveal cell-nonautonomous functions of oncogenic RAS and the p53 tumor suppressor. PLoS Biol 6:2853-2868
49. Coppé JP, Patil CK, Rodier F, Sun Y, Muñoz DP, Goldstein J, Nelson PS, Desprez PY, Campisi J (2008) Senescence-associated secretory phenotypes reveal cell-nonautonomous functions of oncogenic RAS and the p53 tumor suppressor. PLoS Biol 6:2853-2868
50. Corpet A, Olbrich T, Gwerder M, Fink D, Stucki M (2014) Dynamics of histone H3.3 deposition in proliferating and senescent cells reveals a DAXX-dependent targeting to PML-NBs important for pericentromeric heterochromatin organization. Cell Cycle 13:249-267
51. Courtois-Cox S, Genther Williams SM, Reczek EE, Johnson BW, McGillicuddy LT, Johannessen CM, Hollstein PE, MacCollin M, Cichowski K (2006) A negative feedback signaling network underlies oncogene-induced senescence. Cancer Cell 10:459-472
52. Courtois-Cox S, Jones SL, Cichowski K (2008) Many roads lead to oncogene-induced senescence. Oncogene 27:2801-2809
53. Crescenzi E, Pacifico F, Lavorgna A, De Palma R, D'Aiuto E, Palumbo G, Formisano S, Leonardi A (2011) NF-κB-dependent cytokine secretion controls Fas expression on chemotherapy-induced premature senescent tumor cells. Oncogene 30:2707-2717
54. d'Adda di Fagagna F, Reaper PM, Clay-Farrace L, Fiegler H, Carr P, Von Zglinicki T, Saretzki G, Carter NP, Jackson SP (2003) A DNA damage checkpoint response in telomere-initiated senescence. Nature 426:194-198
55. d'Adda di Fagagna F (2008) Living on a break: cellular senescence as a DNA-damage response. Nat Rev Cancer 8:512-522
56. Dahl KN, Engler AJ, Pajerowski JD, Discher DE (2005) Power-law rheology of isolated nuclei with deformation mapping of nuclear substructures. Biophys J 89:2855-2864
57. Dankort D, Filenova E, Collado M, Serrano M, Jones K, McMahon M (2007) A new mouse model to explore the initiation, progression, and therapy of BRAFV600E-induced lung tumors. Genes Dev 21:379-384
58. De Sandre-Giovannoli A, Bernard R, Cau P, Navarro C, Amiel J, Boccaccio I, Lyonnet S, Stewart CL, Munnich A, Le Merrer M, Lévy N (2003) Lamin a truncation in Hutchinson-Gilford progeria. Science 300:2055

59. DeFazio LG, Stansel RM, Griffith JD, Chu G (2002) Synapsis of DNA ends by DNA-dependent protein kinase. Embo Journal 21:3192-3200
60. Demaria M, Ohtani N, Youssef SA, Rodier F, Toussaint W, Mitchell JR, Laberge RM, Vijg J, Van Steeg H, Dolle ME, Hoeijmakers JH, de Bruin A, Hara E, Campisi J (2014) An essential role for senescent cells in optimal wound healing through secretion of PDGF-AA. Dev Cell 31:722-733
61. Demaria M, O'Leary MN, Chang J, Shao L, Liu S, Alimirah F, Koenig K, Le C, Mitin N, Deal AM, Alston S, Academia EC, Kilmarx S, Valdovinos A, Wang B, de Bruin A, Kennedy BK, Melov S, Zhou D, Sharpless NE, Muss H, Campisi J (2017) Cellular Senescence Promotes Adverse Effects of Chemotherapy and Cancer Relapse. Cancer Discov 7:165-176
62. Dimri GP, Lee X, Basile G, Acosta M, Scott G, Roskelley C, Medrano EE, Linskens M, Rubelj I, Pereira-Smith O (1995) A biomarker that identifies senescent human cells in culture and in aging skin in vivo. Proc Natl Acad Sci U S A 92:9363-9367
63. Dinant C, Houtsmuller AB, Vermeulen W (2008) Chromatin structure and DNA damage repair. Epigenetics Chromatin 1:9
64. Dreesen O, Chojnowski A, Ong PF, Zhao TY, Common JE, Lunny D, Lane EB, Lee SJ, Vardy LA, Stewart CL, Colman A (2013a) Lamin B1 fluctuations have differential effects on cellular proliferation and senescence. Journal of Cell Biology 200:605-617
65. Dreesen O, Ong PF, Chojnowski A, Colman A (2013b) The contrasting roles of lamin B1 in cellular aging and human disease. Nucleus 4:283-290
66. Du LL, Nakamura TM, Russell P (2006) Histone modification-dependent and -independent pathways for recruitment of checkpoint protein Crb2 to double-strand breaks. Genes Dev 20:1583-1596
67. Erenpreisa J (1981) Staining of DNA with uranylacetate in hydrolysed ultrathin sections. Acta Histochem 68:22-26
68. Eriksson M, Brown WT, Gordon LB, Glynn MW, Singer J, Scott L, Erdos MR, Robbins CM, Moses TY, Berglund P, Dutra A, Pak E, Durkin S, Csoka AB, Boehnke M, Glover TW, Collins FS (2003) Recurrent de novo point mutations in lamin A cause Hutchinson-Gilford progeria syndrome. Nature 423:293-298
69. Falck J, Coates J, Jackson SP (2005) Conserved modes of recruitment of ATM, ATR and DNA-PKcs to sites of DNA damage. Nature 434:605-611
70. Farage MA, Miller KW, Elsner P, Maibach HI (2008) Functional and physiological characteristics of the aging skin. Aging Clin Exp Res 20:195-200
71. Farage MA, Miller KW, Elsner P, Maibach HI (2013) Characteristics of the Aging Skin. Adv Wound Care (New Rochelle) 2:5-10
72. Farr JN, Xu M, Weivoda MM, Monroe DG, Fraser DG, Onken JL, Negley BA, Sfeir JG, Ogrodnik MB, Hachfeld CM, LeBrasseur NK, Drake MT, Pignolo RJ, Pirtskhalava T, Tchkonia T, Oursler MJ, Kirkland JL, Khosla S (2017) Targeting cellular senescence prevents age-related bone loss in mice. Nat Med 23:1072-1079
73. Ferbeyre G, de Stanchina E, Querido E, Baptiste N, Prives C, Lowe SW (2000) PML is induced by oncogenic ras and promotes premature senescence. Genes Dev 14:2015-2027
74. Fernandez-Capetillo O, Chen HT, Celeste A, Ward I, Romanienko PJ, Morales JC, Naka K, Xia Z, Camerini-Otero RD, Motoyama N, Carpenter PB, Bonner WM, Chen J, Nussenzweig A (2002) DNA damage-induced G2-M checkpoint activation by histone H2AX and 53BP1. Nat Cell Biol 4:993-997
75. Ferrari M, Dibitetto D, De Gregorio G, Eapen VV, Rawal CC, Lazzaro F, Tsabar M, Marini F, Haber JE, Pellicioli A (2015) Functional interplay between the 53BP1-ortholog Rad9 and the Mre11 complex regulates resection, end-tethering and repair of a double-strand break. PLoS Genet 11:e1004928
76. Fradet-Turcotte A, Canny MD, Escribano-Diaz C, Orthwein A, Leung CC, Huang H, Landry MC, Kitevski-LeBlanc J, Noordermeer SM, Sicheri F, Durocher D (2013) 53BP1 is a reader of the DNA-damage-induced H2A Lys 15 ubiquitin mark. Nature 499:50-54

77. Franceschi C, Campisi J (2014) Chronic inflammation (inflammaging) and its potential contribution to age-associated diseases. J Gerontol A Biol Sci Med Sci 69 Suppl 1:S4-9
78. Freund A, Orjalo AV, Desprez PY, Campisi J (2010) Inflammatory networks during cellular senescence: causes and consequences. Trends Mol Med 16:238-246
79. Freund A, Patil CK, Campisi J (2011) p38MAPK is a novel DNA damage response-independent regulator of the senescence-associated secretory phenotype. EMBO J 30:1536-1548
80. Freund A, Laberge RM, Demaria M, Campisi J (2012a) Lamin B1 loss is a senescence-associated biomarker. Mol Biol Cell 23:2066-2075
81. Freund A, Laberge RM, Demaria M, Campisi J (2012b) Lamin B1 loss is a senescence-associated biomarker. Molecular Biology of the Cell 23:2066-2075
82. Fumagalli M, Rossiello F, Clerici M, Barozzi S, Cittaro D, Kaplunov JM, Bucci G, Dobreva M, Matti V, Beausejour CM, Herbig U, Longhese MP, d'Adda di Fagagna F (2012) Telomeric DNA damage is irreparable and causes persistent DNA-damage-response activation. Nat Cell Biol 14:355-365
83. Fumagalli M, Rossiello F, Mondello C, d'Adda di Fagagna F (2014) Stable cellular senescence is associated with persistent DDR activation. PLoS One 9:e110969
84. Funayama R, Saito M, Tanobe H, Ishikawa F (2006) Loss of linker histone H1 in cellular senescence. J Cell Biol 175:869-880
85. Ghosh K, Capell BC (2016) The Senescence-Associated Secretory Phenotype: Critical Effector in Skin Cancer and Aging. J Invest Dermatol 136:2133-2139
86. Goldberg M, Stucki M, Falck J, D'Amours D, Rahman D, Pappin D, Bartek J, Jackson SP (2003) MDC1 is required for the intra-S-phase DNA damage checkpoint. Nature 421:952-956
87. Goodarzi AA, Noon AT, Deckbar D, Ziv Y, Shiloh Y, Löbrich M, Jeggo PA (2008) ATM signaling facilitates repair of DNA double-strand breaks associated with heterochromatin. Mol Cell 31:167-177
88. Gottlieb TM, Jackson SP (1993) The DNA-dependent protein kinase: requirement for DNA ends and association with Ku antigen. Cell 72:131-142
89. Gruenbaum Y, Margalit A, Goldman RD, Shumaker DK, Wilson KL (2005) The nuclear lamina comes of age. Nat Rev Mol Cell Biol 6:21-31
90. Gruenbaum Y, Foisner R (2015) Lamins: nuclear intermediate filament proteins with fundamental functions in nuclear mechanics and genome regulation. Annu Rev Biochem 84:131-164
91. Gu J, Lu H, Tippin B, Shimazaki N, Goodman MF, Lieber MR (2007a) XRCC4 : DNA ligase IV can ligate incompatible DNA ends and can ligate across gaps (vol 26, pg 1010, 2007). Embo Journal 26:3506-3507
92. Gu JF, Lu HH, Tsai AG, Schwarz K, Lieber MR (2007b) Single-stranded DNA ligation and XLF-stimulated incompatible DNA end ligation by the XRCC4-DNA ligase IV complex: influence of terminal DNA sequence. Nucleic Acids Research 35:5755-5762
93. Guelen L, Pagie L, Brasset E, Meuleman W, Faza MB, Talhout W, Eussen BH, de Klein A, Wessels L, de Laat W, van Steensel B (2013) Domain organization of human chromosomes revealed by mapping of nuclear lamina interactions (vol 453, pg 948, 2008). Nature 500:242-242
94. Haber JE, Ira G, Malkova A, Sugawara N (2004) Repairing a double-strand chromosome break by homologous recombination: revisiting Robin Holliday's model. Philos Trans R Soc Lond B Biol Sci 359:79-86
95. Hake SB, Allis CD (2006) Histone H3 variants and their potential role in indexing mammalian genomes: the "H3 barcode hypothesis". Proc Natl Acad Sci U S A 103:6428-6435
96. Haruta N, Kurokawa Y, Murayama Y, Akamatsu Y, Unzai S, Tsutsui Y, Iwasaki H (2006) The Swi5-Sfr1 complex stimulates Rhp51/Rad51- and Dmc1-mediated DNA strand exchange in vitro. Nat Struct Mol Biol 13:823-830
97. Hauer MH, Gasser SM (2017) Chromatin and nucleosome dynamics in DNA damage and repair. Genes Dev 31:2204-2221

98. Hayflick L, Moorhead PS (1961) The serial cultivation of human diploid cell strains. Exp Cell Res 25:585-621
99. He Y, Thummuri D, Zheng G, Okunieff P, Citrin DE, Vujaskovic Z, Zhou D (2019) Cellular senescence and radiation-induced pulmonary fibrosis. Transl Res 209:14-21
100. Henikoff S, Smith MM (2015) Histone variants and epigenetics. Cold Spring Harb Perspect Biol 7:a019364
101. Herbig U, Jobling WA, Chen BPC, Chen DJ, Sedivy JM (2004) Telomere shortening triggers senescence of human cells through a pathway involving ATM, p53, and p21(CIP1), but not p16(INK4a). Molecular Cell 14:501-513
102. Holliday R (2007) A mechanism for gene conversion in fungi. Genet Res 89:285-307
103. Hustedt N, Durocher D (2016) The control of DNA repair by the cell cycle. Nat Cell Biol 19:1-9
104. Huyen Y, Zgheib O, Ditullio RA, Gorgoulis VG, Zacharatos P, Petty TJ, Sheston EA, Mellert HS, Stavridi ES, Halazonetis TD (2004) Methylated lysine 79 of histone H3 targets 53BP1 to DNA double-strand breaks. Nature 432:406-411
105. Iliakis G (1997) Cell cycle regulation in irradiated and nonirradiated cells. Semin Oncol 24:602-615
106. Iliakis G, Wang Y, Guan J, Wang H (2003) DNA damage checkpoint control in cells exposed to ionizing radiation. Oncogene 22:5834-5847
107. Imanishi T, Hano T, Nishio I (2005) Estrogen reduces endothelial progenitor cell senescence through augmentation of telomerase activity. J Hypertens 23:1699-1706
108. Jackson SP (2002) Sensing and repairing DNA double-strand breaks. Carcinogenesis 23:687-696
109. Jackson SP, Bartek J (2009) The DNA-damage response in human biology and disease. Nature 461:1071-1078
110. Jeon OH, Kim C, Laberge RM, Demaria M, Rathod S, Vasserot AP, Chung JW, Kim DH, Poon Y, David N, Baker DJ, van Deursen JM, Campisi J, Elisseeff JH (2017) Local clearance of senescent cells attenuates the development of post-traumatic osteoarthritis and creates a pro-regenerative environment. Nat Med 23:775-781
111. Kammeyer A, Luiten RM (2015) Oxidation events and skin aging. Ageing Res Rev 21:16-29
112. Kaur E, Rajendra J, Jadhav S, Shridhar E, Goda JS, Moiyadi A, Dutt S (2015) Radiation-induced homotypic cell fusions of innately resistant glioblastoma cells mediate their sustained survival and recurrence. Carcinogenesis 36:685-695
113. Kim J, Daniel J, Espejo A, Lake A, Krishna M, Xia L, Zhang Y, Bedford MT (2006) Tudor, MBT and chromo domains gauge the degree of lysine methylation. EMBO Rep 7:397-403
114. Kim KS, Kim JE, Choi KJ, Bae S, Kim DH (2014) Characterization of DNA damage-induced cellular senescence by ionizing radiation in endothelial cells. Int J Radiat Biol 90:71-80
115. Kobayashi Y, Sakemura R, Kumagai A, Sumikawa E, Fujii M, Ayusawa D (2008) Nuclear swelling occurs during premature senescence mediated by MAP kinases in normal human fibroblasts. Biosci Biotechnol Biochem 72:1122-1125
116. Kornberg RD (1974) Chromatin structure: a repeating unit of histones and DNA. Science 184:868-871
117. Kouzarides T (2007) Chromatin modifications and their function. Cell 128:693-705
118. Kristiani L, Kim M, Kim Y (2020) Role of the Nuclear Lamina in Age-Associated Nuclear Reorganization and Inflammation. Cells 9
119. Krizhanovsky V, Yon M, Dickins RA, Hearn S, Simon J, Miething C, Yee H, Zender L, Lowe SW (2008) Senescence of activated stellate cells limits liver fibrosis. Cell 134:657-667
120. Krtolica A, Parrinello S, Lockett S, Desprez PY, Campisi J (2001) Senescent fibroblasts promote epithelial cell growth and tumorigenesis: a link between cancer and aging. Proc Natl Acad Sci U S A 98:12072-12077
121. Kuilman T, Michaloglou C, Vredeveld LC, Douma S, van Doorn R, Desmet CJ, Aarden LA, Mooi WJ, Peeper DS (2008) Oncogene-induced senescence relayed by an interleukin-dependent inflammatory network. Cell 133:1019-1031

122. Kumagai A, Dunphy WG (2000) Claspin, a novel protein required for the activation of Chk1 during a DNA replication checkpoint response in Xenopus egg extracts. Mol Cell 6:839-849
123. Labrie F, Belanger A, Cusan L, Gomez JL, Candas B (1997) Marked decline in serum concentrations of adrenal C19 sex steroid precursors and conjugated androgen metabolites during aging. J Clin Endocrinol Metab 82:2396-2402
124. Landau M (2007) Exogenous factors in skin aging. Curr Probl Dermatol 35:1-13
125. Lanz MC, Dibitetto D, Smolka MB (2019) DNA damage kinase signaling: checkpoint and repair at 30 years. EMBO J 38:e101801
126. Lavker RM, Sun TT, Oshima H, Barrandon Y, Akiyama M, Ferraris C, Chevalier G, Favier B, Jahoda CAB, Dhouailly D, Panteleyev AA, Christiano AM (2003) Hair follicle stem cells. Journal of Investigative Dermatology Symposium Proceedings 8:28-38
127. Lawless C, Wang C, Jurk D, Merz A, Zglinicki T, Passos JF (2010) Quantitative assessment of markers for cell senescence. Exp Gerontol 45:772-778
128. Lazzerini Denchi E, Attwooll C, Pasini D, Helin K (2005) Deregulated E2F activity induces hyperplasia and senescence-like features in the mouse pituitary gland. Mol Cell Biol 25:2660-2672
129. Lee AC, Fenster BE, Ito H, Takeda K, Bae NS, Hirai T, Yu ZX, Ferrans VJ, Howard BH, Finkel T (1999) Ras proteins induce senescence by altering the intracellular levels of reactive oxygen species. J Biol Chem 274:7936-7940
130. Lee S, Schmitt CA (2019) The dynamic nature of senescence in cancer. Nat Cell Biol 21:94-101
131. Lendvay TS, Morris DK, Sah J, Balasubramanian B, Lundblad V (1996) Senescence mutants of Saccharomyces cerevisiae with a defect in telomere replication identify three additional EST genes. Genetics 144:1399-1412
132. Lieber MR (2008) The mechanism of human nonhomologous DNA end joining. J Biol Chem 283:1-5
133. Ling S, Zhou L, Li H, Dai A, Liu JP, Komesaroff PA, Sudhir K (2006) Effects of 17beta-estradiol on growth and apoptosis in human vascular endothelial cells: influence of mechanical strain and tumor necrosis factor-alpha. Steroids 71:799-808
134. Liu D, Hornsby PJ (2007) Senescent human fibroblasts increase the early growth of xenograft tumors via matrix metalloproteinase secretion. Cancer Res 67:3117-3126
135. Liu T, Huang J (2014) Quality control of homologous recombination. Cell Mol Life Sci 71:3779-3797
136. Livak KJ, Schmittgen TD (2001) Analysis of relative gene expression data using real-time quantitative PCR and the 2(-Delta Delta C(T)) Method. Methods 25:402-408
137. Long M, Sun X, Shi W, Yanru A, Leung STC, Ding D, Cheema MS, MacPherson N, Nelson CJ, Ausio J, Yan Y, Ishibashi T (2019) A novel histone H4 variant H4G regulates rDNA transcription in breast cancer. Nucleic Acids Res 47:8399-8409
138. Lopez-Otin C, Blasco MA, Partridge L, Serrano M, Kroemer G (2013) The hallmarks of aging. Cell 153:1194-1217
139. Lopez MF, Tollervey J, Krastins B, Garces A, Sarracino D, Prakash A, Vogelsang M, Geesman G, Valderrama A, Jordan IK, Lunyak VV (2012) Depletion of nuclear histone H2A variants is associated with chronic DNA damage signaling upon drug-evoked senescence of human somatic cells. Aging (Albany NY) 4:823-842
140. Luger K, Mader AW, Richmond RK, Sargent DF, Richmond TJ (1997) Crystal structure of the nucleosome core particle at 2.8 A resolution. Nature 389:251-260
141. Luijsterburg MS, von Bornstaedt G, Gourdin AM, Politi AZ, Moné MJ, Warmerdam DO, Goedhart J, Vermeulen W, van Driel R, Höfer T (2010) Stochastic and reversible assembly of a multiprotein DNA repair complex ensures accurate target site recognition and efficient repair. J Cell Biol 189:445-463
142. Ma Y, Lu H, Tippin B, Goodman MF, Shimazaki N, Koiwai O, Hsieh CL, Schwarz K, Lieber MR (2004) A biochemically defined system for mammalian nonhomologous DNA end joining. Mol Cell 16:701-713

143. Ma YM, Schwarz K, Lieber MR (2005) The Artemis: DNA-PKcs endonuclease cleaves DNA loops, flaps, and gaps. DNA Repair 4:845-851
144. Macadangdang BR, Oberai A, Spektor T, Campos OA, Sheng F, Carey MF, Vogelauer M, Kurdistani SK (2014) Evolution of histone 2A for chromatin compaction in eukaryotes. Elife 3
145. Macip S, Igarashi M, Fang L, Chen A, Pan ZQ, Lee SW, Aaronson SA (2002) Inhibition of p21-mediated ROS accumulation can rescue p21-induced senescence. EMBO J 21:2180-2188
146. Marzluff WF, Duronio RJ (2002) Histone mRNA expression: multiple levels of cell cycle regulation and important developmental consequences. Curr Opin Cell Biol 14:692-699
147. Maser RS, Monsen KJ, Nelms BE, Petrini JH (1997) hMre11 and hRad50 nuclear foci are induced during the normal cellular response to DNA double-strand breaks. Mol Cell Biol 17:6087-6096
148. Matsuoka S, Ballif BA, Smogorzewska A, McDonald ER, 3rd, Hurov KE, Luo J, Bakalarski CE, Zhao Z, Solimini N, Lerenthal Y, Shiloh Y, Gygi SP, Elledge SJ (2007) ATM and ATR substrate analysis reveals extensive protein networks responsive to DNA damage. Science 316:1160-1166
149. Mattiroli F, Vissers JH, van Dijk WJ, Ikpa P, Citterio E, Vermeulen W, Marteijn JA, Sixma TK (2012) RNF168 ubiquitinates K13-15 on H2A/H2AX to drive DNA damage signaling. Cell 150:1182-1195
150. Michaloglou C, Vredeveld LC, Soengas MS, Denoyelle C, Kuilman T, van der Horst CM, Majoor DM, Shay JW, Mooi WJ, Peeper DS (2005) BRAFE600-associated senescence-like cell cycle arrest of human naevi. Nature 436:720-724
151. Mimitou EP, Symington LS (2009) DNA end resection: many nucleases make light work. DNA Repair (Amst) 8:983-995
152. Minamino T, Yoshida T, Tateno K, Miyauchi H, Zou Y, Toko H, Komuro I (2003) Ras induces vascular smooth muscle cell senescence and inflammation in human atherosclerosis. Circulation 108:2264-2269
153. Mitsui Y, Schneider EL (1976) Increased nuclear sizes in senescent human diploid fibroblast cultures. Exp Cell Res 100:147-152
154. Montecucco A, Rossi R, Ferrari G, Scovassi AI, Prosperi E, Biamonti G (2001) Etoposide induces the dispersal of DNA ligase I from replication factories. Mol Biol Cell 12:2109-2118
155. Montecucco A, Zanetta F, Biamonti G (2015) Molecular mechanisms of etoposide. EXCLI J 14:95-108
156. Munoz-Espin D, Canamero M, Maraver A, Gomez-Lopez G, Contreras J, Murillo-Cuesta S, Rodriguez-Baeza A, Varela-Nieto I, Ruberte J, Collado M, Serrano M (2013) Programmed cell senescence during mammalian embryonic development. Cell 155:1104-1118
157. Munoz-Espin D, Serrano M (2014) Cellular senescence: from physiology to pathology. Nat Rev Mol Cell Biol 15:482-496
158. Muñoz-Espín D, Cañamero M, Maraver A, Gómez-López G, Contreras J, Murillo-Cuesta S, Rodríguez-Baeza A, Varela-Nieto I, Ruberte J, Collado M, Serrano M (2013) Programmed cell senescence during mammalian embryonic development. Cell 155:1104-1118
159. Musi N, Valentine JM, Sickora KR, Baeuerle E, Thompson CS, Shen Q, Orr ME (2018) Tau protein aggregation is associated with cellular senescence in the brain. Aging Cell 17:e12840
160. Narita M, Nũnez S, Heard E, Lin AW, Hearn SA, Spector DL, Hannon GJ, Lowe SW (2003a) Rb-mediated heterochromatin formation and silencing of E2F target genes during cellular senescence. Cell 113:703-716
161. Narita M, Nunez S, Heard E, Narita M, Lin AW, Hearn SA, Spector DL, Hannon GJ, Lowe SW (2003b) Rb-mediated heterochromatin formation and silencing of E2F target genes during cellular senescence. Cell 113:703-716
162. Nelms BE, Maser RS, MacKay JF, Lagally MG, Petrini JH (1998) In situ visualization of DNA double-strand break repair in human fibroblasts. Science 280:590-592
163. New JH, Sugiyama T, Zaitseva E, Kowalczykowski SC (1998) Rad52 protein stimulates DNA strand exchange by Rad51 and replication protein A. Nature 391:407-410

164. Nishida H, Suzuki T, Tomaru Y, Hayashizaki Y (2005) A novel replication-independent histone H2a gene in mouse. BMC Genet 6:10
165. Noren Hooten N, Evans MK (2017) Techniques to Induce and Quantify Cellular Senescence. J Vis Exp
166. O'Driscoll M, Ruiz-Perez VL, Woods CG, Jeggo PA, Goodship JA (2003) A splicing mutation affecting expression of ataxia-telangiectasia and Rad3-related protein (ATR) results in Seckel syndrome. Nat Genet 33:497-501
167. Ohuchida K, Mizumoto K, Murakami M, Qian LW, Sato N, Nagai E, Matsumoto K, Nakamura T, Tanaka M (2004) Radiation to stromal fibroblasts increases invasiveness of pancreatic cancer cells through tumor-stromal interactions. Cancer Res 64:3215-3222
168. Ota T, Suzuki Y, Nishikawa T, Otsuki T, Sugiyama T, Irie R, Wakamatsu A, Hayashi K, Sato H, Nagai K, Kimura K, Makita H, Sekine M, Obayashi M, Nishi T, Shibahara T, Tanaka T, Ishii S, Yamamoto J, Saito K, Kawai Y, Isono Y, Nakamura Y, Nagahari K, Murakami K, Yasuda T, Iwayanagi T, Wagatsuma M, Shiratori A, Sudo H, Hosoiri T, Kaku Y, Kodaira H, Kondo H, Sugawara M, Takahashi M, Kanda K, Yokoi T, Furuya T, Kikkawa E, Omura Y, Abe K, Kamihara K, Katsuta N, Sato K, Tanikawa M, Yamazaki M, Ninomiya K, Ishibashi T, Yamashita H, Murakawa K, Fujimori K, Tanai H, Kimata M, Watanabe M, Hiraoka S, Chiba Y, Ishida S, Ono Y, Takiguchi S, Watanabe S, Yosida M, Hotuta T, Kusano J, Kanehori K, Takahashi-Fujii A, Hara H, Tanase TO, Nomura Y, Togiya S, Komai F, Hara R, Takeuchi K, Arita M, Imose N, Musashino K, Yuuki H, Oshima A, Sasaki N, Aotsuka S, Yoshikawa Y, Matsunawa H, Ichihara T, Shiohata N, Sano S, Moriya S, Momiyama H, Satoh N, Takami S, Terashima Y, Suzuki O, Nakagawa S, Senoh A, Mizoguchi H, Goto Y, Shimizu F, Wakebe H, Hishigaki H, Watanabe T, Sugiyama A, Takemoto M, Kawakami B, Yamazaki M, Watanabe K, Kumagai A, Itakura S, Fukuzumi Y, Fujimori Y, Komiyama M, Tashiro H, Tanigami A, Fujiwara T, Ono T, Yamada K, Fujii Y, Ozaki K, Hirao M, Ohmori Y, Kawabata A, Hikiji T, Kobatake N, Inagaki H, Ikema Y, Okamoto S, Okitani R, Kawakami T, Noguchi S, Itoh T, Shigeta K, Senba T, Matsumura K, Nakajima Y, Mizuno T, Morinaga M, Sasaki M, Togashi T, Oyama M, Hata H, Watanabe M, Komatsu T, Mizushima-Sugano J, Satoh T, Shirai Y, Takahashi Y, Nakagawa K, Okumura K, Nagase T, Nomura N, Kikuchi H, Masuho Y, Yamashita R, Nakai K, Yada T, Nakamura Y, Ohara O, Isogai T, Sugano S (2004) Complete sequencing and characterization of 21,243 full-length human cDNAs. Nat Genet 36:40-45
169. Ovadya Y, Landsberger T, Leins H, Vadai E, Gal H, Biran A, Yosef R, Sagiv A, Agrawal A, Shapira A, Windheim J, Tsoory M, Schirmbeck R, Amit I, Geiger H, Krizhanovsky V (2018) Impaired immune surveillance accelerates accumulation of senescent cells and aging. Nat Commun 9:5435
170. Parrinello S, Coppe JP, Krtolica A, Campisi J (2005) Stromal-epithelial interactions in aging and cancer: senescent fibroblasts alter epithelial cell differentiation. J Cell Sci 118:485-496
171. Pasparakis M, Haase I, Nestle FO (2014) Mechanisms regulating skin immunity and inflammation. Nat Rev Immunol 14:289-301
172. Paull TT, Rogakou EP, Yamazaki V, Kirchgessner CU, Gellert M, Bonner WM (2000) A critical role for histone H2AX in recruitment of repair factors to nuclear foci after DNA damage. Curr Biol 10:886-895
173. Peng A, Chen PL (2003) NFBD1, like 53BP1, is an early and redundant transducer mediating Chk2 phosphorylation in response to DNA damage. J Biol Chem 278:8873-8876
174. Pickersgill H, Kalverda B, de Wit E, Talhout W, Fornerod M, van Steensel B (2006) Characterization of the Drosophila melanogaster genome at the nuclear lamina. Nature Genetics 38:1005-1014
175. Podgorsak EB (2005) Radiation oncology physics: A handbook for teachers and students (Austria, International Atomic Energy Agency).
176. Pommier Y, Leo E, Zhang H, Marchand C (2010) DNA topoisomerases and their poisoning by anticancer and antibacterial drugs. Chem Biol 17:421-433
177. Postberg J, Forcob S, Chang WJ, Lipps HJ (2010) The evolutionary history of histone H3 suggests a deep eukaryotic root of chromatin modifying mechanisms. BMC Evol Biol 10:259

178. Prise KM, O'Sullivan JM (2009) Radiation-induced bystander signalling in cancer therapy. Nat Rev Cancer 9:351-360
179. Reynolds P, Anderson JA, Harper JV, Hill MA, Botchway SW, Parker AW, O'Neill P (2012) The dynamics of Ku70/80 and DNA-PKcs at DSBs induced by ionizing radiation is dependent on the complexity of damage. Nucleic Acids Research 40:10821-10831
180. Rodier F, Coppe JP, Patil CK, Hoeijmakers WA, Munoz DP, Raza SR, Freund A, Campeau E, Davalos AR, Campisi J (2009) Persistent DNA damage signalling triggers senescence-associated inflammatory cytokine secretion. Nat Cell Biol 11:973-979
181. Rodier F, Munoz DP, Teachenor R, Chu V, Le O, Bhaumik D, Coppe JP, Campeau E, Beausejour CM, Kim SH, Davalos AR, Campisi J (2011a) DNA-SCARS: distinct nuclear structures that sustain damage-induced senescence growth arrest and inflammatory cytokine secretion. J Cell Sci 124:68-81
182. Rodier F, Muñoz DP, Teachenor R, Chu V, Le O, Bhaumik D, Coppé JP, Campeau E, Beauséjour CM, Kim SH, Davalos AR, Campisi J (2011b) DNA-SCARS: distinct nuclear structures that sustain damage-induced senescence growth arrest and inflammatory cytokine secretion. J Cell Sci 124:68-81
183. Rodier F (2013) Detection of the senescence-associated secretory phenotype (SASP). Methods Mol Biol 965:165-173
184. Rodriguez R, Meuth M (2006) Chk1 and p21 cooperate to prevent apoptosis during DNA replication fork stress. Mol Biol Cell 17:402-412
185. Rogakou EP, Pilch DR, Orr AH, Ivanova VS, Bonner WM (1998) DNA double-stranded breaks induce histone H2AX phosphorylation on serine 139. J Biol Chem 273:5858-5868
186. Rogakou EP, Boon C, Redon C, Bonner WM (1999) Megabase chromatin domains involved in DNA double-strand breaks in vivo. J Cell Biol 146:905-916
187. Rossi R, Montecucco A, Donzelli M, Denegri M, Biamonti G, Scovassi A (2002) DNA ligase I is dephosphorylated during the execution step of etoposide-induced apoptosis. Cell Death Differ 9:89-90
188. Rossi R, Lidonnici MR, Soza S, Biamonti G, Montecucco A (2006) The dispersal of replication proteins after Etoposide treatment requires the cooperation of Nbs1 with the ataxia telangiectasia Rad3-related/Chk1 pathway. Cancer Res 66:1675-1683
189. Rovillain E, Mansfield L, Caetano C, Alvarez-Fernandez M, Caballero OL, Medema RH, Hummerich H, Jat PS (2011) Activation of nuclear factor-kappa B signalling promotes cellular senescence. Oncogene 30:2356-2366
190. S.M. Seltzer DTB, D.T. Burns, G. Dietze, H.-G. Menzel, H.G. Paretzke, A. Wambersie (2011). The international commission on radiation units and measurements
191. Sadaie M, Salama R, Carroll T, Tomimatsu K, Chandra T, Young ARJ, Narita M, Perez-Mancera PA, Bennett DC, Chong H, Kimura H, Narita M (2013) Redistribution of the Lamin B1 genomic binding profile affects rearrangement of heterochromatic domains and SAHF formation during senescence. Genes & Development 27:1800-1808
192. Sagiv A, Biran A, Yon M, Simon J, Lowe SW, Krizhanovsky V (2013) Granule exocytosis mediates immune surveillance of senescent cells. Oncogene 32:1971-1977
193. Salama R, Sadaie M, Hoare M, Narita M (2014) Cellular senescence and its effector programs. Genes Dev 28:99-114
194. Saleh T, Tyutyunyk-Massey L, Gewirtz DA (2019) Tumor Cell Escape from Therapy-Induced Senescence as a Model of Disease Recurrence after Dormancy. Cancer Res 79:1044-1046
195. Salminen A, Kauppinen A, Kaarniranta K (2012) Emerging role of NF-κB signaling in the induction of senescence-associated secretory phenotype (SASP). Cell Signal 24:835-845
196. San Filippo J, Chi P, Sehorn MG, Etchin J, Krejci L, Sung P (2006) Recombination mediator and Rad51 targeting activities of a human BRCA2 polypeptide. J Biol Chem 281:11649-11657
197. San Filippo J, Sung P, Klein H (2008) Mechanism of eukaryotic homologous recombination. Annu Rev Biochem 77:229-257
198. Sanders SL, Portoso M, Mata J, Bähler J, Allshire RC, Kouzarides T (2004) Methylation of histone H4 lysine 20 controls recruitment of Crb2 to sites of DNA damage. Cell 119:603-614

199. Sarkisian CJ, Keister BA, Stairs DB, Boxer RB, Moody SE, Chodosh LA (2007) Dose-dependent oncogene-induced senescence in vivo and its evasion during mammary tumorigenesis. Nat Cell Biol 9:493-505
200. Scaffidi P, Misteli T (2006) Lamin A-dependent nuclear defects in human aging. Science 312:1059-1063
201. Schirmer EC, Foisner R (2007) Proteins that associate with lamins: many faces, many functions. Experimental Cell Research 313:2167-2179
202. Schultz LB, Chehab NH, Malikzay A, Halazonetis TD (2000) p53 Binding protein 1 (53BP1) is an early participant in the cellular response to DNA double-strand breaks. Journal of Cell Biology 151:1381-1390
203. Sedelnikova OA, Horikawa I, Zimonjic DB, Popescu NC, Bonner WM, Barrett JC (2004) Senescing human cells and ageing mice accumulate DNA lesions with unrepairable double-strand breaks. Nat Cell Biol 6:168-170
204. Serrano M, Lin AW, McCurrach ME, Beach D, Lowe SW (1997) Oncogenic ras provokes premature cell senescence associated with accumulation of p53 and p16INK4a. Cell 88:593-602
205. Shah PP, Donahue G, Otte GL, Capell BC, Nelson DM, Cao KJ, Aggarwala V, Cruickshanks HA, Rai TS, McBryan T, Gregory BD, Adams PD, Berger SL (2013) Lamin B1 depletion in senescent cells triggers large-scale changes in gene expression and the chromatin landscape. Genes & Development 27:1787-1799
206. Shah Punatar R, Martin MJ, Wyatt HD, Chan YW, West SC (2017) Resolution of single and double Holliday junction recombination intermediates by GEN1. Proc Natl Acad Sci U S A 114:443-450
207. Shibata A, Jeggo P (2019) A historical reflection on our understanding of radiation-induced DNA double strand break repair in somatic mammalian cells; interfacing the past with the present. Int J Radiat Biol 95:945-956
208. Shiloh Y, Lehmann AR (2004) Maintaining integrity. Nat Cell Biol 6:923-928
209. Shimi T, Butin-Israeli V, Adam SA, Hamanaka RB, Goldman AE, Lucas CA, Shumaker DK, Kosak ST, Chandel NS, Goldman RD (2011) The role of nuclear lamin B1 in cell proliferation and senescence. Genes & Development 25:2579-2593
210. Shinohara A, Ogawa T (1998) Stimulation by Rad52 of yeast Rad51-mediated recombination. Nature 391:404-407
211. Shumaker DK, Dechat T, Kohlmaier A, Adam SA, Bozovsky MR, Erdos MR, Eriksson M, Goldman AE, Khuon S, Collins FS, Jenuwein T, Goldman RD (2006) Mutant nuclear lamin A leads to progressive alterations of epigenetic control in premature aging. Proc Natl Acad Sci U S A 103:8703-8708
212. Smith GCM, Jackson SP (1999) The DNA-dependent protein kinase. Genes & Development 13:916-934
213. Solinger JA, Heyer WD (2001) Rad54 protein stimulates the postsynaptic phase of Rad51 protein-mediated DNA strand exchange. Proc Natl Acad Sci U S A 98:8447-8453
214. Sonoda E, Hochegger H, Saberi A, Taniguchi Y, Takeda S (2006) Differential usage of non-homologous end-joining and homologous recombination in double strand break repair. DNA Repair (Amst) 5:1021-1029
215. Stein GH, Drullinger LF, Soulard A, Dulic V (1999) Differential roles for cyclin-dependent kinase inhibitors p21 and p16 in the mechanisms of senescence and differentiation in human fibroblasts. Mol Cell Biol 19:2109-2117
216. Stewart GS, Wang B, Bignell CR, Taylor AM, Elledge SJ (2003) MDC1 is a mediator of the mammalian DNA damage checkpoint. Nature 421:961-966
217. Strausberg RL, Feingold EA, Grouse LH, Derge JG, Klausner RD, Collins FS, Wagner L, Shenmen CM, Schuler GD, Altschul SF, Zeeberg B, Buetow KH, Schaefer CF, Bhat NK, Hopkins RF, Jordan H, Moore T, Max SI, Wang J, Hsieh F, Diatchenko L, Marusina K, Farmer AA, Rubin GM, Hong L, Stapleton M, Soares MB, Bonaldo MF, Casavant TL, Scheetz TE, Brownstein MJ, Usdin TB, Toshiyuki S, Carninci P, Prange C, Raha SS, Loquellano NA, Peters GJ, Abramson RD, Mullahy

SJ, Bosak SA, McEwan PJ, McKernan KJ, Malek JA, Gunaratne PH, Richards S, Worley KC, Hale S, Garcia AM, Gay LJ, Hulyk SW, Villalon DK, Muzny DM, Sodergren EJ, Lu X, Gibbs RA, Fahey J, Helton E, Ketteman M, Madan A, Rodrigues S, Sanchez A, Whiting M, Madan A, Young AC, Shevchenko Y, Bouffard GG, Blakesley RW, Touchman JW, Green ED, Dickson MC, Rodriguez AC, Grimwood J, Schmutz J, Myers RM, Butterfield YS, Krzywinski MI, Skalska U, Smailus DE, Schnerch A, Schein JE, Jones SJ, Marra MA, Mammalian Gene Collection Program T (2002) Generation and initial analysis of more than 15,000 full-length human and mouse cDNA sequences. Proc Natl Acad Sci U S A 99:16899-16903

218. Stucki M, Clapperton JA, Mohammad D, Yaffe MB, Smerdon SJ, Jackson SP (2005) MDC1 directly binds phosphorylated histone H2AX to regulate cellular responses to DNA double-strand breaks. Cell 123:1213-1226
219. Sung P (1997) Yeast Rad55 and Rad57 proteins form a heterodimer that functions with replication protein A to promote DNA strand exchange by Rad51 recombinase. Genes Dev 11:1111-1121
220. Symington LS (2002) Role of RAD52 epistasis group genes in homologous recombination and double-strand break repair. Microbiol Mol Biol Rev 66:630-670, table of contents
221. Symington LS, Rothstein R, Lisby M (2014) Mechanisms and regulation of mitotic recombination in Saccharomyces cerevisiae. Genetics 198:795-835
222. Tabasso AFS, Jones DJL, Jones GDD, Macip S (2019) Radiotherapy-Induced Senescence and its Effects on Responses to Treatment. Clinical Oncology 31:283-289
223. Tanaka H, Sato S, Koyama M, Kujirai T, Kurumizaka H (2020) Biochemical and structural analyses of the nucleosome containing human histone H2A.J. J Biochem 167:419-427
224. Tremethick DJ (2007) Higher-order structures of chromatin: the elusive 30 nm fiber. Cell 128:651-654
225. Underwood EA (1945) Wilhelm Conrad Rotgen (1845-1923) and the early development of radiology. Proc R Soc Med 38:697-706
226. van Gent DC, Hoeijmakers JH, Kanaar R (2001) Chromosomal stability and the DNA double-stranded break connection. Nat Rev Genet 2:196-206
227. Vernier M, Bourdeau V, Gaumont-Leclerc MF, Moiseeva O, Begin V, Saad F, Mes-Masson AM, Ferbeyre G (2011) Regulation of E2Fs and senescence by PML nuclear bodies. Genes Dev 25:41-50
228. Wajapeyee N, Serra RW, Zhu X, Mahalingam M, Green MR (2008) Oncogenic BRAF induces senescence and apoptosis through pathways mediated by the secreted protein IGFBP7. Cell 132:363-374
229. Waldera Lupa DM, Kalfalah F, Safferling K, Boukamp P, Poschmann G, Volpi E, Gotz-Rosch C, Bernerd F, Haag L, Huebenthal U, Fritsche E, Boege F, Grabe N, Tigges J, Stuhler K, Krutmann J (2015) Characterization of Skin Aging-Associated Secreted Proteins (SAASP) Produced by Dermal Fibroblasts Isolated from Intrinsically Aged Human Skin. J Invest Dermatol 135:1954-1968
230. Waldman T, Kinzler KW, Vogelstein B (1995) p21 is necessary for the p53-mediated G1 arrest in human cancer cells. Cancer Res 55:5187-5190
231. Walker JR, Corpina RA, Goldberg J (2001) Structure of the Ku heterodimer bound to DNA and its implications for double-strand break repair. Nature 412:607-614
232. Wang AS, Ong PF, Chojnowski A, Clavel C, Dreesen O (2017) Loss of lamin B1 is a biomarker to quantify cellular senescence in photoaged skin. Sci Rep 7:15678
233. Wang B, Matsuoka S, Carpenter PB, Elledge SJ (2002) 53BP1, a mediator of the DNA damage checkpoint. Science 298:1435-1438
234. Wang GG, Allis CD, Chi P (2007) Chromatin remodeling and cancer, Part I: Covalent histone modifications. Trends Mol Med 13:363-372
235. Wang H, Wang Z, Huang Y, Zhou Y, Sheng X, Jiang Q, Wang Y, Luo P, Luo M, Shi C (2019) Senolytics (DQ) Mitigates Radiation Ulcers by Removing Senescent Cells. Front Oncol 9:1576
236. Ward JF (1988) DNA damage produced by ionizing radiation in mammalian cells: identities, mechanisms of formation, and reparability. Prog Nucleic Acid Res Mol Biol 35:95-125

237. Weterings E, Verkaik NS, Bruggenwirth HT, Hoeijmakers JHJ, van Gent DC (2003) The role of DNA dependent protein kinase in synapsis of DNA ends. Nucleic Acids Research 31:7238-7246
238. Wickert RR, Visscher MO (2006) Structure and function of the epidermal barrier. American Journal of Infection Control 34:S98-S110
239. Woodcock CL, Safer JP, Stanchfield JE (1976) Structural repeating units in chromatin. I. Evidence for their general occurrence. Exp Cell Res 97:101-110
240. Wu L, Luo K, Lou Z, Chen J (2008) MDC1 regulates intra-S-phase checkpoint by targeting NBS1 to DNA double-strand breaks. Proc Natl Acad Sci U S A 105:11200-11205
241. Xiong Y, Hannon GJ, Zhang H, Casso D, Kobayashi R, Beach D (1993) p21 is a universal inhibitor of cyclin kinases. Nature 366:701-704
242. Yang F, Tuxhorn JA, Ressler SJ, McAlhany SJ, Dang TD, Rowley DR (2005a) Stromal expression of connective tissue growth factor promotes angiogenesis and prostate cancer tumorigenesis. Cancer Res 65:8887-8895
243. Yang G, Rosen DG, Zhang Z, Bast RC, Jr., Mills GB, Colacino JA, Mercado-Uribe I, Liu J (2006) The chemokine growth-regulated oncogene 1 (Gro-1) links RAS signaling to the senescence of stromal fibroblasts and ovarian tumorigenesis. Proc Natl Acad Sci U S A 103:16472-16477
244. Yang H, Li Q, Fan J, Holloman WK, Pavletich NP (2005b) The BRCA2 homologue Brh2 nucleates RAD51 filament formation at a dsDNA-ssDNA junction. Nature 433:653-657
245. Yannone SM, Khan IS, Zhou RZ, Zhou T, Valerie K, Povirk LF (2008) Coordinate 5 ' and 3 ' endonucleolytic trimming of terminally blocked blunt DNA double-strand break ends by Artemis nuclease and DNA-dependent protein kinase. Nucleic Acids Research 36:3354-3365
246. Yosef R, Pilpel N, Papismadov N, Gal H, Ovadya Y, Vadai E, Miller S, Porat Z, Ben-Dor S, Krizhanovsky V (2017) p21 maintains senescent cell viability under persistent DNA damage response by restraining JNK and caspase signaling. EMBO J 36:2280-2295
247. Zacarias-Fluck MF, Morancho B, Vicario R, Luque Garcia A, Escorihuela M, Villanueva J, Rubio IT, Arribas J (2015) Effect of cellular senescence on the growth of HER2-positive breast cancers. J Natl Cancer Inst 107
248. Zhang R, Poustovoitov MV, Ye X, Santos HA, Chen W, Daganzo SM, Erzberger JP, Serebriiskii IG, Canutescu AA, Dunbrack RL, Pehrson JR, Berger JM, Kaufman PD, Adams PD (2005) Formation of MacroH2A-containing senescence-associated heterochromatin foci and senescence driven by ASF1a and HIRA. Dev Cell 8:19-30
249. Zhang R, Chen W, Adams PD (2007) Molecular dissection of formation of senescence-associated heterochromatin foci. Mol Cell Biol 27:2343-2358
250. Zhou BB, Elledge SJ (2000) The DNA damage response: putting checkpoints in perspective. Nature 408:433-439
251. Zomer HD, Trentin AG (2018) Skin wound healing in humans and mice: Challenges in translational research. J Dermatol Sci 90:3-12
252. Zou J, Lei T, Guo P, Yu J, Xu Q, Luo Y, Ke R, Huang D (2019) Mechanisms shaping the role of ERK1/2 in cellular senescence (Review). Mol Med Rep 19:759-770

9 Supplemental

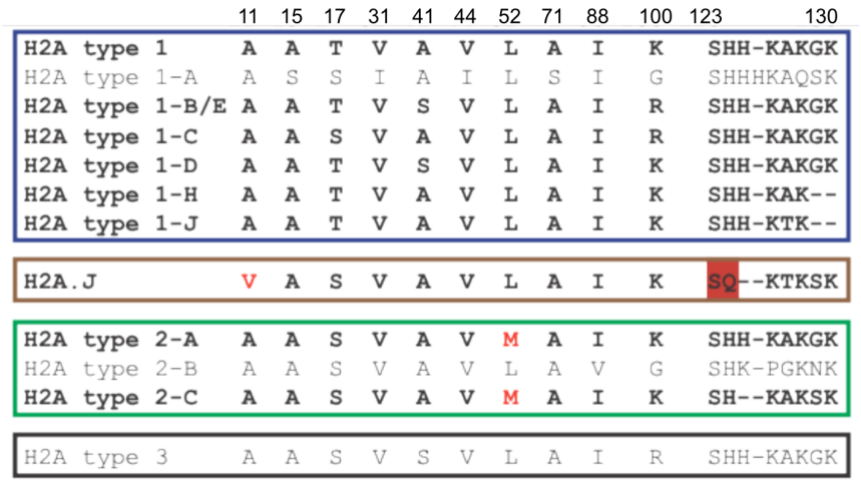

Supp. 1 Sequence alignment of human H2A.J with canonical H2As

(Contrepois et al., 2017)

10 List of tables

11 List of figures

12 Publications

1. DNA damage accumulation during fractionated low-dose radiation compromises hippocampal neurogenesis. Schmal Z, Isermann A, Hladik D, von Toerne C, Tapio S, Rübe C E, Radiother, 2019. 137:p.45-54

Publications submitted and currently under review:

2. Histone variant H2A.J involved in persistent DNA damage signaling triggers senescence-associated inflammatory cytokine secretion. Isermann A, Mann C, Rübe CE.

3. Human skin aging is associated with increased expression of the histone variant H2A.J in the epidermis. Rübe CE, Bäumert C, Schuler N, Isermann A, Schmal Z, Glanemann M, Mann C, Scherthan H.

13 Acknowledgements

First and foremost, I would like to thank Frau Prof. Dr. med. Claudia E. Rübe (or “Chefin” as you are know to most of us) for taking a chance on me and offering me the Ph.D. position in your lab. You provided a fascinating and challenging project for my dissertation that allowed me to grow and develop as a scientist. Simultaneously, I would like to thank you for giving me the time needed to do this and for supporting me throughout me PhD journey. I will always appreciate and value it.

I would also like to offer my thanks to Prof. Dr. rer. nat. Jens Mayer for all your time, support and guidance offered throughout. I would especially like to thank you for the feedback and constructive criticism you provided that pushed me to think and rethink my project along the way.

I also extend special thanks to Prof. Dr. med. Christian Rübe, director of the department for Radiation Therapy and Radiation Oncology, for all the support provided and the use of the clinics accelerator. Additionally, all the staff, from planners to technicians, in the clinic who helped and supported through each of the numerous cell irradiations over the years.

A special thank you is due to Carl Mann for who provided, not only the H2A.J antibody and the cell lines, but also provided his continued support and guidance throughout my entire project.

Not to be forgotten, all my colleagues in the lab. Nadine Schuler, thank you for your guidance and expertise. Daniela Jung, thank you for all your help with all things lab related and for jumping in when a helping hand was needed.

And of course, Yvonne Lorat. A huge thank you first of all for allowing me to use your fabulous TEM data to support my own findings in my dissertation! For all the discussion about H2A.J, all the advice, your enthusiasm for the project, all your time and patience with me, and, in general, for being a brilliant colleague in every way. Knowing you always had an open door and an open ear was priceless to me.

Then of course there is the world’s greatest TA: the lovely Kathrin Förderer. Even though you terrified me when I first started in the lab (no lie), I perserviered and soon we became great friends. Schwenker till the end! You are the best teacher and I would have been lost without you when I first started. Not only that, but you always cheered me up so much when I got frustrated and encouraged me to keep going. I am forever grateful.

Onto the next emotional support and, more importantly, friend. Caroline Bäumert. Oh, I remember your first day when you started and I had to share my office with you. You decorated your entire side with photos, flowers and colorful patterns. Not to mention your super happy morning persona! I remember thinking “this is going to be a challenge”. Well, I could not have been more wrong. All those chats, laughs (and cries) we shared while you were there are some of the highlights of my PhD. I’m so glad I got to share them all with you and I will always treasure our friendship.

Speaking of chats, laughs and cries, I would not have gotten this far without you, Zoe Schmal (aka Nick Miller). I have been grateful every day that I landed in the same lab as you did. I am so very lucky to have found you as a colleague and even better, as a friend. Your sarcasm and sense of humour made all the difference on those days when I was particularly down and frustrated, and made the days when I wasn’t even better. I hope in years to come, when we’re old and grey, we will be sitting sipping gin (or maybe a pint of Guinness) remembering, and laughing about, all those crazy times during our PhDs. JFK…

Now, onto those people, whom without, I would not be here. Julo, thank you for listening to my ramblings and complainings over the phone. For being the best wee brother and for always managing to cheer me up. Dad, you also deserve dues for all those rambling phone calls over the years! I could always depend on you to have an open ear. Mainly though, thank you for never doubting me, for making me laugh, showing me how important it is to not take myself so seriously, and to “always look on the bright side of life”. To Fronk (aka T.U.M.) I need to say: you may possibly be the most annoying person I know, BUT, you are also my rock, a constant through all the craziness since I was teeny tiny. I have a feeling that this PhD may be your greatest reverse Psychology trick to date…either way, it worked! Thank you for always being there.

And to my amazing Mum: Thank you for everything you have done and for always supporting me no matter what hair brained idea I might have. Words aren’t really enough. You always had confidence in me and my abilities. Having you as my Mum, and witnessing all the things you can do and have accomplished, made me believe in myself and gave me the confidence to go out and go after what I wanted. Cheesy, I know, but no word of a lie!

Last, but not least, my Peters. What a whirlwind it has been, and who would have thought a little “Goats Don’t Shave” concert in Bundoran would have been the start to such story. Thank you for being there, for listening when I need you to, but also for giving me kick up the a** when I needed it. Needless to say, I couldn’t have done it without you.

14 Curriculum vitae

The curriculum vitae was removed from the electronic version of the doctoral thesis for reasons of data protection.